

LEHRSTUHL FÜR BIOMEDIZINISCHE PHYSIK

TECHNISCHE UNIVERSITÄT MÜNCHEN

DEVELOPMENT OF A LARGE-ANIMAL X-RAY DARK-FIELD SCANNER

LUKAS BENEDICT GROMANN

DISSERTATION

TECHNISCHE UNIVERSITÄT MÜNCHEN
Physik Department
Lehrstuhl für Biomedizinische Physik

Development of a large-animal X-ray dark-field scanner

Lukas Benedict Gromann

Vollständiger Abdruck der von der Fakultät für Physik der Technischen Universität München zur Erlangung des akademischen Grades eines

Doktors der Naturwissenschaften (Dr. rer. nat.)

genehmigten Dissertation.

Vorsitzender: Prof. Dr. Martin Beneke
Prüfer der Dissertation: 1. Prof. Dr. Franz Pfeiffer
2. Prof. Dr. Jonathan Finley

Die Dissertation wurde am 13.09.2017 bei der Technischen Universität München eingereicht und durch die Fakultät für Physik am 01.12.2017 angenommen.

Abstract

X-ray chest radiography is an inexpensive and broadly available tool for the assessment of the human lung in daily clinical routine, but it typically lacks diagnostic sensitivity when it comes to the detection of pulmonary diseases in their early stages. Recent X-ray dark-field (XDF) imaging studies on dead and living mice have shown significant potential for improving imaging-based lung diagnostics, demonstrating that the XDF signal is highly sensitive to the pulmonary microstructure and its potential disorders. Especially in the case of early diagnosis of chronic obstructive pulmonary disease (COPD), XDF imaging clearly demonstrated the potential to outperform conventional radiography. However until now, a translation of this technique from the aforementioned small-animal models towards the investigation of larger mammals and finally humans has not been achieved.

The scope of this PhD thesis was therefore the development and optimization of a novel, high-energy large-animal XDF imaging system which overcomes the limitations of currently established setups; namely achieving a large field-of-view and allowing for high quality XDF images acquired at clinically compatible dose values and scan times. The main scientific results of this work have been published in Gromann, De Marco, et al., *In-vivo X-ray Dark-Field Chest Radiography of a Pig*, Nature Scientific Reports (2017). Here the very first in-vivo XDF chest radiographs of a pig with a field-of-view of $32 \times 35 \text{ cm}^2$ acquired in 40 sec scan time with an effective imaging dose of $80 \mu\text{Sv}$ were presented. The XDF radiographs yield a sufficiently high image contrast and quality to enable radiographic evaluation of the lungs. This result is a milestone in the bench-to-bedside translation of XDF imaging, with first human studies now at reach.

The content of this thesis covers the full development process of the system. Starting with the evaluation of the boundary conditions for the new system, the design specifications have been developed and the prototype was built. This step was followed by an extensive characterization and optimization of the system, before the first in-vivo images were acquired.

As a result of this work, XDF imaging is expected to become an invaluable tool in clinical practice both as a general chest X-ray modality and as a dedicated tool for high-risk patients affected by smoking, industrial work or smog. Additionally, the developed prototype was evaluated for advanced applications in security screening. Here detection of powder-like drugs hidden in luggage appears as a promising side application.

Kurzzusammenfassung

Radiographie des menschlichen Thorax ist eine kostengünstige und weitverbreitete Methode für die Erstuntersuchung der Lunge in der klinischen Routine. Leider ist die Sensitivität dieser Untersuchung insbesondere für Lungenerkrankungen im Frühstadium nicht sehr groß. Kürzlich veröffentlichte Studien an toten und lebenden Mäusen haben gezeigt, dass das neuartige Verfahren der Röntgen-Dunkelfeld-Bildgebung eine signifikante Verbesserung der bildbasierten Lungendiagnostik ermöglicht. Es wurde insbesondere gezeigt, dass Röntgen-Dunkelfeld-Bildgebung sehr sensitiv auf die Mikrostruktur der Lunge ist und dass damit insbesondere Lungenkrankheiten wie COPD im Frühstadium deutlich besser diagnostiziert werden können als mit konventioneller Thorax-Bildgebung.

Leider war es bis jetzt technisch noch nicht möglich, diese erfolgversprechende Technologie auch auf größere Tiere oder gar Menschen anzuwenden. Das Ziel dieser Promotionsarbeit bestand daher darin, einen neuartigen, Hochenergie-Röntgen-Dunkelfeld-Scanner zu entwickeln, welcher die Limitierungen bestehender Systeme überwindet und damit die Bildgebung von Großtieren ermöglicht. Hauptkriterien waren hier vor allem das große Sichtfeld und eine ausreichende Bildqualität bei klinisch vertretbarer Strahlendosis und Scanzeit. Die wichtigsten wissenschaftlichen Resultate dieser Arbeit sind in Gromann, De Marco, et al., *In-vivo X-ray Dark-Field Chest Radiography of a Pig*, Nature Scientific Reports (2017) publiziert. Hier wurden die weltweit ersten Thorax-Dunkelfeld-Bilder von einem lebenden Schwein präsentiert. Diese Bilder erreichten ein Sichtfeld von $32 \times 35 \text{ cm}^2$ und wurden in 40 Sekunden Scanzeit mit einer effektiven Strahlendosis von gerade einmal $80 \mu\text{Sv}$ aufgenommen. Dabei ist die Qualität der Dunkelfeld Bilder hoch genug um eine sinnvolle Radiologische Auswertung zu ermöglichen.

Dieses Ergebnis ist ein Meilenstein in der Entwicklung der Röntgen-Dunkelfeld-Bildgebung vom Labor hin zur klinischen Anwendung. Die ersten klinischen Humanversuche sind damit nun in Reichweite.

Die Promotionsarbeit umfasst das vollständige Spektrum der Entwicklung eines neuartigen Bildgebungssystems. Angefangen mit den Designspezifikationen wurde ein Prototyp des neuartigen Bildgebungssystem gebaut, welcher die gegebenen Rahmenbedingungen erfüllte. In einem zweiten Schritt wurde dieses System dann ausführlich charakterisiert und optimiert, bevor die Entwicklung mit den ersten in-vivo Experimenten an Schweinen erfolgreich abgeschlossen wurde.

Als Resultat dieser Arbeit ist die Technologie der Röntgen-Dunkelfeld-

Bildgebung nun so weit, um in ersten klinischen Versuchen eingesetzt zu werden. Auf Grund der Vorstudien an Mäusen ist zu erwarten, dass diese Methode eine enorme Bereicherung in der klinischen Praxis darstellen wird, sowohl als generelle Thorax Bildgebung, als auch als dedizierte Methode für Hochrisikopatienten, welche zum Beispiel durch Rauchen, industrielle Arbeit oder Smog besonders gefährdet für Lungenkrankheiten sind.

Schlussendlich wurde der neuentwickelte Prototyp noch für erweiterte Anwendungen im Bereich der Gepäckkontrolle evaluiert. Hier hat sich gezeigt, dass die Identifizierung von pulverförmigen Drogen in normalen Gepäckstücken ebenfalls eine vielversprechende Anwendung des neuen Systems darstellt.

Contents

1	Introduction	1
1.1	Motivation	1
1.2	Outline	3
1.3	Framework of the thesis	4
2	Theory & Background	5
2.1	X-rays and their interaction with matter	5
2.1.1	Interaction effects	6
2.1.2	Complex refractive index	6
2.1.3	Free space propagation	8
2.1.4	Talbot effect	10
2.2	Phase-contrast and dark-field imaging	10
2.2.1	Motivation	10
2.2.2	Grating based imaging	11
2.2.3	Phase- and XDF-sensitivity	18
2.2.4	Dark-field imaging of the lung	19
2.3	X-ray generation & Detection	20
2.3.1	X-ray tubes	20
2.3.2	Energy integrating detectors	21
2.3.3	Photon counting detector/ X-ray spectrometer	22
2.4	Dosimetry	24
2.4.1	Air kerma	25
2.4.2	Energy dose	25
2.4.3	Equivalent dose	25
2.4.4	Effective dose	26
2.5	Wave-optical simulations	28
2.5.1	Parallel vs. cone-beam geometry	28
2.5.2	X-ray source & X-ray detector	29
2.5.3	Wave-front propagation	29
2.6	Monte-Carlo simulations	34
2.6.1	Motivation	34

2.6.2	Physical model	34
2.6.3	Simulation framework	35
3	Design specifications of the scanner	37
3.1	Requirements for the new scanner	37
3.2	Grating optimization	39
3.2.1	G0	39
3.2.2	G1	42
3.2.3	G2	46
3.3	Increased FOV by a slot-scanning approach	47
3.3.1	Grating alignment & Stitching	47
3.3.2	Swing movement vs. planar movement (“parallax- problem”)	51
3.3.3	Motorization	54
3.4	Imaging system	56
3.4.1	Hardware	56
3.4.2	Control software	57
3.4.3	Lead shielding & Collimators	57
3.5	Image acquisition procedure	59
3.5.1	Conventional phase stepping mode	59
3.5.2	Slot-scanning	59
3.6	Summary: Design	60
4	Characterization of the prototype scanner	61
4.1	Large field-of-view	62
4.2	Visibility	62
4.2.1	Motivation	62
4.2.2	Methods	64
4.2.3	Results & Discussion: integrated visibility	64
4.2.4	Results & Discussion: energy-resolved visibility	65
4.3	Tube voltage optimization	67
4.3.1	Background & Motivation	67
4.3.2	Methods	67
4.3.3	Results	68
4.3.4	Discussion & Summary	69
4.4	Visibility reduction by Compton-scattering	71
4.4.1	Background & Motivation	71
4.4.2	Methods	72
4.4.3	Results	73
4.4.4	Summary & Outlook	76
4.5	Compton-scatter-correction for sample data	80

4.5.1	Motivation	80
4.5.2	Methods	80
4.5.3	Results & Discussion	81
4.5.4	Summary & Outlook	82
4.6	Beam/visibility-hardening effects	85
4.6.1	Background & Motivation	85
4.6.2	Calibration & Correction method	85
4.6.3	Choice of calibration material	86
4.6.4	Calibration measurements	87
4.6.5	Correction of bone artifacts	89
4.6.6	Discussion & Summary	93
4.7	Radiation dose	95
4.8	Resolution limits	97
4.8.1	Motivation	97
4.8.2	Methods	98
4.8.3	Results	98
4.8.4	Discussion & Summary	99
4.9	Scanning speed optimization	102
4.9.1	Motivation	102
4.9.2	Methods	102
4.9.3	Results	102
4.9.4	Discussion & Summary	103
4.10	Summary: Characterization of the prototype	105
5	Applications: Porcine chest imaging	107
5.1	First in-vivo porcine chest images	107
5.1.1	Motivation	107
5.1.2	Methods	108
5.1.3	Results & Discussion	109
5.2	Tube voltage optimization	113
5.2.1	Motivation	113
5.2.2	Methods	113
5.2.3	Results & Discussion	113
5.3	Motion artifacts	114
5.3.1	Motivation	114
5.3.2	Methods	115
5.3.3	Results & Discussion	115
5.4	Visibility-hardening and CS corrections	116
5.4.1	Motivation	116
5.4.2	Methods	117
5.4.3	Results & Discussion	117

5.5	Summary & Outlook	117
5.5.1	First in-vivo porcine XDF chest images	117
5.5.2	Tube voltage optimization	119
5.5.3	Motion artifacts	120
5.5.4	Visibility-hardening and CS correction	120
6	Advanced applications: drug screening in luggage	121
6.1	Motivation	121
6.2	Materials & Methods	122
6.2.1	Drug phantom samples	122
6.2.2	Image fusion algorithm	123
6.2.3	Tunable XDF sensitivity	123
6.3	Results	124
6.3.1	Real luggage sample	124
6.3.2	Adjusting the sensitivity with the X-ray energy	124
6.4	Discussion & Summary	127
7	Summary, Discussion & Outlook	129
7.1	Design of the large-animal XDF-scanner	129
7.2	Characterization of the scanner	130
7.3	Applications:	132
7.3.1	Porcine chest imaging	132
7.3.2	Drug screening	133
7.4	Discussion with other research in the field	134
7.5	Final conclusions	135
8	Appendix	137
	Publications and scientific presentations	137
	Bibliography	140
	Acknowledgements	159

Chapter 1

Introduction

In the first part of this chapter, the content of this PhD thesis is introduced. Further, the research focus of this thesis is motivated and placed in context of other research in the field. The second part of this chapter gives an outline of the structure of the thesis. A third part contains general remarks about the framework this PhD was placed in.

1.1 Motivation

Since it's discovery in 1895 by W. C. Röntgen[1], the ability of X-rays to penetrate dense matter has found a huge application in medical diagnostics, industry and research. In conventional X-ray imaging a sample is illuminated from one side and the attenuated transmission is measured at the opposite side. This shadow image shows differences in the density and composition of a sample very well e.g. dense bones are clearly distinguishable from soft-tissue or a metal gun hidden in a suitcase. But also other non-imaging applications like crystallography, where the 3D shape of molecules and proteins is decoded by X-ray defraction or X-ray fluorescence spectroscopy make broad use of X-rays[2].

However, conventional X-ray imaging can only measure the attenuation differences within a sample, but these differences can become very small for e.g. similar soft-tissue types. Differentiation of adipose tissue from muscle tissue by means of X-ray imaging is therefore rather challenging[3, 4]. To overcome this limitation, phase sensitive X-ray imaging methods were developed in the recent decades[3]. These approaches rely on the wave nature of X-rays and allow for a much higher soft-tissue contrast by measuring not only the attenuation caused by a sample but also the phase shift introduced to the X-rays. This is similar to refraction of visible light by a lens. However, the refraction

angles are so small for X-rays that sophisticated methods are required to measure them. These methods have first been developed for large-scale synchrotron facilities, where high brilliance X-rays are available. In general, there are free-space propagation-based approaches[5, 6], crystal analyzer-based methods[7, 8] and grating-based techniques[9, 10]. Only since a few years, a translation of phase sensitive imaging methods from these large-scale research facilities towards lab-based systems was achieved[11]. Here grating-based methods are most promising as they are compatible with conventional X-ray tubes and detectors. A further benefit of grating-based imaging techniques is the generation of a third imaging contrast besides the *phase* and the *attenuation* images: the X-ray *dark-field* (XDF) image[12]. This image can be considered as the amount of *ultra-small-angle* scattering introduced by a sample. This scattering signal allows for an assessment of the microstructure of the sample, without the need to directly resolve it. For example, a sample with 5 μm structure size can be probed with this technology with imaging pixels of a few hundred micrometers. This is also the technology used for this PhD thesis.

In general, grating based imaging allows also for a 3D reconstruction of the sample volume in all three imaging modalities (attenuation, phase and dark-field) if applied in a CT mode. Here, either the sample needs to be rotated or the gratings[13, 14]. However, this thesis is restricted to 2D imaging only. Radiographic imaging is usually performed with just a very limited number of viewing angles (e.g. for chest imaging most often two[4]). This type of imaging requires much less time and radiation dose compared to a full CT scan (which is basically a projection from every solid angle), and is therefore most often the initial assessment in clinical practice. In fact, radiographic chest imaging is one of the most common radiographic examinations[15]. The drawback of the 2D projection is the superposition of different features in the sample, which complicate diagnosis.

The potential benefits of grating based imaging for biomedical imaging applications were extensively studied in recent years in various ex-vivo samples[16–21] and most recently also in in-vivo mouse models[22–29]. Here especially lung imaging revealed a significant improvement compared to conventional, attenuation based imaging. The lung causes a significant XDF signal due to the large amount of air-tissue interfaces, that allow for the gas exchange. It was found, that all lung pathologies, which affect the microstructure of the lung, are much better visible in the XDF signal than in conventional, attenuation-based imaging. This renders XDF imaging a functional imaging tool for the lung. Even other imaging methods like nuclear magnetic resonance (NMR) imaging or ultrasound imaging, which are known for an increased soft-tissue contrast do not allow for such a functional assessment of

the lung. The analyzed pathologies are for example chronic obstructive pulmonary disease (COPD), lung fibrosis, lung tumors and as well as many more. As lung diseases are among the five major causes of death worldwide[30], any improvement in diagnosis such diseases will therefore benefit millions of people. However, all the promising results of XDF imaging were so far only demonstrated on mice. A translation of this technology towards larger mammals or even humans posed major technical and conceptual challenges. The scope of this thesis was therefore to overcome these limitations and enable the first in-vivo XDF chest images of pigs, which serve as an excellent model for the human thorax[31]. This feasibility study can neither be given by simulations nor by ex-vivo studies. Further, this prove-of-principle with living pigs can be considered as the last step in the long journey of the bench-to-bedside translation of XDF imaging. Started in large-scale research facilities decades ago, XDF imaging is now at the edge for clinical applications.

1.2 Outline

The structure of this PhD thesis is divided into four main parts. Starting with the theoretical background in **Chapter 2**, the reader is introduced to the basic concept of X-rays, their creation and detection, as well as their general interaction with matter. This includes also a detailed description of the grating-based imaging method as well as a discussion of the concept of dosimetry. Finally different simulation approaches are introduced which are necessary to model X-ray imaging systems numerically with a computer. These simulations are used in this thesis to optimize the imaging system to be developed. Although being mostly descriptive, this chapter also extends current literature and introduces some new features in the modeling of the gratings. These features are important for the understanding of the results in the following chapters.

In the next chapter (**Chapter 3**), the boundary conditions and resulting design specifications for the prototype are discussed in detail. The approach to achieve a high visibility at high energies as well as a large field-of-view is explained and the optimization results for all three gratings are presented. Finally, the implementation and actual realization of the hard- and software of the prototype is presented and the image acquisition process is elaborated. The design chapter is then followed by **Chapter 4**, which focuses on the characterization of the developed system. In this chapter the main performance indicators of the developed prototype are evaluated. Especially the achievable visibility is studied and the influence of Compton-scattering and visibility-hardening for the measured XDF signal is evaluated extensively.

For both of these effects a correction method is presented. Additionally, the optimal tube voltage for a technical phantom of a thorax is estimated and a measurement of the applied radiation dose is performed. Finally, the maximum imaging speed and achievable resolution limits are discussed.

The developed prototype is used in **Chapter 5** and **Chapter 6** for the very first imaging experiments. **Chapter 5** presents the results of the first in-vivo imaging experiments with pigs. Additionally, some optimizations regarding the image quality are given, with a focus on the heart-beat artifacts, as well as the applied tube voltage. As the scanner is not only able to measure large animals, its suitability for security-screening applications was additionally evaluated in **Chapter 6**.

Chapter 7 concludes this thesis with a brief summary of the main results and an outlook on further research perspectives and possible follow-up studies.

1.3 Framework of the thesis

Major parts of the work of this PhD thesis were carried out in close collaboration with the PhD projects of Konstantin Willer and Fabio De Marco. Especially the development of the imaging system was a team effort. For a full overview about the project the reader is therefore also referred to the PhD theses of Mr. Willer and Mr. De Marco. This thesis here focuses on the contributions to the project made by the author, however without the team this work would not have been possible to this extent.

Further, the development of this large-animal XDF-scanner involved a rather large research collaboration between the chair of Biomedical Physics of Prof. Pfeiffer from the Technical University Munich (TUM) and research partners from Koninklijke Philips N.V. (Hamburg), both the University Hospitals in Munich (Klinikum Rechts der Isar (TUM) & Klinikum der Ludwig-Maximilian Universität (LMU)), as well as the Institute of Molecular Animal Breeding and Biotechnology (LMU) which provided the expertise on the actual animal experiments. All animal experiments performed for this thesis were therefore approved by the corresponding authorities and every single animal was handled with great care and kept under pain-free anesthesia during the full experiments.

Chapter 2

Theory & Background

This chapter introduces the required theoretical backgrounds to understand the theoretical and experimental results which are presented in this thesis. At first, an introduction to the physics of X-rays and especially their interaction with matter is given. Thereafter, the basic principles of phase sensitive X-ray imaging methods are discussed, with a focus on grating based imaging methods. Next, the generation and detection of X-rays is discussed and the concept of dosimetry is introduced. Finally, different simulation approaches are introduced which allow to model X-ray imaging systems with a computer.

Contents

2.1	X-rays and their interaction with matter	5
2.2	Phase-contrast and dark-field imaging	10
2.3	X-ray generation & Detection	20
2.4	Dosimetry	24
2.5	Wave-optical simulations	28
2.6	Monte-Carlo simulations	34

2.1 X-rays and their interaction with matter

For over a hundred years now, X-rays are a substantial part of biomedical imaging applications. Their triumph is based on their ability to penetrate dense matter like a human body. This allowed, for the first time in history, for a noninvasive insight in the human body[1]. However, that this insight is only quasi noninvasive was found much later, when it was discovered that X-rays might interact with the cells of a living organism in a fatal way. These interactions of X-rays with matter are discussed in the following paragraphs in detail and their consequences to biomedical imaging applications are ex-

plained.

Although primarily considered to be particles, it is known since the work of Max von Laue in 1912[32] that X-rays also can be described as electromagnetic waves, the so called wave-particle dualism. In conventional X-ray images only the particle nature of X-rays is exploited to obtain basically a shadow image, highlighting dense structures like bones. Recently new methods were developed which take advantage of the wave nature of X-rays[3]. These methods are often summarized under the term *phase-contrast imaging*. In the wave model, X-rays can be described by a plane wave, propagating through vacuum[33]

$$\Psi(\mathbf{r}, t) = \Psi_0 \cdot e^{i(\mathbf{k} \cdot \mathbf{r} - \omega t)}, \quad (2.1)$$

with the amplitude of the wave Ψ_0 and the positions in space \mathbf{r} and time t . ω is the angular frequency and \mathbf{k} the wave vector with $|\mathbf{k}| = \frac{2\pi}{\lambda}$. Conventional X-ray detectors however are not sensitive to the phase of the wave and can only record the intensity

$$I(\mathbf{r}) = |\Psi(\mathbf{r})|^2 \quad (2.2)$$

of the wave field.

2.1.1 Interaction effects

If the X-ray wave is propagating through matter, different effects can occur with a probability mostly based on their energy and the atomic mass number of the interacting matter. For the energies considered in the thesis (1-200 keV), *photoelectric absorption*, *coherent Thomson-scattering* and *incoherent Compton-scattering* are the dominating effects for interactions of X-rays with matter. Other effects like *pair production* which occur at much higher energies (above 1.02 MeV) and *photon disintegration* are not discussed here. The interested reader is here referred to one of the various textbooks [33–36].

2.1.2 Complex refractive index

To describe the interaction of X-ray with matter phenomenologically, the formalism of the complex refractive index[34]

$$n = 1 - \delta + i\beta \quad (2.3)$$

was developed. The refractive index decrement δ describes the phase shift and β is the attenuation strength. Far from any absorption edges they can be written as[34]:

$$\delta = \frac{r_0 \lambda^2}{2\pi} n_a \cdot f_1^0 \quad (2.4)$$

$$\beta = \frac{r_0 \lambda^2}{2\pi} n_a \cdot f_2^0 \quad (2.5)$$

with the wavelength λ , the number density n_a (atoms or electron per unit volume), the Bohr radius r_0 and the complex atomic scattering coefficients f_1^0 and f_2^0 . The two atomic scattering coefficients describe the scattering amplitude of an incident X-ray wave by an isolated atom. These two parameter are measured and tabulated for a vast number of elements and energies by NIST[37].

With the concept of the refractive index the interaction of an X-ray wave with matter can be formulated for a plane electromagnetic wave as

$$\Psi(\mathbf{r}) = \Psi_0 \cdot e^{i\mathbf{k}\cdot\mathbf{r}} = \underbrace{\Psi_0 \cdot e^{i\mathbf{k}\cdot\mathbf{r}}}_{\text{vacuum propagation}} \cdot \underbrace{e^{-i\delta\mathbf{k}\cdot\mathbf{r}}}_{\text{phase-shift}} \cdot \underbrace{e^{-\beta\mathbf{k}\cdot\mathbf{r}}}_{\text{decay}}. \quad (2.6)$$

Behind a propagation distance L through a material there will be a change in the intensity due to the decay term. The transmitted intensity can therefore be expressed as

$$T(L) = \frac{I(L)}{I_0} = \frac{|\Psi(L)|}{|\Psi_0|} = e^{-2k\beta L} \quad (2.7)$$

which is the well-known Lambert-Beer law[38]:

$$I = I_0 e^{-\mu L}, \quad (2.8)$$

with the absorption coefficient $\mu = 2k\beta$. Additionally, the wave will experience a shift in its phase, relative to a wave propagating in free space[34]:

$$\Delta\phi = \delta k \cdot r. \quad (2.9)$$

At an interface between different materials this difference in the phase results in refraction with the refraction angle[34]

$$\alpha = \frac{\lambda}{2\pi} \frac{\partial\phi}{\partial x}, \quad (2.10)$$

as indicated in Fig. 2.1.

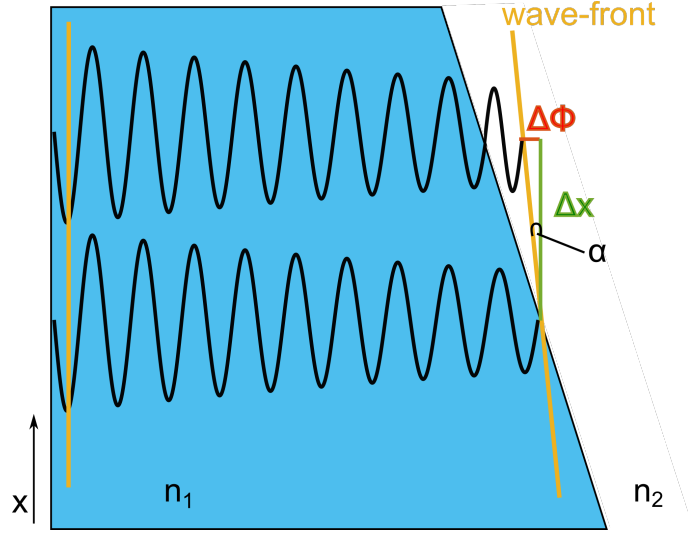


Figure 2.1 Sketch to visualize phase shift: Two waves with a distance Δx are traveling through a wedge shaped sample with the refractive index n_1 . Behind the interface to the next material with n_2 , there is a phase shift $\Delta\phi$ between the two waves as one of the waves was propagating longer through the material n_1 , resulting in a refraction angle α of the wave-front (see Eq. (2.10)).

2.1.3 Free space propagation

So far, we discussed the effects of a planar X-ray wave interacting with matter. However, the wave will also change during a propagation through free space. This is especially important here, as for most imaging methods discussed in this thesis, there is a rather large propagation distance between the sample and the X-ray detector. Generally, the propagated wave-front can be calculated by the *Kirchhoff diffraction integral*[39]. Based on *Huygen-Fresnel's principle* that a wave-front can always be considered as the sum of spherical wavelets $e^{ik \cdot r}/r$, this integral combines all the contributions of these wavelets at a later propagation distance z , yielding[39]:

$$\Psi(x, y, z) = \frac{1}{i\lambda} \iint \Psi(x', y', 0) \frac{e^{ik \cdot r}}{r} \cos(\mathbf{n}, \mathbf{r}) dx' dy' \quad (2.11)$$

with (\mathbf{n}, \mathbf{r}) being the angle between the unit vector \mathbf{n} (pointing in the propagation distance) and the vector \mathbf{r} (pointing from the origin to the corresponding points in the imaging plane). The $\cos()$ accounts here for the intensity distribution. For the two extreme cases of *far-field* (Fraunhofer limit) and *near-field* (Fresnel limit) propagation, several further approximation can be

made to solve this complex integral. The Fresnel number[39]

$$F = \frac{a^2}{\lambda \cdot d} \quad (2.12)$$

is often used to distinguish these two regimes with the aperture size a , the propagation distance d and the illuminating wavelength λ . For $F \ll 1$, the propagation can be approximated by the far-field and for $F \gg 1$, the propagation can be approximated by simple geometric optics. The case $F \approx 1$ can be described by the near-field or Fresnel diffraction approximation. As this approximation is important for the understanding of the wave-optical simulations (see section 2.5), it is derived in detail in the following:

For X-rays, the deflection angles will be very small. Therefore, one can assume that $\cos(\mathbf{n}, \mathbf{r}) \approx 1$ and that $r \approx z$. This is called the *paraxial approximation*[39]. However, in e^{ikr} , r cannot be set to z and a Taylor expansion is therefore applied:

$$r = \sqrt{(x - x')^2 + (y - y')^2 + z^2} \quad (2.13)$$

$$= z \sqrt{1 + \frac{(x - x')^2}{z^2} + \frac{(y - y')^2}{z^2}} \quad (2.14)$$

$$= z \left[1 + \frac{1}{2} \frac{(x - x')^2}{z^2} + \frac{1}{2} \frac{(y - y')^2}{z^2} + \mathcal{O}(x^4, y^4, z^{-4}) \right] \quad (2.15)$$

$$r \approx z + \frac{(x - x')^2 + (y - y')^2}{2z}. \quad (2.16)$$

In the last step from Eq. (2.15) to Eq. (2.16) we used the fact that higher order terms can be neglected. This is called the Fresnel approximation which simplifies the Kirchhoff integral to:

$$\Psi(x, y, z) = \frac{e^{ikz}}{i\lambda z} \iint \Psi(x', y', 0) e^{\frac{ik}{2z}[(x-x')^2 + (y-y')^2]} dx' dy'. \quad (2.17)$$

From a mathematical point of view, this integral can also be seen as a convolution of the incoming wave function $\Psi(x', y', z = 0)$ with a *propagator function* $P(x, y, z)$:

$$P(x, y, z) = \frac{e^{ikz}}{i\lambda z} \cdot e^{i\frac{k}{2z}(x^2 + y^2)}. \quad (2.18)$$

The propagated wave-front is then given by:

$$\Psi(x, y, z) = \Psi(x', y', 0) \otimes P(x, y, z), \quad (2.19)$$

with \otimes denoting the convolution operator. For numerical calculations it is often beneficial to use the *convolution theorem*[36] to substitute a convolution by a multiplication of the Fourier transforms (\mathcal{F}) of the corresponding functions:

$$\Psi(x, y, z) = \mathcal{F}^{-1} [\mathcal{F}\Psi(x', y', 0) \cdot \mathcal{F}P(x, y, z)]. \quad (2.20)$$

This will be used later for the wave-optical simulations.

2.1.4 Talbot effect

In 1836, Henry Fox Talbot[40] discovered that behind a periodic structure (in his case an attenuation grid) which is illuminated by coherent light at certain propagation distances a self-image of this structure occurs. Self image means in this case that the image is formed without the help of lenses or other optical devices. He could further show that these images occur at propagation distances

$$d_T = \frac{2p^2}{\lambda} \quad (2.21)$$

behind the structure with period p and the wave length λ of the illuminating light. This distance is often called the *full Talbot distance*. The theoretical explanation for this effect was given by Lord Rayleigh in 1881[41]. Later, a more detailed analysis of periodically modified wave-fronts showed that also at fractions of this distance the interference pattern still has a high correlation to the initial structure[42–45]. However, only at the full Talbot distance the image is an exact copy of the initial wave-front. In contrast to the full Talbot distance which is only dependent on the period of the illuminated structure and the wave-length, the positions of fractional Talbot distances are also highly depend on the actual shape of the structure/grating[42–45].

2.2 Phase-contrast and dark-field imaging

2.2.1 Motivation

To allow for an imaging method that uses these phase effects and does not solely rely on the attenuation of a sample, different approaches were developed over the recent years[3, 10–12, 46–50]. All these methods have in common that they translate the phase effects, introduced by a sample, into intensity variations which can then be measured by conventional X-ray detectors.

2.2.2 Grating based imaging

Among these methods, grating-based imaging (GBI) methods (i.e. interferometric[3, 10–12, 48] and non-interferometric[49–54] methods) are most promising for clinical applications, as they are compatible with conventional X-ray sources and detectors. A good introduction to these techniques can also be found in the textbook by Als-Nielsen[35].

For the interferometric methods, usually three X-ray gratings (source, reference and analyzer-grating) are placed in the beam path to create a Talbot-Lau interferometer[11]. A non-interferometric modification of the three-grating concept was introduced in [50] and will be studied intensively in this thesis. Other approaches like the non-interferometric coded apertures[49, 55] will not be discussed here.

Besides the phase information, GBI has the advantage of acquiring a third imaging contrast which is based on the *ultra-small-angle-scattering* happening in the sample[12, 56–58]. This signal is often referred to as *X-ray dark-field* (XDF) signal, in analogy to conventional light microscopy. With GBI all three imaging modalities (conventional attenuation, phase-contrast and XDF) are acquired simultaneously. The principles behind the interferometric and non-interferometric approaches of a three-grating-system are discussed in more detail in the following sections.

2.2.2.1 Reference grating

In GBI, a *reference grating* (G1) with a period p_{G1} in the range of a few micrometers and a duty cycle of usually $dc=0.5$ (50% of the surface is covered by the grating bars) is placed in the X-ray beam to create a very fine fringe pattern on the detector (see Fig. 2.2). This fringe pattern can either be realized as the Talbot-self-image which occurs at (energy-dependent) propagation distances T_p downstream of G1 in Fresnel domain[10, 11, 47] or directly as the immediate geometric shadow of a binary-attenuation grating[50].

Given a sufficient attenuation efficiency of G1 with respect to the underlying X-ray energies, the geometric shadow is independent of diffraction and thereby spectral effects. This approach has a significant advantage compared to “conventional” Talbot-Lau interferometers, which typically rely on a phase-grating¹; here the fringe contrast strongly decreases with increasing beam polychromaticity, as T_p is energy dispersive (if G1 is realized as a phase grating, the induced phase shift is also energy dispersive). However, the attenuation-grating approach requires rather compact systems, as

¹Please note: Also for three attenuation gratings, a Talbot self-imaging effect would occur, however this would happen at much longer propagation distances[35].

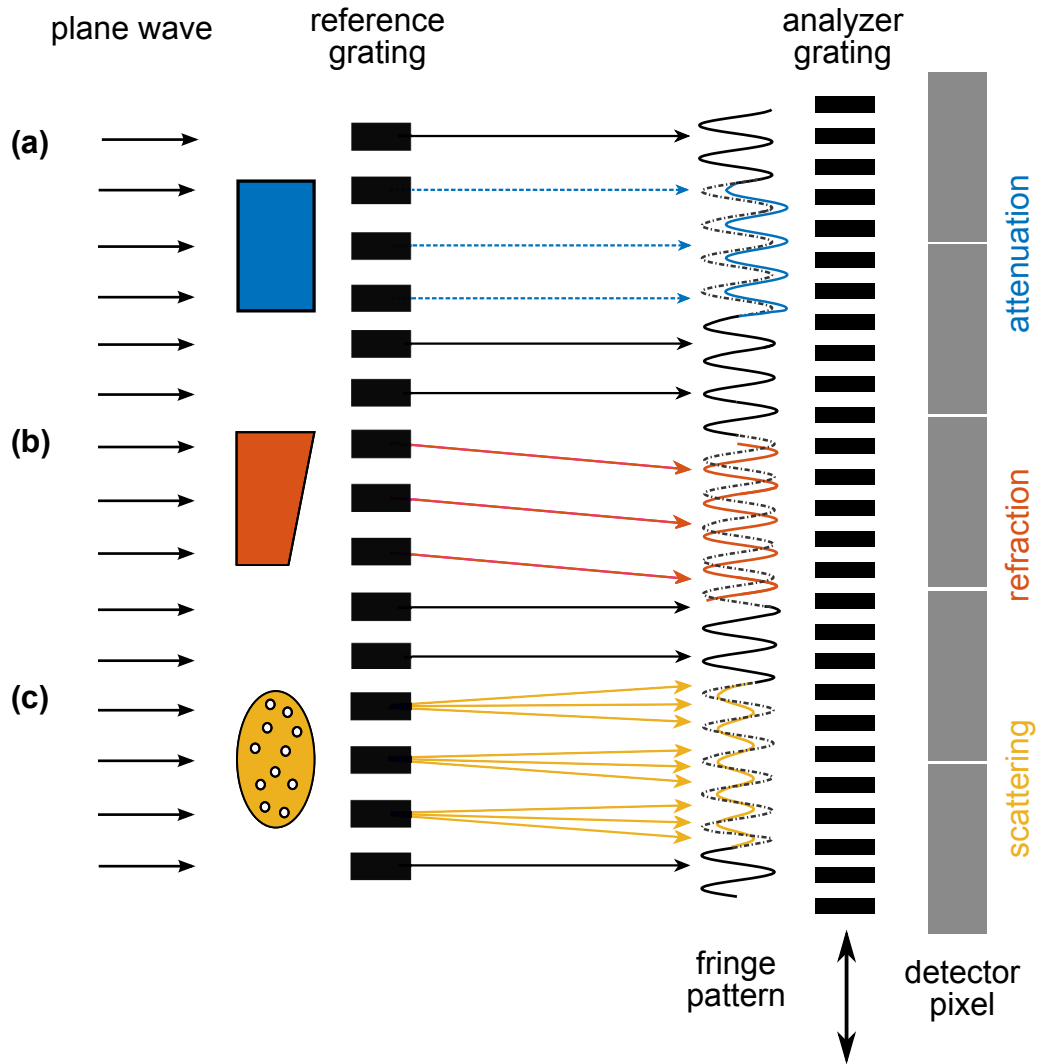


Figure 2.2 Schematic of a GBI system: Three different types of objects are illuminated by a plane wave. In case of a purely attenuating object (a), the fringe pattern created by the reference grating is just attenuated globally. A phase shifting object, like a wedge (b) will result in a lateral shift of the fringe pattern and a scattering object (c) will reduce the contrast of the fringe pattern. The analyzer grating samples the very fine fringe pattern and allows to record the stepping curve with a lateral shift of the grating over one period. Figure adapted from [59].

the distance between G1 and the analyzer grating G2 (see below) has to be much shorter than the first Talbot propagation-distance. As this comes with a reduced sensitivity (see section 2.2.3) it is the main reason, why almost all systems were designed as Talbot-Lau interferometers with a phase grating in the recent years. In addition, an attenuation-grating as G1 requires a factor of two in flux (and dose if the sample is placed upstream of G1) compared to systems with a weakly absorbing phase grating for G1.

The sample information is extracted in the following way: A purely attenuating sample (Fig. 2.2a) will reduce the mean intensity value of the fringe pattern. A curved surface of a sample will result in a lateral shift in this fringe pattern which is caused by a phase shift of the wave-front (see Fig. 2.2b). The Talbot self-imaging effect allows for a larger propagation distance between the G1 and the actual fringe pattern (compared to an attenuation grating). Without the Talbot self-imaging effect this fringe pattern would be smeared out due to diffraction effects after rather short distances. The large propagation is beneficial for detecting small refraction angles, as they are measured indirectly over the lateral shift of the fringe pattern. For larger distances this lateral shift is magnified for the same refraction angle (see Fig. 2.2b).

The undisturbed contrast of the interference pattern is commonly referred to as the (fringe) visibility V of the system and the XDF signal is subsequently given by the reduction in visibility when a scattering specimen is introduced into the beam path (Fig. 2.2c). For an ideal system this visibility would be 1, meaning that there is a black and white contrast for the fringe pattern. In reality such values are usually not achieved and visibilities above 30 % are already considered to be quite high.

2.2.2.2 Source grating

If the reference grating would be illuminated with a conventional X-ray tube, one would not observe any of the effects discussed above. For the interferometric approach, this is the case, as an X-ray tube (see section 2.3.1) is absolutely incoherent, which means that the wave-front reaching the grating does not have a defined phase. In consequence a periodic phase modulation caused by G1 is not possible. To solve this issue the so called *source grating* (G0) was introduced in [11]. The idea of this grating is to virtually slice the large, incoherent focal spot of the X-ray tube into an array of mutually coherent slit sources. Additionally, the periodicity of this grating is chosen as

$$p_{G0} = p_{G1} \cdot \frac{L}{d} \quad (2.22)$$

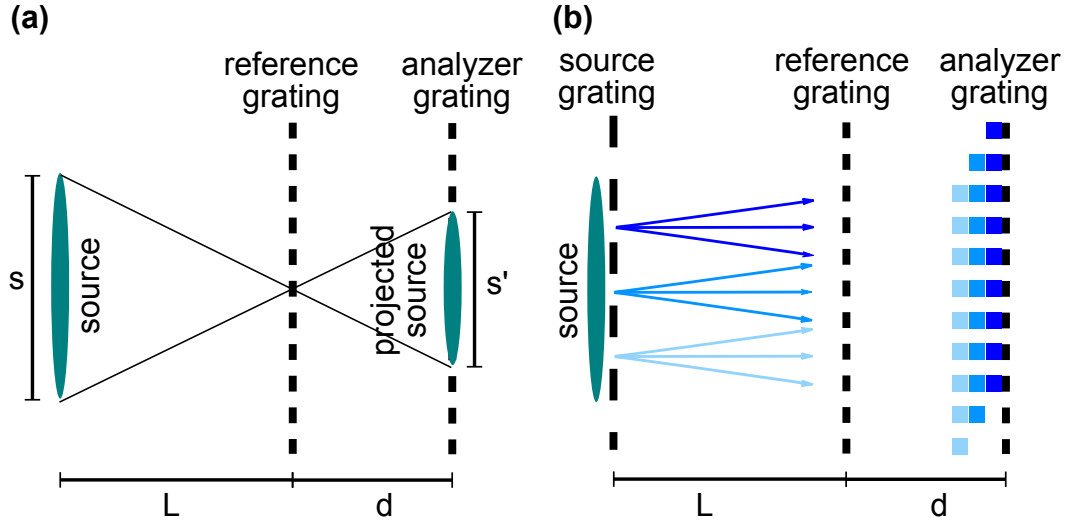


Figure 2.3 Effect of G_0 : Without a source grating (a) the fine fringe pattern would be blurred out by the projected source size. With a source grating of the right periodicity (b) the contributions of the individual slots add up constructively at the analyzer grating and a blurring of the fringe pattern is prevented. Figure adapted from [60].

to guarantee that all individual slit sources sum up constructively at the position of the image of the G_1 (L and d are defined as the distanced between G_0 - G_1 and G_1 - G_2 respectively). Otherwise, this fringe image would be simply blurred out. This principle is shown in Fig. 2.3. The blurring is also the reason, why the G_0 is needed for the non-interferometric approach discussed above. A larger value for the duty cycle of the G_0 grating will usually result in higher visibilities, however comes with a reduction in photon flux[60] and other problems (see section 3.2.1.2).

2.2.2.3 Analyzer grating

As the very fine fringe pattern of G_1 is usually much too fine to be directly resolved by a conventional X-ray detector, the *analyzer grating* G_2 is introduced. This grating has approximately the same periodicity as the image of the G_1 (especially needs to account for the magnification in cone-beam systems). With this G_2 grating the fringe pattern can be sampled now. Combined with a phase stepping[48] or fringe scanning[61] approach (see next sections) the three imaging modalities can be reconstructed.

2.2.2.4 Phase stepping approach

To acquire the data necessary for a reconstruction of the three imaging modalities, one of the gratings is moved laterally over one period p in a step-and-shoot manner, with a minimum of three steps. In every pixel, the intensity $I(x)$, as a function of the grating position x will then follow the so called *stepping curve*[48]:

$$I(x) = a_0 + a_1 \cdot \cos\left(2\pi \frac{x}{p} - \varphi\right) \quad (2.23)$$

with the mean intensity a_0 , the oscillation amplitude a_1 and the phase φ . The contrast of this oscillation is again the visibility:

$$V = \frac{a_1}{a_0} \quad (2.24)$$

An example of such a stepping curve is shown in Fig. 2.4. To reconstruct the three imaging modalities, two scans need to be performed, one with and one without the sample. After a fitting of both scans with the model from Eq. (2.23), the images are given as:

$$\text{Transmission:} \quad T = \frac{a_0^{\text{sam}}}{a_0^{\text{ref}}} \quad (2.25)$$

$$\text{Dark-field:} \quad D = \frac{\frac{a_1^{\text{sam}}}{a_0^{\text{sam}}}}{\frac{a_1^{\text{ref}}}{a_0^{\text{ref}}}} = \frac{V^{\text{sam}}}{V^{\text{ref}}} \quad (2.26)$$

$$\text{Diff. phase:} \quad \Delta\varphi = \varphi_{\text{ref}} - \varphi_{\text{sam}} \quad (2.27)$$

It is important to mention here that the (differential) phase image $\Delta\varphi$ is measured from the phase of the stepping curve, and not from the phase of the wave-front itself.

2.2.2.5 Fringe scanning approach

As the step-and-shoot method does not allow for a continuous scanning of larger samples, Kottler et al.[61] developed a Moiré fringe scanning procedure. In this method, a small mismatch between the G2 period and the period of the fringe pattern is introduced on purpose. This can be achieved for example by a slight detuning in the distances between the gratings. Due to the mismatch in the periods of the two patterns, coarse Moiré pattern will become visible, as shown in Fig. 2.5. The period of the Moiré pattern p_M is defined by the two periods of the projected G1 image p'_1 and the G2 grating p_2 and the angle α between the two[62]:

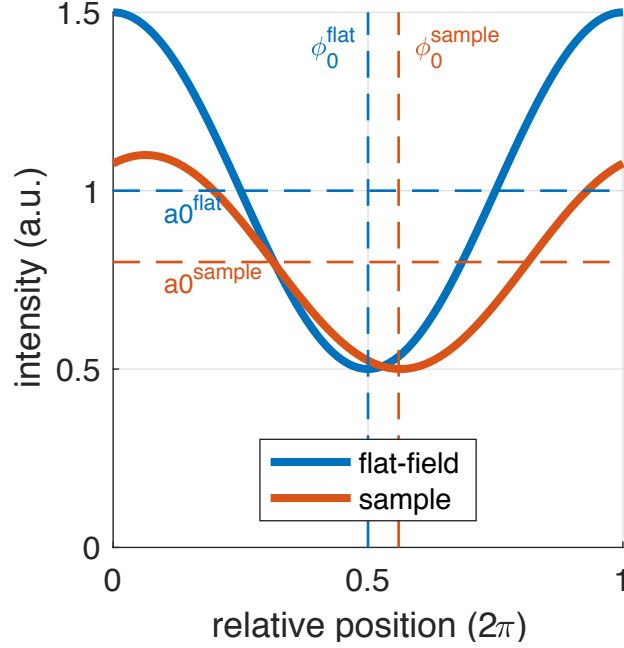


Figure 2.4 Example stepping curve: Two example stepping curves for a flat-field and sample scan. The mean values $a_0^{\text{flat}} = 1$ and $a_0^{\text{sample}} = 0.8$ are marked by horizontal dashed lines. The two curves have a difference in phase $\Delta\varphi=0.4$ which is marked by the dashed vertical lines. Finally, the visibility is for the sample scan only $V_{\text{sample}} = 0.37$ while it was $V_{\text{flat}} = 0.5$ for the flat field.

$$p_M = \frac{p'_1 \cdot p_2}{\sqrt{p_2^2 + p_1'^2 - 2 \cdot p_2 \cdot p_1' \cdot \cos(\alpha)}} \quad (2.28)$$

This Moiré pattern now decodes all possible relative positions of the two gratings. While in the phase stepping approach, the stepping curve is acquired by a relative shift of one of the gratings, a “quasi stepping curve” is acquired in the fringe scanning, by a relative movement of the sample with respect to all (static) gratings. This principle is explained in Fig. 2.6. In Fig. 2.6a an example Moiré pattern is shown. If a sample is moved from position #1 to #5 during the scanning, it will be measured at different positions of this Moiré pattern. After a resorting step, these intensity modulations can be interpreted as the quasi stepping curve shown in Fig. 2.6b. With this stepping curve the same mathematical signal extraction as discussed above, can be performed to obtain the three images (*attenuation*, XDF and *differential phase*).

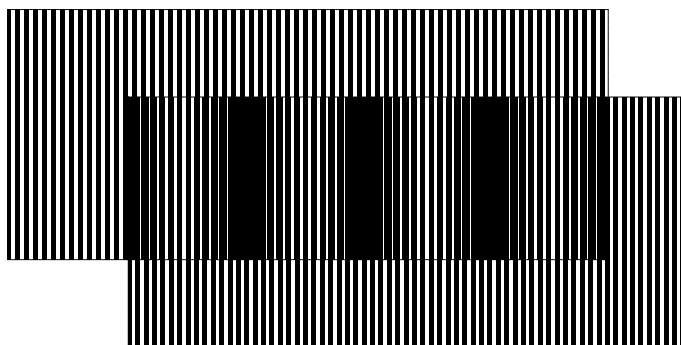


Figure 2.5 Moiré fringe example: The figure shows the resulting Moiré fringe pattern of two line patterns with 16% difference in their period ($\alpha = 0$). For the X-ray gratings, a similar effect occurs.

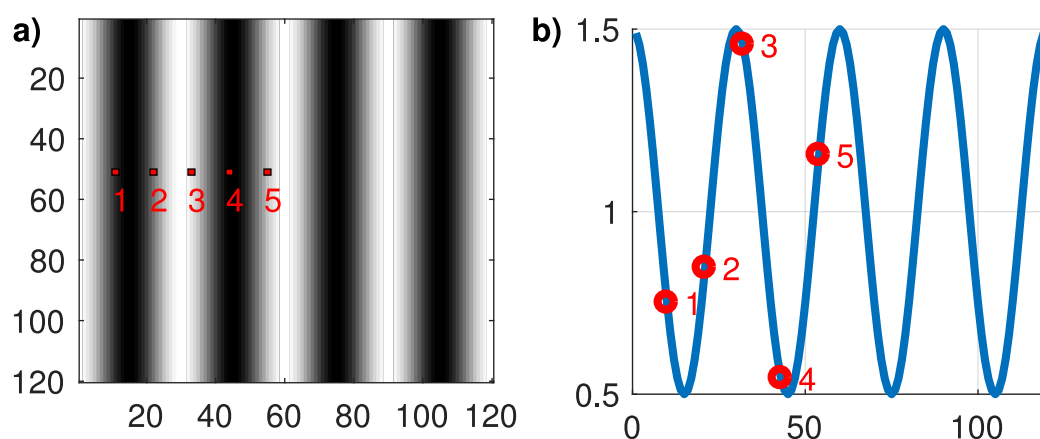


Figure 2.6 Explanation of the Moiré fringe scanning approach: (a) Example Moiré pattern with indicated sampling points for an object being moved from left to right through the pattern. After a resorting step, these intensity modulations can be interpreted as a quasi stepping curve presented in (b).

2.2.3 Phase- and XDF-sensitivity

Two important parameters for a GBI system are the angular sensitivity S , and the correlation length ξ_{corr} . The sensitivity S defines the translation of an angular deflected X-ray into a measured signal for the diff. phase [63, 64]:

$$S = 2\pi \frac{D_{\text{G2,S}}}{p_2} \hat{=} 2\pi \frac{D_{\text{G0,S}}}{p_0} \quad (2.29)$$

$D_{\text{G,S}}$ is the distance between the sample and the corresponding grating (either G0, if the sample is placed between G0-G1 or G2 if the sample is placed between G1-G2) and p is the period of this grating. The smaller the period and the larger the distance to the corresponding grating is, the higher is the measured phase signal.

The correlation length ξ_{corr} defines the length-scale the imaging system probes the autocorrelation function (ACF) of a given sample [57, 58, 63, 64]. This parameter is usually defined as

$$\xi_{\text{corr}} = \lambda \cdot \frac{D_{\text{G2,S}}}{p_2} \hat{=} \lambda \cdot \frac{D_{\text{G0,S}}}{p_0}, \quad (2.30)$$

which is also dependent on the wavelength λ of the applied X-rays. When a sample is probed at different correlation lengths (e.g. by varying the energy, distances or grating periods), its autocorrelation function can be reconstructed [58, 65]. For most typical samples the XDF signal will become higher, the closer the correlation length of the system is to the feature-size of the sample.

The positions of the gratings (e.g. a symmetric system with equal distances between the gratings, or asymmetric geometries with either G0 and G1 or G1 and G2 being closer together) do not influence the sensitivity as both S and ξ_{corr} are only dependent on a single grating period. However, the other two gratings still have to fulfill [11]

$$p_0 = \frac{L}{d} \cdot p_2 \quad (2.31)$$

and

$$p_1 = \frac{L}{L+d} \cdot p_2 \quad (2.32)$$

which might result in very small or large periods for extreme asymmetric geometries.

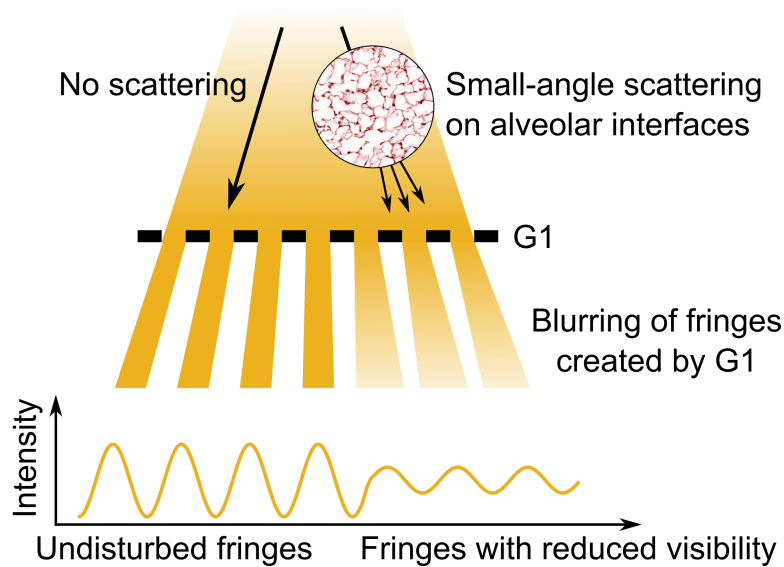


Figure 2.7 Origin of the XDF signal of lung tissue: Multiple scattering on the air-tissue interfaces (as indicated by the histological image) results in a blurring of the fine fringe pattern which is measured as the XDF signal. Adapted version of the figure published in [68].

2.2.4 Dark-field imaging of the lung

The very first in-vivo dark-field images of mice[66] revealed a very strong signal for the lung due to the porous microstructure of the lung tissue. This microstructure is given by hundreds of millions of alveoli which are basically air-tissue interfaces to allow for a proper gas exchange. A histological slice of such a lung tissue is given in Fig. 2.7 together with a schematic explanation why such a tissue creates a strong XDF signal: at every air-tissue interface a small deflection of the X-rays occurs which results finally in a large amount of ultra-small-angle X-ray scattering. Quite soon after the first in-vivo publication, numerous follow-up studies were performed to quantify the possible diagnostic benefit of this new imaging technique, especially for lung imaging. Here the idea was that any lung pathology, which affect the microstructure of the lung, should be much better visible in the XDF images as conventional radiography cannot resolve these structures. Indeed, these studies could show a significant improvement in lung diagnostic by XDF imaging[22, 24–29, 67]. These promising preclinical results with mice are the motivation for this PhD thesis to translate this technology from small animals to animals with thorax dimensions comparable with humans.

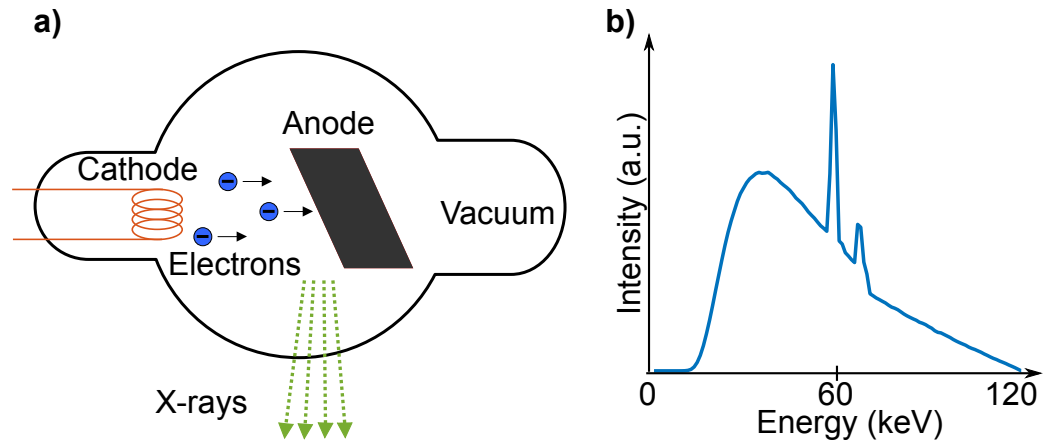


Figure 2.8 Conventional X-ray tube: (a) Schematic of the X-ray tube with the electron being decelerated in the anode material. (b) Spectrum of a conventional X-ray tube with tungsten as an anode material. The Bremsstrahlung spectrum is very broad with a maximum energy of the full acceleration voltage of 120 kVp. Additionally, there are the characteristic lines of the tungsten at $K_{\alpha} = 59$ keV and $K_{\beta} = 67$ keV visible.

2.3 X-ray generation & Detection

For all X-ray imaging experiments at least two components are necessary besides the sample to be imaged; an X-ray source and a detector. Although there are many different (exotic) types of X-ray sources like hot plasmas and synchrotrons, only (conventional) X-ray tubes are discussed in more detail here, as all experiments in the thesis were performed using those devices. For the detection of the X-rays two different types of detectors are discussed in detail; energy-integrating detectors and energy-dispersive photon-counting devices, as both were used during this thesis.

2.3.1 X-ray tubes

One of the oldest ways of creating X-rays is by decelerating fast electrons in a block of material with a high atomic number Z [69]. Usually these electrons are emitted by a glowing filament (the cathode) and then accelerated in a very high electric field between the cathode and the stopping material (anode). This process is sketched in see Fig. 2.8a. This anode is often formed from tungsten due to the high melting point and high Z of this element. However, also other materials like molybdenum, rhodium or silver are used frequently. By the deceleration of the electrons by the atoms of the anode, X-rays are

emitted with a very broad energy spectrum - the so called *Bremsstrahlung*[70]. The emitted X-rays have a very broad energy distribution with a maximum energy of the full kinetic energy $E_{kin} = e \cdot U$ of the incident electrons. e is here the elementary charge of $1.602 \cdot 10^{-19}C$ and U is the electric potential between the cathode and the anode. This voltage is typically in the range of a few ten to hundred kilovolts. Additionally, there can be characteristic X-ray peaks in the spectrum (see Fig. 2.8b), caused by fluorescence in the anode material. Here, an incoming electron excites a bound electron of one of the inner shells of the atoms in the anode. When the atom now relaxes, an electron from a higher shell will fill this vacancy and the energy difference will be emitted as an X-ray with a very discrete energy[69].

The major drawback of this approach to create X-rays is the rather poor efficiency. The conversion of input electrical power towards the output of X-rays is below 1 % for conventional X-ray tubes[69]. Most of the energy is lost here in form of heat in the anode. This renders high power X-ray tubes technically challenging, especially in terms of cooling of the anode. As an improvement, rotating anodes were invented to increase the area of the anode, where heat is dissipated to allow for much higher powers. Additionally, active cooling can be applied, e.g. by a cooling liquid being pumped through the anode[69].

The size of the area where the electron beam hits the anode material is defined as the area of the focal spot. Larger focal spots allow for higher powers, however will result in an increased blurring in the acquired images. Medical X-ray tubes have focal spot sizes of around 1 mm^2 , but there are also tubes available with spot sizes in the micro or even nanometer range. These tubes are not used for medical imaging, but rather for investigation of very small samples in industry and research due to the very limited flux[69].

2.3.2 Energy integrating detectors

Nowadays, the most common class of medical X-ray detectors are energy-integrating *flat-panel detectors* (see sketch in Fig. 2.9). The working principle of these detectors is explained here in detail, based on the textbook by Willmott[36]. As these devices cannot convert the X-rays to an electronic information directly, several intermediate steps are applied in these detectors. First, the X-rays are converted to visible light in a scintillating material. After excitation of the atoms in these scintillator crystals with the incident X-rays, there is a high chance that these atoms will send out visible light during their de-excitation process. This light is then registered by a pixelized, light sensitive layer directly below the scintillator. This can either be a CCD-camera, or an array of photo sensitive diodes (TFT). As

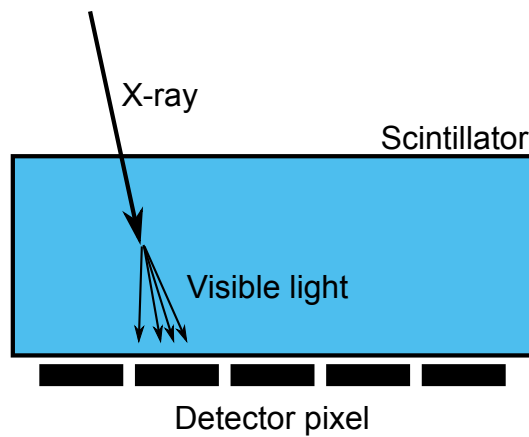


Figure 2.9 Flat-panel detectors: X-rays are first converted to visible light in a scintillator layer and then recorded by a pixelized, photo sensitive layer.

these detectors sum up all the secondary light during a certain integration period, they are called *integrating detectors*. As the amount of secondary light is ideally proportional to the energy of the primary X-ray photon, also an intrinsic energy-weighting is applied. Additionally, the detector cannot distinguish between different X-ray events, as it only “sees” the amount of secondary light.

Most types of detectors are “blind” for new events during the short time, where the actual electronic readout is performed. Therefore, it is beneficial for dose sensitive experiments to not apply X-rays during this read out time. This can be achieved by digital synchronization of the X-ray detector and X-ray source, to allow exposure in the *X-ray window* only, where the detector is sensitive.

2.3.3 Photon counting detector/ X-ray spectrometer

A completely different class of detectors are *single-photon-counting* devices[36]. These detectors apply a direct conversion of the incident X-ray into a measurable electric charge inside of a semi-conductor layer (see Fig. 2.10a). Advanced versions of these detectors are further able to discriminate the energy of every incoming X-ray photon by comparing the measured charge against a reference (see Fig. 2.10b). However, there are only quite a few examples (e.g. the Philips MicroDose system) where this technology is already implemented into medical products as these detectors are still quite expensive, especially for larger sensitive areas. For low dose applications they provide superior noise properties, as they do not suffer from electronic

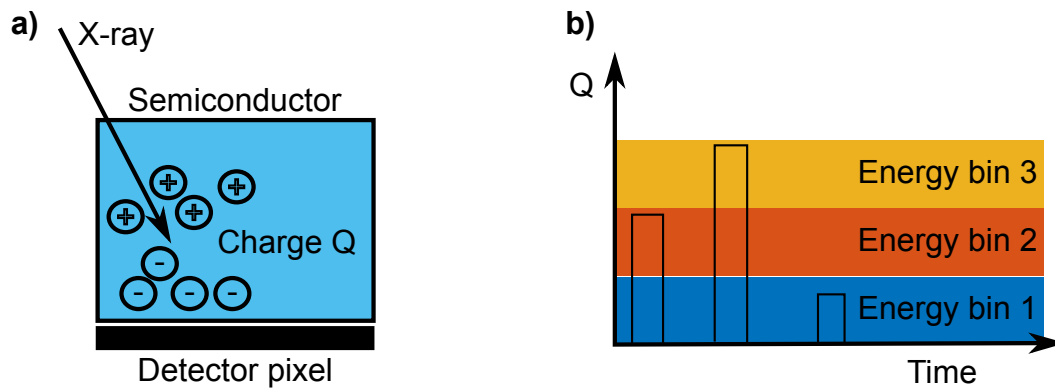


Figure 2.10 Photon counting detectors: (a) Incoming photons are directly converted into an electric charge Q in a semiconductor layer. This electric charge is then collected and compared to different thresholds (b). Based on these thresholds the individual events are grouped into different energy bins. To be able to distinguish individual X-ray photons, this readout needs to be very fast.

read-out-noise like the flat-panels[71]. The multi channel, energy-resolving feature is mostly used in industrial applications of X-ray spectrometers[72] with a single pixel, but also for medical applications first test with multiple energy bins are performed[71]. However, for imaging applications only a very small number of energy bins is usually used, compared to several thousand energy bins available for the single pixel X-ray spectrometer. The main reason here is that every energy bin will only get a fraction of the available photon, resulting in increased noise in these sub-images[71].

2.4 Dosimetry

As X-rays are ionizing radiation, they are potentially harmful for any living being[73]. For the developed prototype it was therefore a major task to minimize the radiation exposure as much as possible to meet clinically compatible values.

The danger of the X-rays for living cells was discovered much later than the X-rays itself[69]. In the early 20th century there were X-ray devices available for entertainment at parties or for example at the shoemaker to check the fitting of shoes[69]. Radiation protection was, at this time, of no concern. Over the years this was stopped when the ionization effects of X-rays were investigated more and more. Today, X-rays are regulated by law in Germany[74] and most other parts of the world. Due to their invaluable contribution to modern medicine and technology it is still legal to apply X-rays to humans and other living beings, however the benefit of the X-ray image has to outweigh the damage of the exposure.

But how can the damage by X-rays or the risk of damage to a living being be measured? The answer of this question will be discussed in the following sections, however is still part of active research. Especially the radiation protection guidelines for the thresholds have become much stricter in recent years[75, 76].

The basic idea behind radiation protection is the limitation of the applied radiation dose to human beings (and animals). However, the measurement of this radiation dose is not straight forward and often even completely impossible. Here we start with a simple example about the energy content of X-rays adapted from [77]:

100 g chocolate might contain an energy equivalent of about 2300 kJ which would also be sufficient to power a 80 W light bulb for around 8h. However, if the same amount of energy would be applied in form of X-rays to a 80 kg person, this would result in 28.750 Gy[=J/kg] of radiation dose which is around 1000 times the lethal dose.

It is not the pure energy content of the X-ray radiation which renders them harmful but rather their microscopic interaction with living cells[73]. These interactions are mostly related to ionization processes that destroy parts of the DNA in the cells. In the following, a few concepts are introduced on how to measure and classify the “dose” of X-rays on the various stages of their interaction levels.

2.4.1 Air kerma

Most often, the intensity of an X-ray beam is classified by the amount of ionization events introduced in an unit volume of a reference material. This measurement unit is called the (air) kerma which stands for the **K**inetic **E**nergy **R**elaxed per unit **M**Ass and is given in SI units as gray (Gy)[73]:

$$K [\text{Gy}] = \frac{E_{\text{kin}} [\text{J}]}{\text{mass} [\text{kg}]} \quad (2.33)$$

This value highly depends on the material used for the interaction and is therefore most often given for air. It is measured by an ionization chamber which measures the electric current of ionized electrons in this chamber. The drawback of this quantity is the non-linear interaction probability of X-rays with air with respect to typical X-ray energies[73]. Fig. 2.11 shows two tungsten spectra, both scaled to 1 Gy air kerma but once for 120 kVp (pre-filtered with 1.6 mm Al) and once for only 20 kVp (both solid lines). Additionally, there are both spectra filtered with 2 mm of water. While for the 120 kVp spectrum almost nothing happens to the flux (and therefore the measured air kerma), do this 2 mm of water filter about half the flux and almost 90% of the measured air kerma for the 20 kVp spectrum. The measured air kerma makes therefore only sense, if the underlying X-ray spectrum is known. This non-linear behavior renders the air kerma a very un-intuitive measurement quantity. However it is still broadly used, as it is easily accessible.

2.4.2 Energy dose

Much more intuitive would be a direct measurement of the *energy dose*, defined as the stored (radiation) energy per unit mass (also given in Gy), in a certain sample[73]:

$$D[\text{Gy}] = \frac{\text{absorbed energy} [\text{J}]}{\text{mass} [\text{kg}]} \quad (2.34)$$

However, most dense sample of interest do not allow for such a direct measurement, as they are not “a measurement device” itself. For most applications the *energy dose* can therefore only be calculated or deducted from other measurements.

2.4.3 Equivalent dose

Besides X-rays, there are many more sources of ionizing radiation, like alpha or beta radiation, neutron radiation and other particles. All these particles

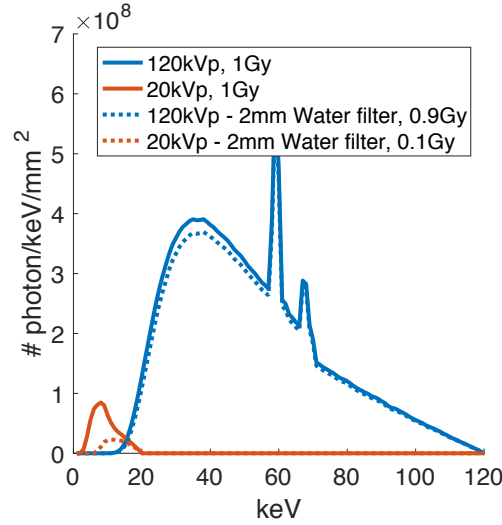


Figure 2.11 Air Kerma: Two X-ray spectra with the same amount of air kerma, however completely different shapes. Therefore, the measured air kerma has always to be given together with an information about the underlying X-ray spectrum.

have different microscopic ionization properties, mostly related to the number of ionization events per path length and the number of energy transferred per event. To account for their different harmfulness to living tissue, an *equivalent dose* H was introduced which is given in Sievert (Sv)[73]:

$$H[\text{Sv}] = w_R \cdot D. \quad (2.35)$$

The weighting factor w_R is simply 1 for all kinds of photons and becomes 20 for e.g. alpha particles, to account for their increased damage to living cells[73]. However, this factor is purely empirical.

2.4.4 Effective dose

Not all types of tissue react to radiation in the same way. There are very radiation sensitive tissues like the lens in an eye and glandular breast tissue and rather robust tissue types like skin. To account for this, the concept of the *effective dose* was developed[73]:

$$\text{ED}[\text{Sv}] = \sum w_T \cdot H_T, \quad (2.36)$$

which is basically a sum of all individual tissue doses, weighted by a factor w_T that takes the radiation sensitivity of the tissue into account. As all the w_T sum up to one, this effective dose ED is used to give the risk for

examination	effective dose	time equivalent
CT-abdomen and pelvis	10 mSv	3 years
CT-chest	7 mSv	2 years
radiography-chest	0.1 mSv	10 days

Table 2.1 Typical effective dose values for different radiological examinations. The time equivalent is given with respect to 3 mSv natural background radiation. The values are taken from the RSNA[78].

radiation induced morbidity, as a large exposure distributed to the full body might result to the same risk of morbidity as a small exposure to a single radiation sensitive organ. These weighting factors are e.g. given in ICRP 103[76]. Typical values for different radiological examinations, as well as their equivalent to the natural background radiation of about 3 mSv are given in Table 2.1.

2.5 Wave-optical simulations

Simulations can serve as an essential tool in the development and optimization of new imaging methods. They allow for a cheap and easy prediction of the performance of an imaging system without the uncertainties usually related with experimental parameters in a lab experiment. However, a simulation can only model reality up to a certain accuracy; the obtained results will therefore be limited by the weakest assumption made in this modeling process. Accounting for the wave-particle dualism, there are two complementary simulation approaches, when it comes to X-rays. Wave-optical simulations which are discussed in the following sub-sections and Monte-Carlo based simulations which account for the stochastic particle nature of X-rays. These types of simulations are discussed in section 2.6. While the wave-optical simulations can account for wave effects like phase propagation and interference, they cannot account for Compton-scattering and vice versa. Therefore, a combination of both simulation approaches is needed to fully model an X-ray system.

For wave-optical simulations of grating-based imaging systems, different approaches have been discussed in literature[79–85]. As major results in this thesis were enabled by wave-optical simulations, their principle and their specific numerical implementation for this thesis is discussed in detail in the following.

2.5.1 Parallel vs. cone-beam geometry

Almost all X-ray imaging systems are cone-beam systems as the rather large detector is illuminated with a point like source (the focal spot). The assumption of a simple plane wave for the X-rays does not hold therefore. However, a numerical implementation of a propagator which accounts for the magnification in the system (so called angular spectrum propagator[86]) is rather complex. A much more simple way is to rescale the system geometry from the *cone-beam* to an equivalent *parallel-beam* system by using the *Fresnel scaling theorem*[33].

The total length of a grating based imaging system can be defined by the distance L between G0 and G1 and the distance d between G1 and G2 via

$$T = L + d_{\text{cone}}. \quad (2.37)$$

The subscript “*cone*” is used here to indicate that the length is measured in the *real lab system*, while the subscript “*par*” will indicate a rescaled length for the calculation and simulation in the corresponding *parallel beam geometry*.

The magnification of the cone-beam system is defined as

$$M = \frac{T}{L} = 1 + \frac{d_{\text{cone}}}{L}. \quad (2.38)$$

According to the *Fresnel scaling theorem*, both the propagation distance as well as the grating period of the G2 have to be rescaled to

$$d_{\text{par}} = \frac{d_{\text{cone}}}{M} \quad (2.39)$$

$$p_{\text{G2,par}} = \frac{p_{2,\text{cone}}}{M} \quad (2.40)$$

to be able to reuse the simple Fourier propagator defined in Eq. (2.18). This allows to model the wave-front as a simple array with constant size, without the need to resample it after every propagation step.

2.5.2 X-ray source & X-ray detector

To model the X-ray source, or more precisely the X-ray spectrum of the source, the software package Spektr[87] was used in this thesis. It is based on the work by Boone et. al[88] which models generic tungsten spectra by polynomial coefficients. Such a spectrum is shown for example in Fig. 2.11. The spectrum S is given as the number of photons per energy bin and mm^2

$$S = n(E). \quad (2.41)$$

The detector is taken into account either as an energy-integrating or photon-counting device with the absorption efficiency of the active layer incorporated into the effective X-ray spectrum.

2.5.3 Wave-front propagation

To simulate a grating based imaging system a plane wave is propagated from the X-ray source to the detector. The simulation is started with a planar wave front which is set to 1 in every sampling point (usually a few hundred sampling points per grating period). During the propagation the interaction of the wave-front with the gratings is taken into account by a multiplication of the wave-front with the complex transmission functions of the gratings. In a first step the planar wave-front is multiplied with the complex transmission function T_{G1} of the G1. An example for such a transmission function

$$T_{\text{G1}}(x, E) = e^{-d(x) \cdot \left[\frac{\mu(E)}{2} - i \cdot k(E) \cdot \delta(E) \right]} \quad (2.42)$$

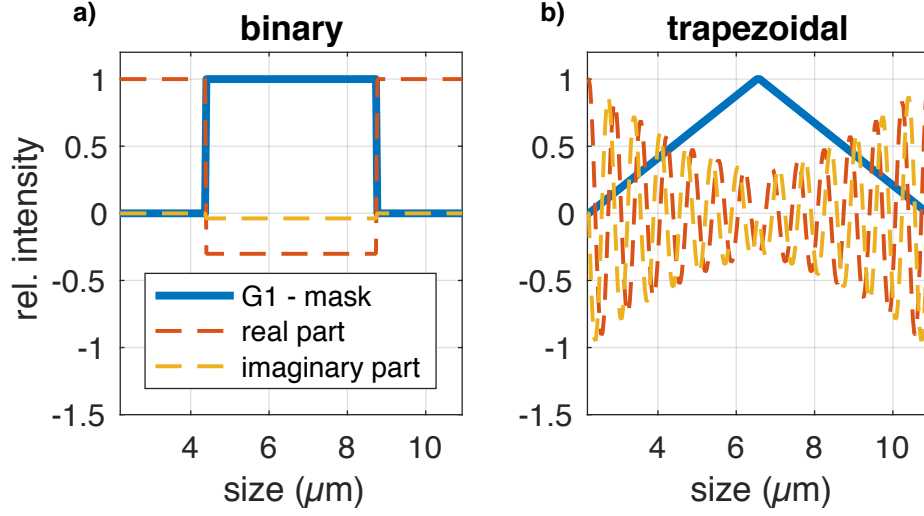


Figure 2.12 Transmission function of G1: Real and imaginary part of the complex transmission function of a G1 gold grating with $170\ \mu\text{m}$ height for $50\ \text{keV}$ photons and (a) rectangular shape and (b) triangular shape.

is given in Fig. 2.12 for different grating shapes $d(x)$ ($\mu(E)$ is the energy dependent attenuation coefficient, $k(E)$ is the wave vector and $\delta(E)$ is the energy dependent refractive index decrement). Usually $d(x)$ is a periodic function with either rectangular steps or a trapezoidal shape. However, in principle, $d(x)$ can have any shape as long as it is periodic.

Using the Fresnel propagator from Eq. (2.18), this wave-front can then be propagated towards the rescaled position of the G2 by multiplying the Fourier transformed wave-front with the Fourier transformed propagator. According to Eq. (2.20) the wave-front is then obtained by the inverse Fourier transform of the result. Such a propagation is visualized in Fig. 2.13. Here a binary G1 with a period of $8.73\ \mu\text{m}$ and a height of $170\ \mu\text{m}$ gold is applied to the planar wave front. The red curve shows the propagated wave-front $23\ \text{cm}$ downstream of the G1 (for $50\ \text{keV}$). The shape of the wave-front is rather complex due to propagation effects. Especially the intensity behind the absorbing gold structures is a result of diffraction/propagation effects. The effect of G0 (with period p_{G0} and duty cycle τ_{G0}) is implemented by a convolution of the propagated wave-front with one period of the projected slot width $w_{G0,\text{proj}}$ (compare Fig. 2.3b) of the G0:

$$w_{G0,\text{proj}} = \frac{d_{\text{par}}}{L} \cdot \tau_{G0} \cdot p_{G0}. \quad (2.43)$$

This results in a further smoothing of the intensity of the wave-front (yellow

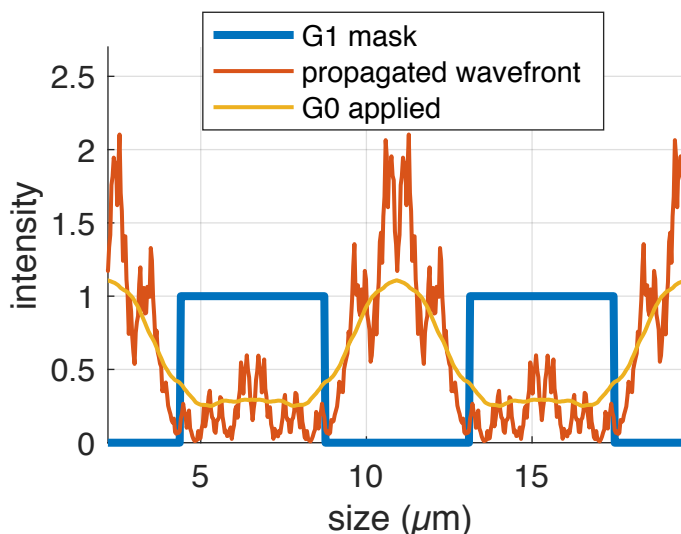


Figure 2.13 Wave-front propagation: A planar wave-front with 50 keV is propagated 23 cm (red curve) downstream of a G1 with 8.73 μm period and 170 μm gold height (blue curve). The wave front has now a rather complex form due to propagation effects. However, after application of the smoothing effect of G0, most of these fine features are gone (yellow curve).

curve in Fig. 2.13). Finally, the wave front is multiplied with the transmission function of the G2 for different relative positions of the G2, similar to a real phase stepping, to obtain the stepping curves. This process is done for all relevant energies individually and the resulting intensity is then given by the sum of effective X-ray spectrum, weighted with the corresponding wave front intensities.

2.5.3.1 Grating imperfections

To account for grating imperfections, such as bridges or not perfectly straight grating lamellas, an additional smoothing of the wave-front can be applied by a convolution with a Gaussian kernel with standard deviation σ_{smooth} . Additionally, the gratings will always have a variation in height, as can be seen in the REM image of one of the G1 grating tiles in Fig. 2.14. To account for this variation, the code implemented for this thesis includes a ripple (in percent of the maximum height) that can be added to the height of the gratings (see Fig. 2.15a). This is a new feature compared to other published wave-optical simulation frameworks[79–85]. This ripple has an interesting effect on the simulation of G1 gratings with very high gold structures. If no ripple is applied, there will be a defined phase shift in addition to the

attenuating effect of the grating bars. This causes an oscillating visibility for different energies, as shown in the simulated visibility spectrum in Fig. 2.15b for two fixed heights of $170\ \mu\text{m}$ and $180\ \mu\text{m}$ respectively. With the additional ripple, these oscillations are gone.

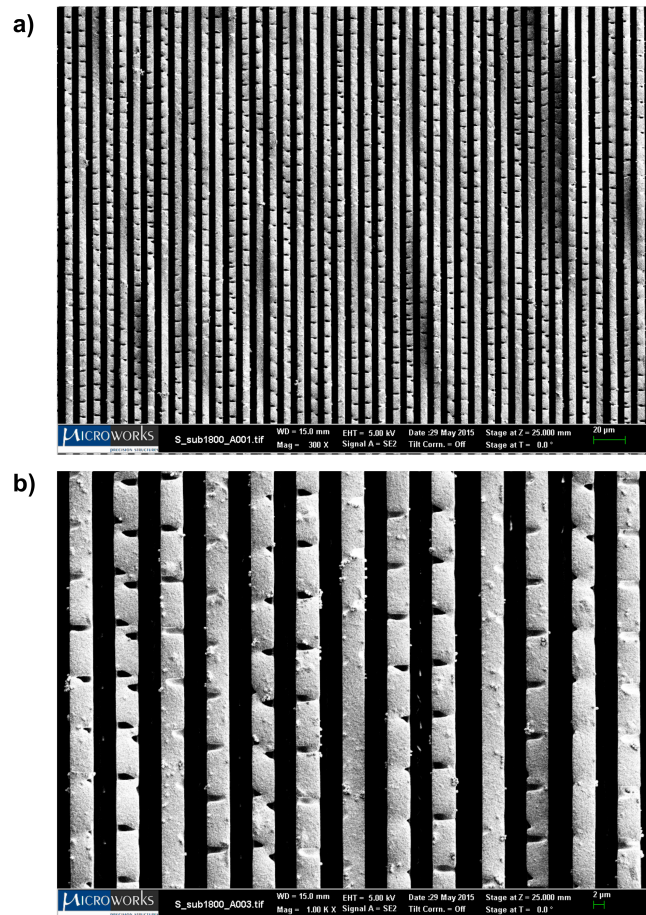


Figure 2.14 REM-images of the G1 grating: (a) Overview and (b) details of a G1 grating with $8.73\ \mu\text{m}$ period and an average height of $155\ \mu\text{m}$. The height of the grating has local distortions of several micrometers. These distortions are modeled with the additional ripple parameter in the simulation.

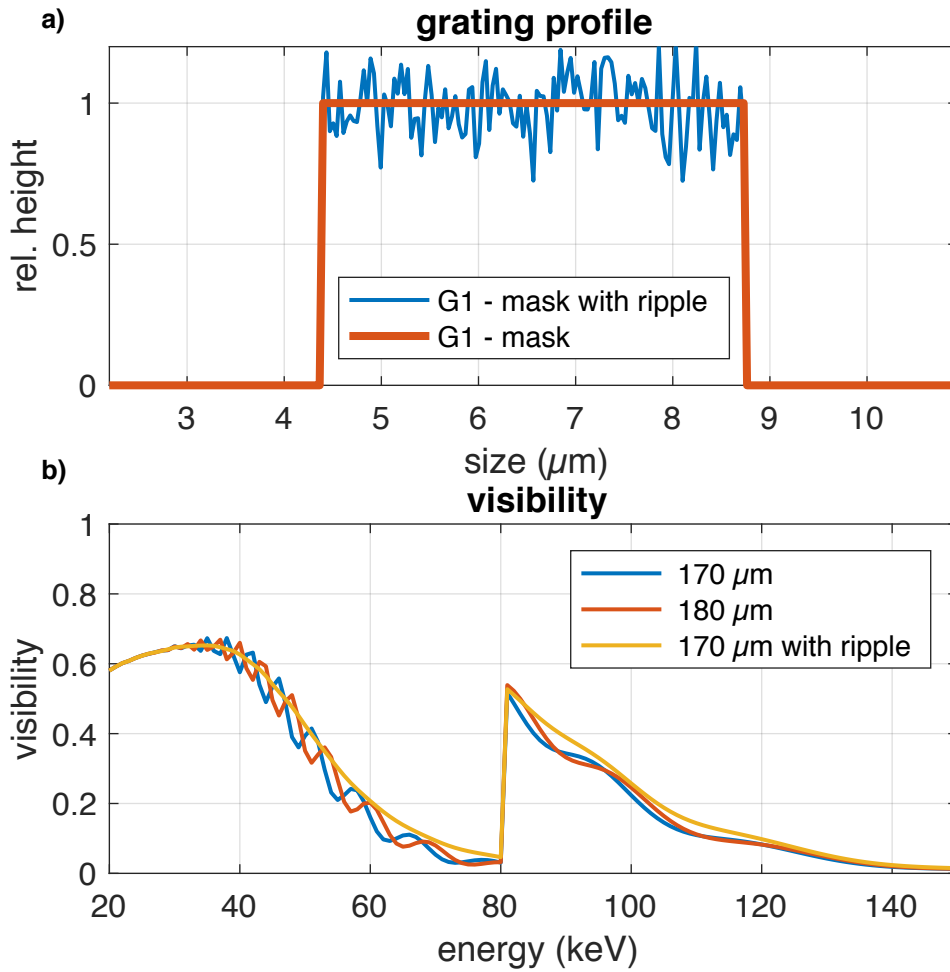


Figure 2.15 G1 ripple: (a) G1 grating with and without an additional ripple of 0.1. (b) Resulting visibility spectrum for a G1 grating with different heights and with additional ripple. The additional visibility oscillations which occur for a fixed grating height vanish as soon as the ripple is included in the simulations.

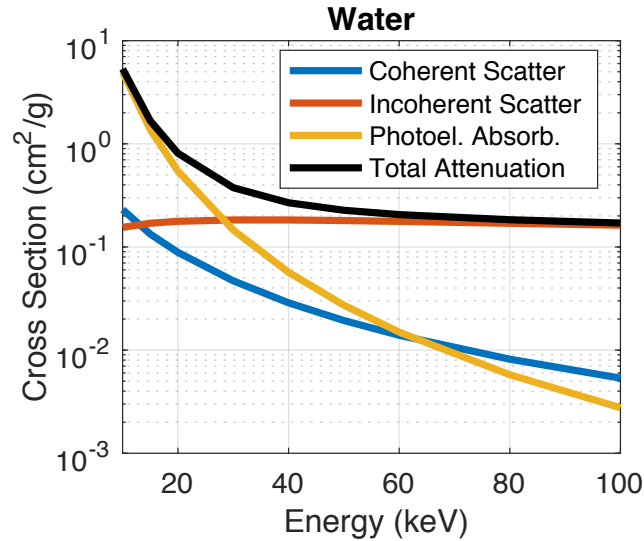


Figure 2.16 Cross sections: The figure shows the different cross sections (= interaction probabilities) for the three main interaction channels of X-rays with water in the energy range between 10 and 100 keV. For lower energies (<30 keV) photo effect is the dominating interaction. For higher energies incoherent Compton-scattering becomes more and more important.

2.6 Monte-Carlo simulations

2.6.1 Motivation

The main difference between wave-optical simulations discussed above and Monte-Carlo based simulations is the stochastic process involved in the latter to account for the particle nature of photons. Monte-Carlo methods are often used to simulate the interaction of particles with matter in high energy physics but are also often used to evaluate the influence of Compton-scattering in X-ray imaging. This is important, as Compton-scattering cannot be modeled with the wave-optical approach discussed above.

2.6.2 Physical model

Each interaction channel of a particle with matter is associated with a certain probability. Most often these probabilities are generated from the measured (or calculated) cross sections for the specific interaction. For X-rays this can be for example the photoelectric effect or Compton-scattering which both have a defined probability to occur per unit length of the object. For water,

such cross sections are given as an example in Fig. 2.16. Below 30 keV, the photoelectric effect is the dominant interaction and above it is the incoherent Compton-scattering. Coherent Thomson scattering has a much lower probability for all relevant energies here.

2.6.3 Simulation framework

The basic concept of the MC-simulation is to shoot a large number of X-ray photons from the source point towards the detector. Each photon is tracked individually and at every sampling point (the precision is limited by the voxel size of the simulated volume), interactions with the atoms of the volume of interest are calculated on a stochastic base. The interaction probabilities are given by the energy of the photon and the elemental composition of the matter at the interaction point. The particles are tracked as long as they are propagating within the volume. Also, secondary particles created by a collision can be considered with most MC softwares. Finally, the particles reaching the defined detector are registered.

A large amount of primary particles (usually 10^{10}) is needed to reduce the influence of noise and to get stochastic robust results. However, this makes these simulations expensive. In this thesis, the Monte-Carlo framework GATE[89] is used. It is basically a wrapper around the famous Geant4[90] framework with the focus on biomedical imaging applications. This framework takes care of all the geometry parameters, the propagation of the photons and all the physical interactions.

Chapter 3

Design specifications of the scanner

In this chapter the design specifications and requirements of the new scanner are discussed in section 3.1. The optimization of the three X-ray gratings under these requirements (based on simulations) is then presented in section 3.2. Further, the concept to obtain a large field-of-view via a slot-scanning approach is elaborated in section 3.3 together with the results of the manufacturing and installation of the large X-ray gratings. Section 3.4 gives an overview of the implemented hard- and software parts of the prototype. Finally, the image acquisition process is briefly explained in section 3.5.

Contents

3.1	Requirements for the new scanner	37
3.2	Grating optimization	39
3.3	Increased FOV by a slot-scanning approach . .	47
3.4	Imaging system	56
3.5	Image acquisition procedure	59
3.6	Summary: Design	60

3.1 Requirements for the new scanner

For the translation of XDF imaging towards the clinic, pigs were chosen as the last step in the process of going from mice to human applications. The porcine thorax anatomy is considered to closely resemble that of humans and pigs are therefore a widely accepted model for translational respiratory medicine[31].

To enable in-vivo chest imaging of pigs, several requirements have to be met:

first, the entire thorax has to be covered which requires a large field-of-view (FOV) of at least $30 \times 30 \text{ cm}^2$. Second, to minimize motion artifacts, the full scan has to be conducted during a single (induced) breath stop, which should not exceed one minute due to animal care regulations. Third, the applied radiation dose should be reasonably low, to be compliant with clinical standards. Finally, the images have to be acquired at clinically relevant energies (typically 60-150 kVp are required to penetrate a thorax for chest radiography). While first applications of high-energy XDF imaging have been carried out as proof-of-principle investigations[21, 91–94], none of the proposed systems satisfied all the above requirements at once.

For the new scanner, a rather asymmetric system geometry as sketched in Fig. 3.1 was chosen with the additional constraint of a maximum system length of about two meters fitting in the experimental hutch. A vertical beam path was favored, as the animals will be scanned during anesthesia and therefore need to be recumbent. As the scanner is designed for imaging of thick lung samples, a rather low XDF sensitivity was chosen to prevent signal saturation in the strongly scattering lung, especially in the lateral projections (compare Fig. 5.2d), where the signals of both lungs are combined. To estimate a useful angular sensitivity S and correlation length ξ_{corr} (comp. section 2.2.3) for the new scanner, the very first XDF measurements of a porcine lung presented in [94], were used as a reference. For the system used in the reference experiments a sensitivity of

$$S_{\text{ref}} \approx 1 \cdot 10^5 \quad (3.1)$$

and a correlation length

$$\xi_{\text{corr,ref}} \approx 0.4 \mu\text{m} \quad (3.2)$$

can be calculated (for 50 keV photons) from Eq. (2.29) and (2.30). Therefore, for the new scanner grating periods of 68.72/8.73/10 μm for G0/G1/G2 were chosen. This parameter result in a similar angular sensitivity and correlation length for a system with a length of 1.8 m and inter-grating distances of 157 cm between G0 and G1, 23 cm between G1 and G2 and the sample being placed on the table 15 cm above G1:

$$S_{\text{new}} \approx 1 \cdot 10^5 \quad (3.3)$$

and

$$\xi_{\text{corr,new}} \approx 0.5 \mu\text{m} \quad (3.4)$$

for photons with 50 keV.

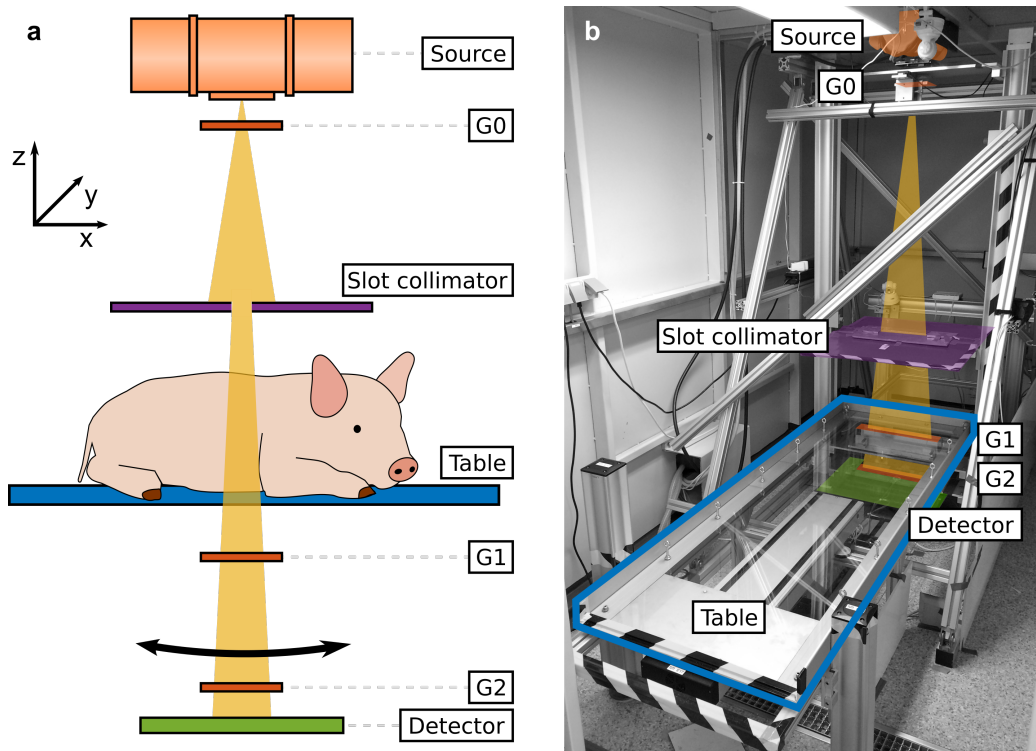


Figure 3.1 Image with schematic of the scanner: Schematic (a) and photograph (b) of the developed scanner with color coded features. The sample (e.g. a pig) is placed on a table made of 6 mm polycarbonate. The x-ray source is mounted on the ceiling and the detector is placed on the floor of the experimental hut. This limits the maximum system length to about 2 m. The G1 and G2 gratings are placed beneath the table and the G0 is mounted close to the X-ray source. To prevent unnecessary exposure, a slot collimator limits the exposed area to the size of the G2 grating.

3.2 Grating optimization

With the grating periods being fixed by the desired geometry and chosen sensitivity, several grating parameters are still free to define. In the following sections, the optimization of the three gratings is therefore discussed in detail.

3.2.1 G0

3.2.1.1 G0 height

Due to the relaxed requirements for the G0 period of about $70 \mu\text{m}$, a larger gold height can be expected for this grating. However, higher gold structures

always come with an increased risk for a failure in the grating fabrication process. To minimize this risk, an optimization study was performed by using wave-optical simulations¹ where the G0 height was varied and the resulting visibility was calculated for different tube voltages (G1 and G2 heights set to 150 μm and G0 duty cycle was set to 0.7, compare next sections). The results of this optimization are shown in Fig. 3.2.

With this approach, the best trade-off between the gold height and the fabrication risk was estimated, as at some point the G0 gold height will not be the limiting factor for the visibility anymore (see plateau in Fig. 3.2 for very high gold structures). Here the other gratings become the bottleneck for the visibility. However, due to the exponential nature of the Lambert-Beer law, it becomes unreasonable from an engineering point of view to aim for such high gold structures, as the gain in visibility is just a few percent, e.g. when doubling the grating height from 200 μm to 400 μm . Finally, to minimize the risk at still quite good values for the visibility, a height of 200 μm was chosen for the G0. If a tube voltage much higher than 70 kVp is anticipated (transmission of 200 μm gold at 70kVp is $T_{70\text{kVp}} < 3\%$), a higher gold structure should be used or a loss in visibility has to be accepted.

3.2.1.2 Duty cycle

The optimal duty cycle of the G0 grating with respect to the visibility was considered in the literature to be as high as possible[95], as no additional dose is applied to the sample for a reduced slit size. However, in reality this value is limited by the available tube power and the measurement time. Extending the work presented in [95], it is shown in the following that there also might be an optimal duty cycle for the case of optimizing the visibility for a fixed sample dose:

If the duty cycle of G0 is chosen too high and if there is a remaining transmission through the grating bars, at some point there will be more “leaked” radiation through the grating bars than through the actual grating slot, as indicated in Fig. 3.3. The quality of the grating can be classified by a quality parameter

$$Q = \frac{\text{intensity behind grating slot}}{\text{total intensity behind grating}} \quad (3.5)$$

However, this quality parameter is not sufficient to describe the performance of the grating, as a G0 with a very small duty cycle would achieve a high Q value, but still a poor visibility due to the small duty cycle. The resulting

¹please see chapter 2.5 on page 28 for more details about the simulations.

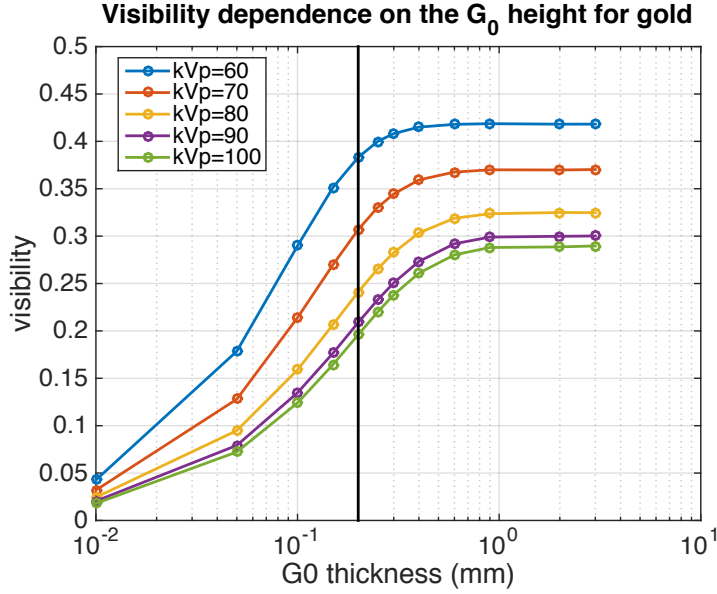


Figure 3.2 Results of the G0 height optimization: The vertical black line is the design height of $200\ \mu\text{m}$. This height was chosen as the best trade off between visibility and possible failure in grating fabrication. For tube voltages of around $60\text{--}70\ \text{kVp}$, $200\ \mu\text{m}$ are already close to the plateau ($T_{70\text{kVp}} < 3\%$) and due to the exponential nature of the Lambert-Beer law, a significant increase in height would be necessary to further improve the visibility here.

effective visibility V_{eff} of a grating based imaging system is therefore given as the visibility of the system with a perfect point source V_0 reduced by a factor $V_{\text{rel,G0}}$

$$V_{\text{eff}} = V_0 \cdot V_{\text{rel,G0}}(h_{\text{G0}}, \tau_{\text{G0}}) \quad (3.6)$$

which takes the height h_{G0} and the duty cycle τ_{G0} of G0 into account (compare to equation (2.63) in [60]) and needs to be computed by wave-optical simulations. This factor might be close to one for a theoretical G0 with infinitesimally small gaps and 100% attenuation efficiency, but will be much smaller for a realistic system, depending on the transmission through the grating bars as shown in Fig. 3.4. These values for $V_{\text{rel,G0}}$ were obtained by the wave-optical simulations. For a grating height of $200\ \mu\text{m}$ and a tube voltage of $70\ \text{kVp}$ a remaining transmission of about 3% of the photon flux can be assumed. As can be seen in Fig. 3.4b, the optimal duty cycle for such a grating would be around 0.8. However, for the actual G0 grating a slightly reduced duty cycle of 0.7 was chosen to improve the flux output a little and

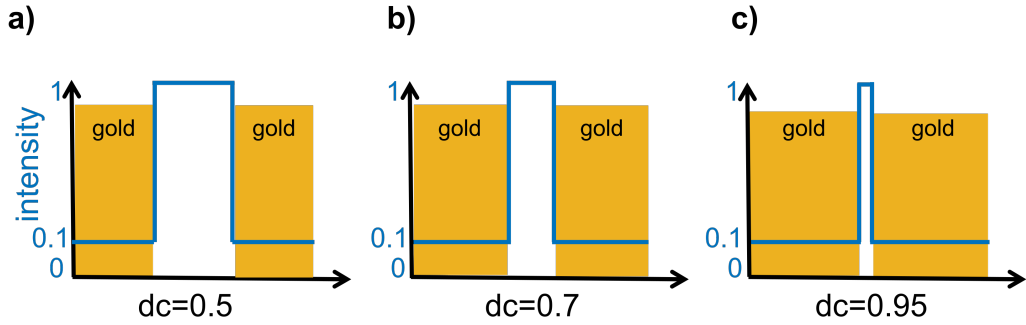


Figure 3.3 *Conceptual explanation of different duty-cycle effects:* The blue curves show the resulting intensity profiles behind the grating (white is air, grating bars are made of gold with insufficient gold height and 10% remaining transmission). (a) For a grating with a small duty cycle of $dc=0.5$, the grating performance is only $Q=0.4$. (b) for an increased duty cycle of $dc=0.7$, the quality is also increased to $Q=0.8$. (c) For the extreme case of a very narrow gap ($dc=0.95$) and 10% remaining transmission through the gold, the grating performance is very poor again with $Q=0.3$.

to reduce the fabrication constraints slightly.

3.2.1.3 Substrate

For the G0 a graphite substrate was chosen as it is beneficial for fabrication of very high structures. As graphite is conductive, no further processing of the substrate is necessary to allow for a galvanization with gold. The application of a thin conductive metal layer, e.g. to silicon substrates might result in decreased quality of the grating structures due to fluorescence events in this metal during the fabrication process. A drawback of graphite as a substrate is its intrinsic microstructure, which can also cause an XDF signal. Therefore, graphite is only suitable as a substrate for a G0 or G2 were the system is not sensitive at all.

The final design parameters of the G0 grating are listed in Table 3.1.

3.2.2 G1

Conventional phase gratings would not work as a G1 in the desired geometry as the first Talbot propagation distance T_p would be much too large (e.g. for 50 keV photons $T_p=1.54$ m for a $\pi/2$ phase-grating with 8.73 μm period). Therefore, in the following paragraph two other approaches are compared

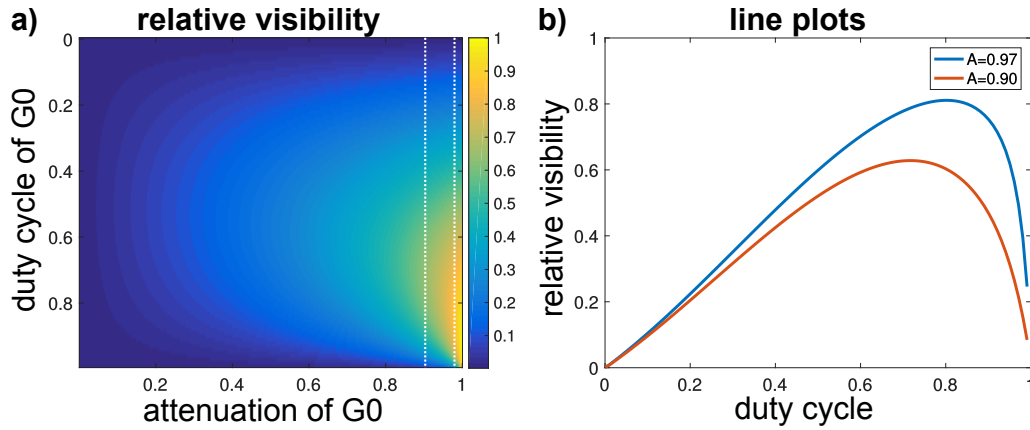


Figure 3.4 Results of the G0 duty cycle optimization: The figures show the relative visibility $V_{rel,G0}$ ($1=no$ loss, $0=$ zero visibility left) with respect to the attenuation efficiency and duty cycle of the G0. (a) Only for gratings with 100% stopping efficiency, the optimal duty cycle will be close to 1 for arbitrary X-ray spectra. As soon as there is any leakage through the grating, a smaller duty cycle is preferred. (b) Line profiles of the two white dashed lines for two realistic example transmission values: $A=0.97$ represents the attenuation efficiency of $200\mu\text{m}$ gold with a 70 kVp tungsten spectrum and $A=0.90$ for a 120 kVp spectrum.

	G0	G1	G2
Substrate	1 mm Graphite	0.525 mm Silicon	0.5 mm Silicon
Period	$68.72\mu\text{m}$	$8.73\mu\text{m}$	$10\mu\text{m}$
Height	$\leq 200\mu\text{m Au}$	$>150\mu\text{m Au}$	$>150\mu\text{m Au}$
Duty-cycle	0.7	0.5	0.5
Active size	$50 \times 50\text{ mm}^2$	$400 \times 50\text{ mm}^2$	$400 \times 50\text{ mm}^2$

Table 3.1 Design specifications for G0, G1 and G2.

in simulations to figure out the most suitable reference gratings for the new scanner.

3.2.2.1 Binary attenuation vs. triangular phase gratings

As discussed in section 3.1 on page 37, an XDF imaging-system with a reduced sensitivity is beneficial for lung imaging. This renders the non-interferometric approach with an attenuation grating as G1 (see section 2.2.2.1) suitable, as this type of system comes with an intrinsic low sensitivity and compact design. However, for the anticipated grating periods and distances some minor diffraction effects will already occur as the system's Fresnel-number F is below 10 for 50 keV photons with a propagating distance of $d = 23$ cm after an aperture of $a = \frac{r_1}{2} = 4.4$ μm . An additional method to reduce the system length for high energy applications was proposed in [96]: By using non binary (e.g. trapezoidal) G1 structures it is also possible to reduce the necessary propagation distance drastically.

To estimate which of these two approaches performs better and which grating parameters would be most suitable for the new scanner, a simulation study was performed with the parameters listed in Table 3.2. Fig. 3.5a and 3.5b show the resulting visibility for binary attenuation gratings and triangular phase gratings for different tube voltages.

To account for the filtering of a human/porcine thorax sample, all X-ray spectra were pre-filtered with 15 cm water. From a fabrication point of view, 150-170 μm gold height was the upper limit which can be reached at the desired period of 8.73 μm at the time of manufacturing the gratings. At this height, the visibility is slightly higher for the attenuation grating approach, than for the triangular phase grating with an optimized height of 26 μm . A further benefit of the attenuation grating is the robustness against changes in the X-ray spectrum. As can be seen in Fig. 3.5c, the performance of the attenuation grating is mostly limited by the K-edge of the gold around 80 keV. The increased transmission for photon energies below this edge leads to a drastic reduction in visibility. A further benefit of these gratings is their robustness against variations in grating height, duty cycle and the overall shape compared to triangular gratings and their broad optimum in the visibility spectrum which reduces visibility-hardening effects (as explained in chapter 4.6 on page 85). In contrast, the triangular gratings are very sensitive to deviations from their ideal shape and even small distortions can lead to a lateral shift of the zero crossing in the visibility curve in Fig. 3.5c. If these negative visibilities would overlap with a fraction of the X-ray spectrum that contains a lot of photons, it would drastically reduce the performance of the system[97]. Preserving the ideal shape of triangular gratings would

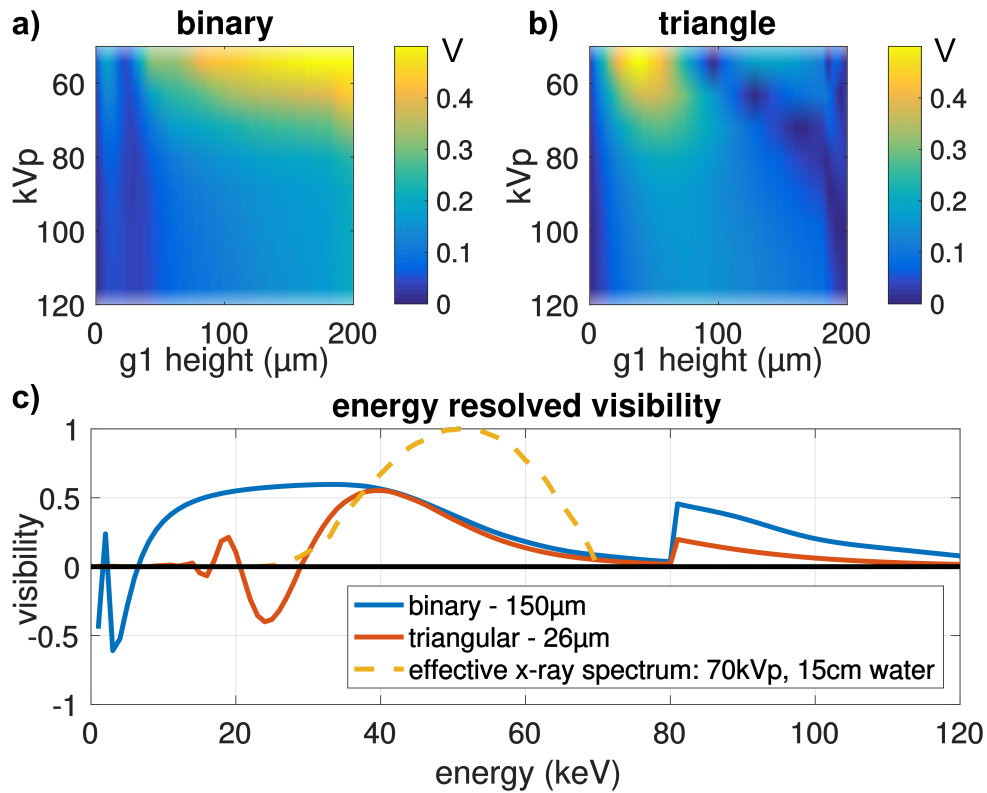


Figure 3.5 Performance of attenuation vs. triangular phase gratings: Simulation of the resulting visibility for binary attenuation gratings (a) and triangular phase gratings (b) for different tube voltages (pre-filtered with 15 cm water). The achievable visibility is slightly higher for the attenuation grating approach, especially for very high G1 heights. (c) Energy-resolved visibility for a realistic height of 150 μm gold for the attenuation gratings and for trapezoidal grating with the optimal height of 26 μm . For the photon energies present in a realistically filtered 70 kVp spectrum (yellow dashed line), these visibilities are very similar. However, the attenuation approach is much more robust against variations in the X-ray spectrum and grating distortions.

	Simulation
G0 period	68.72 μm
G0 height	200 μm Au
G0 duty cycle	0.7
G1 period	8.73 μm
G1 height	0-200 μm Au
G1 duty cycle	0.5
G1 shape	binary/triangular
G2 period	10 μm
G2 height	170 μm Au
G2 duty cycle	0.5
distance G0-G1	1571.4 mm
distance G1-G2	228.6 mm
G1 ripple	0.1
σ_{smooth}	0.075
Detector	600 μm CsI

Table 3.2 Simulation parameters for G1 optimization.

require high demands on their fabrication process and would require a bent implementation into the system. Although they might offer a similar performance in principle, the manufacturing and bent implementation implies much more risks. Therefore, the attenuation grating approach was chosen with the parameters listed in Table 3.1 for the G1.

3.2.3 G2

For the G2 attenuation grating a height of more than 150 μm was specified to limit the leaked photon fluence through the gold bars to less than 5% (for an unfiltered 70 kVp tungsten spectrum). The duty cycle was set to 0.5, although a higher duty cycle would result in a higher visibility. If only phase-contrast and dark-field images are considered, the optimal duty cycle of an analyzer grating G2 can be calculated to be around 0.66[63, 95]. However, this will result in increased noise in the attenuation channel, for the same sample/patient dose. As the new scanner should provide both high quality dark-field as well as attenuation images, a duty cycle of 0.5 was chosen as a compromise. The final parameters for the manufacturing of the G2 grating are listed in Table 3.1.

3.3 Increased FOV by a slot-scanning approach

For the application in chest imaging, a rather large FOV of more than $30 \times 30 \text{ cm}^2$ is required to cover the full thorax in a single scan. However, current GBI systems usually offer only a maximal FOV of about $10 \times 10 \text{ cm}^2$, contingent on the fabrication limitations of the gratings. One simple way to increase the effective FOV is to use multiple exposures and subsequently stitch the obtained images together which results in excessively long scan times and unfavorable movement of the specimen[17, 21, 98, 99]. To overcome this restriction and to increase the FOV, scanning approaches[61, 100] and tiled gratings[101–103] have been suggested. However, no system suitable for in-vivo chest imaging has been presented yet. In the following chapters a new method to overcome this shortcoming is therefore proposed.

3.3.1 Grating alignment & Stitching

Note that some of the results of this section have been jointly published in Schröter, et al., Review of Scientific Instruments (2017)[104]. Figures and text passages in this section may appear similar or identical as in the publication. This is covered by the journals reprint permissions that can be found online under [<https://publishing.aip.org/authors/copyright-reuse>].

To achieve the necessary FOV, a slot-scanning approach was combined with linearly tiled gratings of about $40 \times 2.5 \text{ cm}^2$ for the reference grating G1 and analyzer grating G2. Both gratings are obtained by tiling 8 smaller sub-tiles of $5.0 \times 2.5 \text{ cm}^2$ with the help of a tiling frame[104]. The stitching procedure is shown in Fig. 3.6. The gold structures are created by LIGA processes[105] on conventional 4" silicon wafers with an active size of $50 \times 50 \text{ cm}^2$ (Fig. 3.6a). In the next step, the gratings were cut along two sides and also along the middle line (Fig. 3.6b). The cutting along the middle line was necessary, as not enough gratings were available and the total length of 40 cm could only be achieved by sacrificing half of the slot width (therefore only 2.5 cm rather than the planned 5 cm). The individual grating tiles were then mounted in a sub holder (Fig. 3.6c) which were then assembled in the full frame. These tiles can now be rotated along their z-axis with the help of the adjustment screws.

The strategy to align the individual grating tiles within the assembling frame is explained here in detail for the G2 grating, but was similar for the G1: A single tile of both the G1 grating as well as the G2 were positioned in the middle of the FOV as a reference (see Fig. 3.7a), with the G1 tile covering

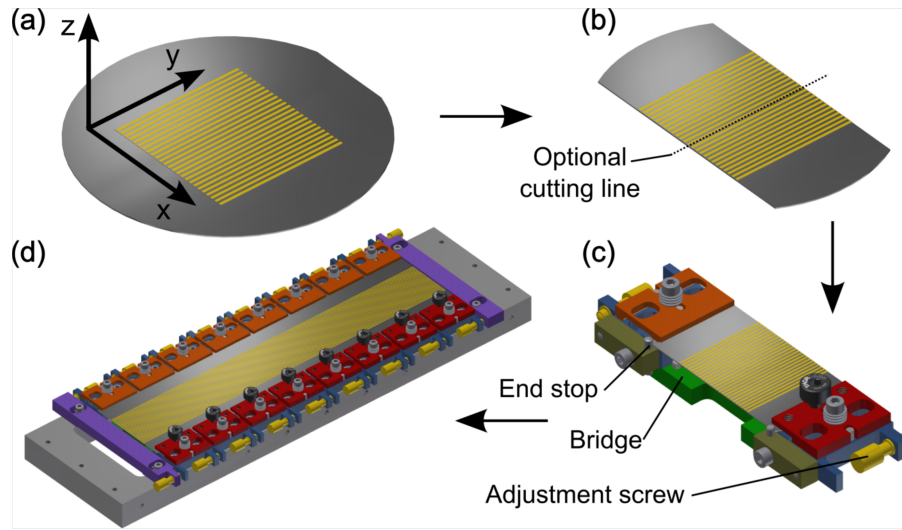


Figure 3.6 Assembly process of the grating tiles in the tiling frame: (a) LIGA structured 4" wafer with $50 \times 50 \text{ mm}^2$ grating area (not to scale), (b) cutting side edges of the grating, (c) assembly of the grating towards end stops in the sub-holder with adjustment screws, (d) assembly of the sub-holders and the frame. Figure and caption adapted from [104].

roughly half of the first G2 tile. Further, the z-distance between the gratings was slightly detuned to show rather large Moiré fringes which is beneficial for positioning of the further grating tiles as discussed below. The neighboring tiles of the G2 were then added successively from the center towards the outside. Every new grating tile was first pre-aligned under a light microscope, to reduce the remaining gap to the previous tile as much as possible, while avoiding direct contact to prevent damage. The fine-tuning of the z-rotation of the new tile was then performed by trying to match the Moiré pattern of the new tile to the one of the reference tile. As both these fringe pattern come from a single G1, the gold lamellas of the two G2 tiles will be parallel if the Moiré pattern are parallel as well (see Fig. 3.7b). This procedure was repeated until the Moiré fringes over the full FOV became collinear (see Fig. 3.8b). Finally, the auxiliary bridges which are used to stabilize the thin wafer during the alignment process, are removed and the gratings are glued to a 1 mm thick polyimide plate (Vespel SEK 3000, DuPont), before they are removed from the assembling frame. A photograph of the final grating is shown in Fig. 3.8a.

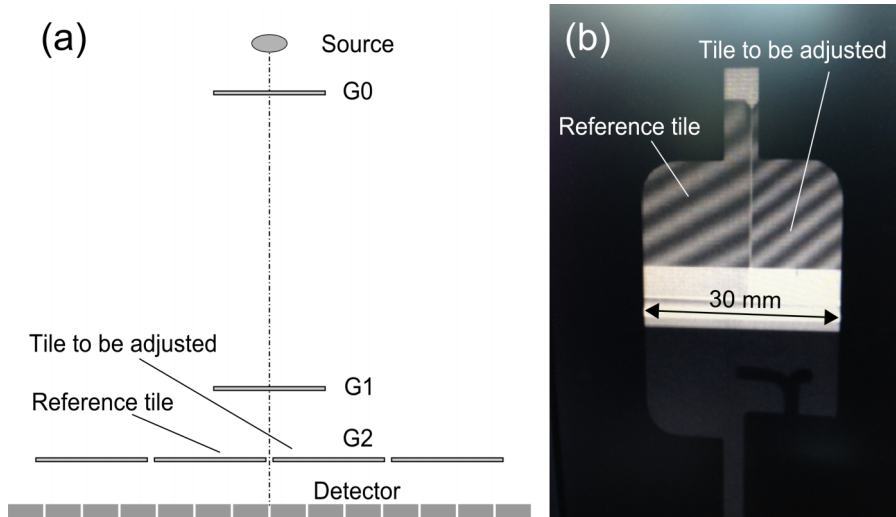


Figure 3.7 Alignment strategy: (a) One tile of G1 and G2 was defined as a reference each, with the G1 tile covering about half of the G2 tile. The rotation of the second G2 tile along the z-axis is now adjusted, to create collinear Moiré fringes across the intersection. (b) The detector raw image with the inter-tile gap in the center of the sub-FOV. The remaining angular misalignment of the tile occurs as a mismatch of the Moiré fringes. Figure and caption adapted from [104].

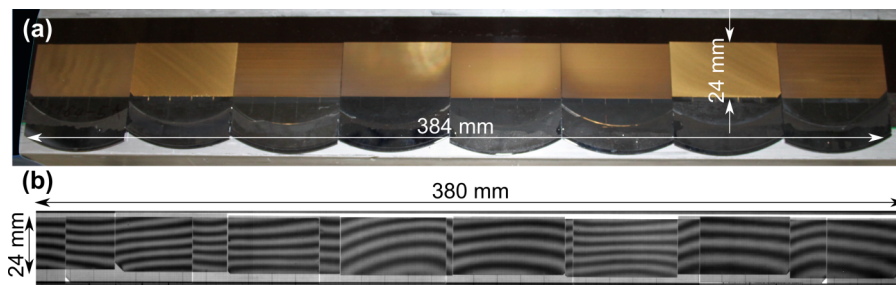


Figure 3.8 Alignment results: (a) Tiled G2 grating with a total structured area of 384 mm × 24 mm. (b) Detector raw image of the aligned horizontal Moiré fringe pattern and the vertical inter-tile gaps. The Moiré fringes are not perfectly parallel lines, as the gratings and their alignment is not perfect. Figure and caption adapted from [104].

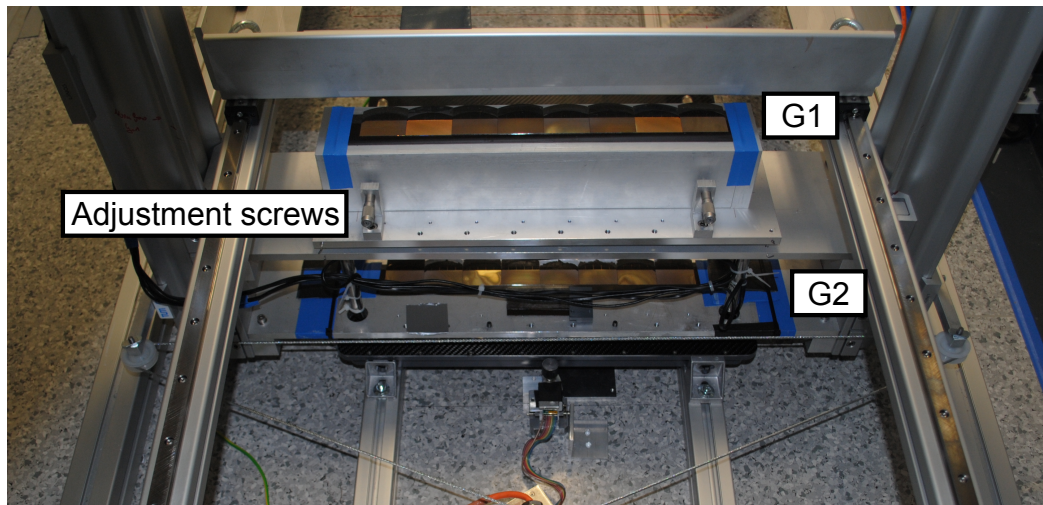


Figure 3.9 Photograph of the implementation of G1 and G2: G2 is fixed to the lowest aluminum plate by the blue sticky tape and allows for no further adjustment. Therefore, G1 can be rotated around the z-axis with the help of four adjustment screws (two on the front and two at the back which are not visible in the photograph) and additionally the height in z of the grating, as well as a tilt in x and y can be controlled by four motorized actuators.

3.3.1.1 Installation of G1 and G2

Fig. 3.9 shows the final installation of G1 and G2 in the system. G2 is directly fixated to the system with no further degree of freedom. To still allow for an alignment of the gratings, G1 has several degrees of freedom. Most importantly G1 can be rotated around the z-axis with four adjustment screws. Additionally, the z-position, as well as a tilt in x and y can be adjusted by four motorized actuators pushing against the bottom of the grating frame. To fixate the frame, strong springs are used.

3.3.1.2 Installation of G0

G0 is mounted on top of two goniometers to allow for a rotation around the z-axis as well as to adjust the y-axis to reduce shadowing artifacts of the G0. In addition, it is connected to a stepping motor which allows for a lateral movement in x-direction. The whole assembly is shown in Fig. 3.10.

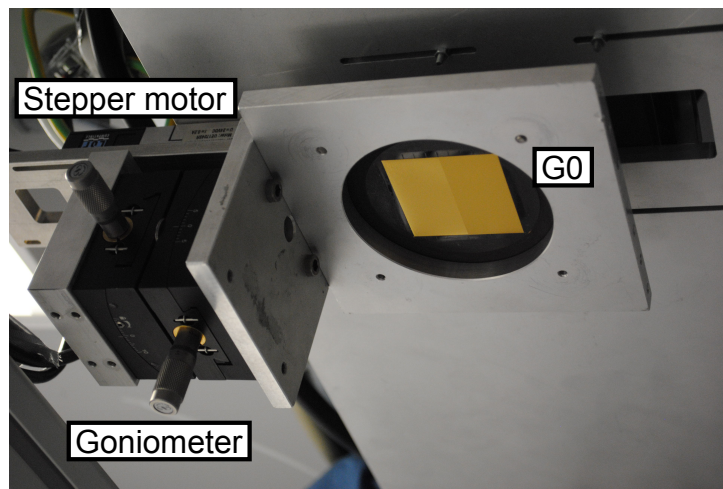


Figure 3.10 G0 mounting: G0 can be rotated around the z- and y-axis with two goniometer heads (see Fig. 3.1 for explanation of the axis). In addition, the grating can be moved by a stepping motor in x direction. The additional lead shielding was removed for this picture.

3.3.2 Swing movement vs. planar movement (“parallax-problem”)

For a slot-scanning system different geometrical realizations are possible:

1. Movement of the sample relative to a fixed system of gratings, detector and source as suggested by Kottler et al.[61].
2. Movement of the gratings and the slit-detector on an arc around the fixed focal spot as implemented in [100].
3. Movement of the gratings and slot collimators on an arc around the fixed focal spot, relative to the fixed sample and a fixed full-field detector (new).

The advantages and disadvantages of these three approaches are discussed in the following: The major issue with approach #1 is the parallax error which is introduced in systems with a non infinitesimal slot width (so basically all realistic systems) as shown in Fig. 3.11a. The red and blue rectangles represent strongly absorbing features, e.g. the ribs in a chest. A system with a total length of $T=2\text{m}$ and a slot width of 2.5 cm has an opening angle of $\alpha = 0.7^\circ$ only, however, for a 20 cm thick sample like a thorax, this already results in a parallax error of above 2 mm (see intensity profile in Fig. 3.11b).

As the Moiré Fringe scanning approach[61] relies on the assumption that all intensity modulations are due to the scanning through the Moiré fringe pattern, this would introduce massive artifacts. Approach No 1 is therefore only suitable for thin samples and/or for systems with very narrow slot widths (e.g. [55, 106]).

Approaches #2 and #3 overcome these limitations and allow for an artifact free imaging, even for an extended slot-width and thick samples. With the arc motion around the fixed focal spot and sample, every point in the sample is always illuminated by the same geometric ray (see orange ray in Fig. 3.11b). This prevents any additional intensity modulation (and therefore artifacts) during the scanning procedure. The main difference between approach #2 and #3 is the detector. In #2 it is realized as a slot detector which is moved together with the gratings and in #3 it is realized as a fixed full-field detector, with only a slot collimator being moved together with the gratings. For #2, an additional resorting procedure is necessary as the data of every point in the sample is measured by different detector pixels. For #3, this constraint does not apply.

The motion speed directly defines the resolution in the images for #1 and #2, while it might affect the visibility in #3, as it would lead to a blurring of the fringes. However, as the fringe period is usually much larger than typical features in the sample, this might be a further advantage of the 3rd approach. A drawback of this approach is however the increased detector size which usually come with increased cost. Further, approaches #2 and #3 limit the FOV to a certain angular range, while approach #1 allows, in theory, for a continues scanning with infinite FOV in the scanning direction. Compared to approach #1, the other two are technically much more challenging, as the gratings have to be moved with no additional vibrations at all.

For the scanner to be developed, however only approaches #2 and #3 are suitable, with the favor for approach #3 as the large detector was already available.

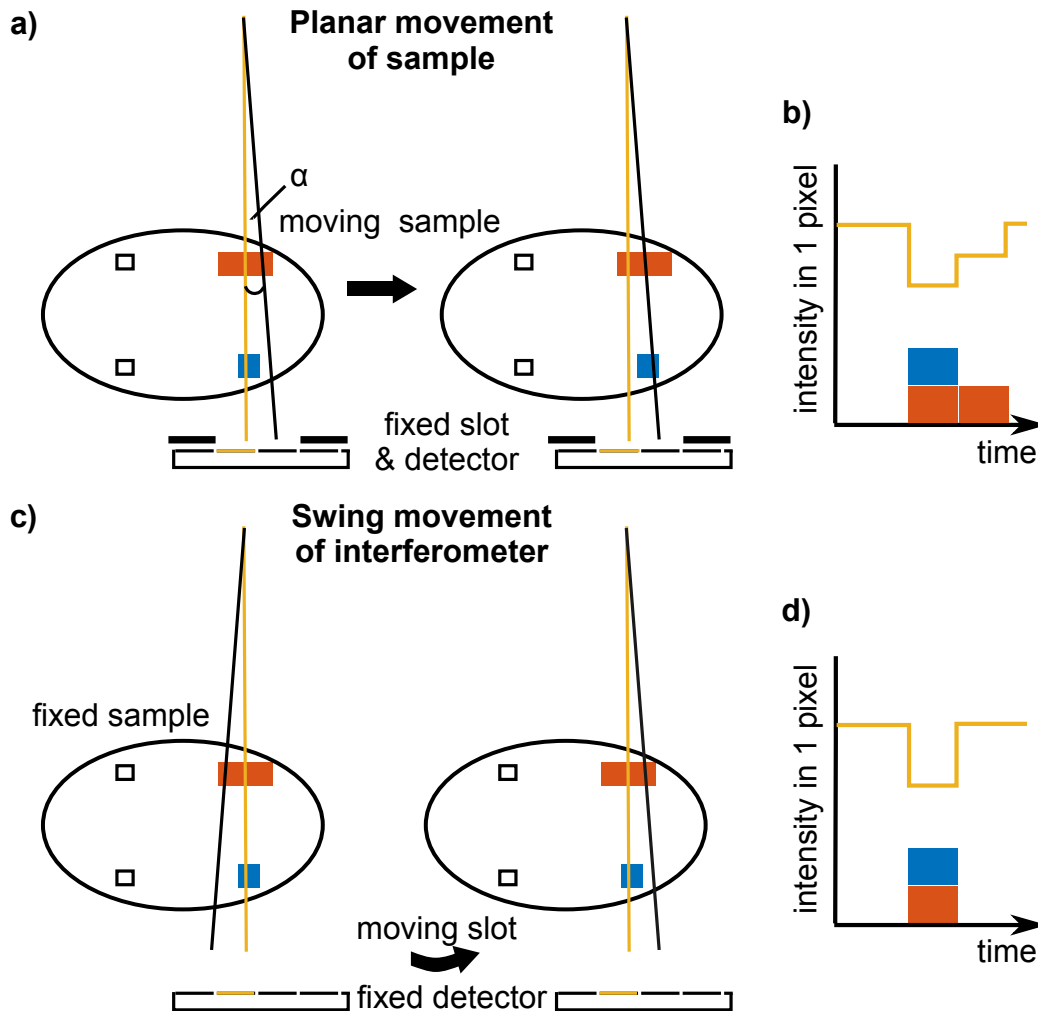


Figure 3.11 Explanation of the parallax problem. (a) Planar movement of the sample, relative to the fixed (slot-) detector. If the sample is very thick and the opening of the slot has a finite width, there will be a parallax-error in the image (see orange intensity profile in (b)). (c) Swing movement of the gratings on an arc relative to a fixed full-field detector and fixed sample. Here no parallax-error occurs, as indicated in the orange intensity profile in (d).

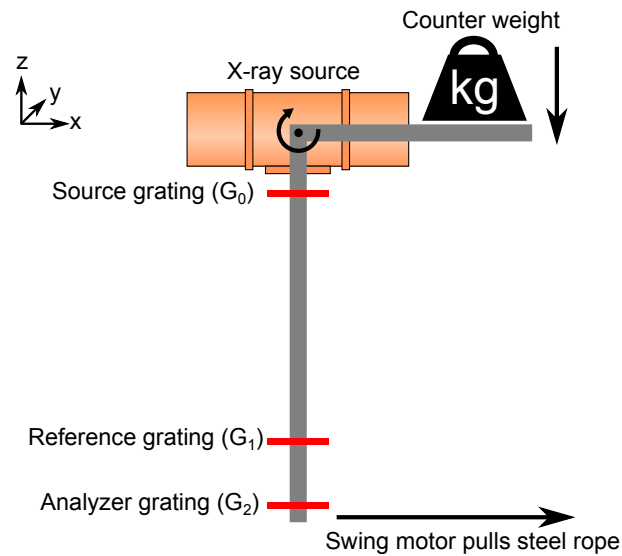


Figure 3.12 Schematic of the motorization concept: A counter weight shifts the rest position to the maximum deflection of the swing. The linear motor which is coupled to the swing via a steel rope, pulls the swing against the gravitation force of the counter weight without an alternation in the load direction. The soft coupling via the flexible steel rope is beneficial for vibration suppression and allows for a conversion of a linear movement to a circular movement without any additional moving parts.

3.3.3 Motorization

To swing the interferometer on an arc, a motorization concept was developed which suppresses vibrations and allows for a smooth movement, without an alternation in the load during the scan motion. The metal frame containing the three gratings is realized in the form of a gallows, with a counter weight at the tip of the upper arm (see schematic of the concept in Fig. 3.12). This counter weight shifts the rest position of the grating frame to the maximum deflection of the swing. Without the counter weight, an alternation in the load would happen in the middle of the swing movement. As it is very challenging and costly to design any backlash free mechanics, this load change would most likely introduce vibrations and unsteady movements and therefore imaging artifacts.

The lower end of the swing is connected to a steel rope which is mounted to a motorized linear stage, as shown in Fig. 3.13. The steel rope fulfills two important tasks: First, it allows a translation of the linear motor movement to an arc motion of the swing, without any further moving parts (a fixed connection would need to allow for a correction of the height during the arc

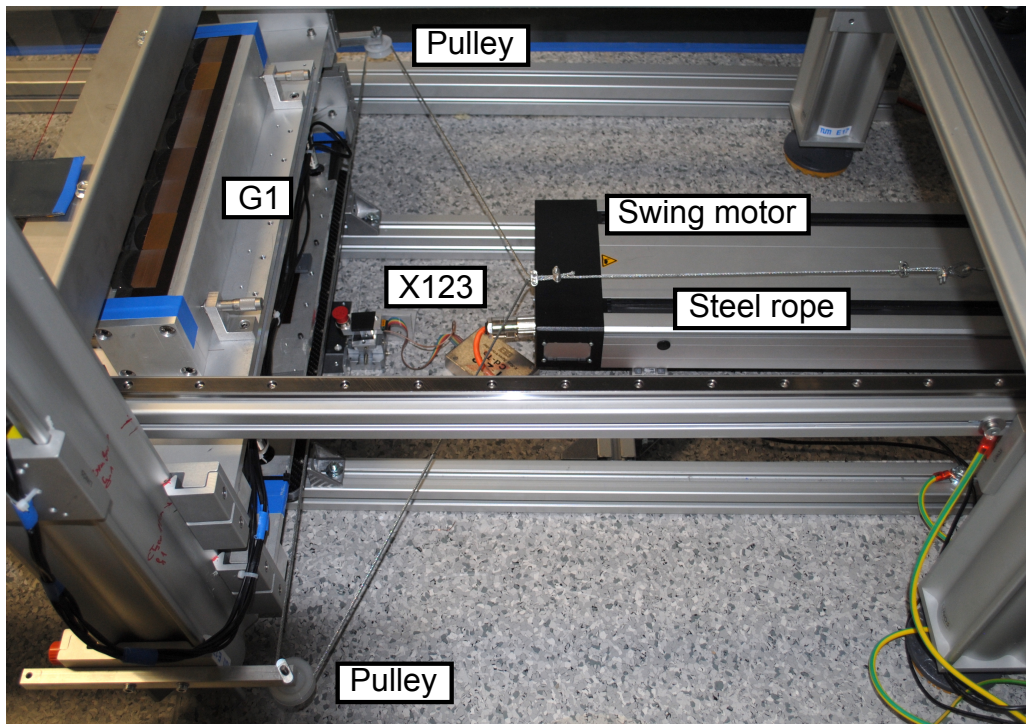


Figure 3.13 Photograph of swing motor: The swing is connected via a steel rope and two pulleys to a linear stage. The steel rope and the pulleys act as a damping, to suppress the vibrations coming from the motor. In addition, also the position of the X123CdTe spectrometer is shown in this picture (see chapter 4.2).

motion). Secondly, the coupling via a rope is very soft compared to a stiff coupling via a fixed axis. This is beneficial for the suppression of vibrations induced by the motor. The effects of these vibrations, introduced by different motor speeds are discussed in section 4.9 on page 102.

3.4 Imaging system

3.4.1 Hardware

3.4.1.1 X-ray tube

For the system, two X-ray tubes were used during the time of this thesis. The first tube was a passively cooled Philips RO 1750 ROT 360 (Philips Medical Systems, Hamburg, Germany). Due to the slot collimators and the additional gratings, most of the X-ray power is “wasted” which resulted in a cooling time of about 45 min between two consecutive high power scans (with 40 s scan time each). To allow for more ergonomically measurement procedures without interruptions due to heat problems, the X-ray source was upgraded to an actively cooled Philips MRC 0310 ROT GS (Philips Medical Systems, Hamburg, Germany) which can be operated at tube voltages between 40-125 kVp with up to 1 A tube current in a pulsed acquisition mode. If not stated differently, all experiments presented in this thesis were performed with the MRC tube.

3.4.1.2 X-ray detector

The detector is a first-generation Pixium RF 4343 (Trixiell, Moirans, France) flat panel detector, with approximately 600 μm of CsI as an active layer. The detector achieves a high readout rate of 12 Hz in a fluoroscopy, 3×3 -binning mode with a resulting pixel size of 444 μm (approx. 360 μm effective pixel size in the sample plane) and only 4 Hz in an unbinned mode. For the fast read-out, the X-ray window for the pulsed exposure is usually 20 ms.

3.4.1.3 Motors

For the precise movement of the G0, a linear MFA-CC stage (Newport Spectra-Physics GmbH, Darmstadt, Germany) is used. Its resolution (approx. 1 μm) is high enough to directly perform a conventional phase stepping approach over the grating period of about 70 μm , without the need for further reduction gears. For the grating alignment mostly micrometer screws were used and only the z-position of the G1 grating is controlled by four TRA12PPD actuators (Newport Spectra-Physics GmbH, Darmstadt, Germany).

The interferometer swing and the large sample table are both moved by LES5 linear stages (isel Germany AG, Eichenzell, Germany).

All the motors are powered by an XPS and ESP motion controller (Newport Spectra-Physics GmbH, Darmstadt, Germany).

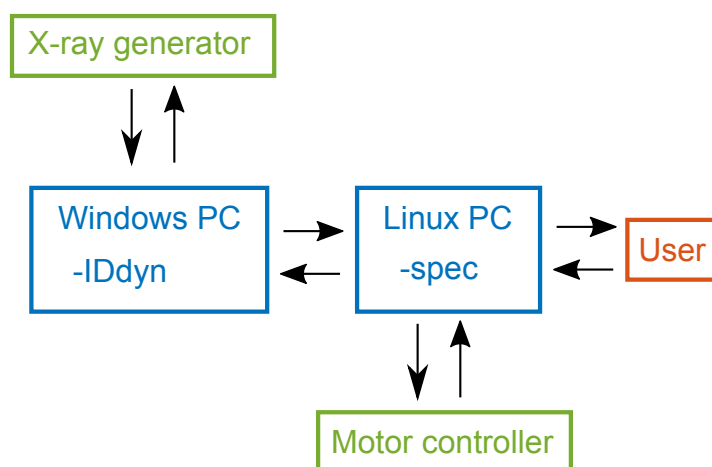


Figure 3.14 Flowchart of the system: Only the main components are shown for simplicity. The user interacts with the software “spec” running on the Linux computer. This software controls all other parts of the system. Most importantly is the communication of spec via Ethernet with the “IDdyn” software server, running on a separate windows PC. This IDdyn server controls all the X-ray hardware. The second important task is the communication between spec and the motion controllers. By using spec as the control master, a synchronization between the motor movements and the X-ray generation is enabled.

3.4.2 Control software

The top-level interaction with the scanner is realized by different macros for the UNIX-based software package for instrument control, *spec* (Certified Scientific Software, Cambridge, Massachusetts, USA). These C-like macros control the movement of all motors, start the X-ray exposures, take care of the communication between the different hard- and software modules and interact with the user as described in the flowchart in Fig. 3.14. In the background, there is an additional windows PC which runs the IDdyn software server to control the actual X-ray generator. All communications are realized via the Telnet protocol (Ethernet).

3.4.3 Lead shielding & Collimators

As explained in section 3.3 on page 47, the system is based on a slot-scanning approach. The slot size is prescribed by the size of the G1 and G2 gratings, however there are several additional collimator present in the beam path. These collimators are necessary for two reasons: The collimators before the actual sample (G0 collimator and the pre-sample slot-collimator shown in

Fig. 3.1), reduce the exposed area exactly to the size of the gratings, to prevent unnecessary dose deposition in the sample. Additionally, there are two to three collimator sets below the sample. One set of collimators around G1 and G2 each and a third one directly placed on the table, if the sample is smaller than the actual FOV (compare Fig. 5.2). These collimators block mostly Compton-scattered photons and are essential to allow for high quality XDF images as discussed in section 4.4.

3.5 Image acquisition procedure

Similar to other phase-contrast imaging methods, also for the new scanner, always two scans (a reference scan and the actual sample scan) are needed to calculate the images of the sample. However, for the new developed fringe scanning approach, the procedures for the reference scan and for the sample scan are quite different. The two scanning methods are therefore briefly discussed in the following paragraphs. An extended discussion of the image acquisition scheme and data processing algorithms will be part of the PhD thesis of Fabio De Marco.

3.5.1 Conventional phase stepping mode

Besides the new fringe scanning approach, the scanner also allows for conventional phase stepping. This is beneficial if smaller samples are scanned or for the measurement of the visibility (e.g. to calculate the amount of beam/visibility-hardening). For the phase stepping, the G0 can be moved over one (or more) periods with the MFA-CC stage.

3.5.2 Slot-scanning

3.5.2.1 Flat-fields

Due to the fringe scanning procedure, every detector pixel i is sampled at different positions x of the gratings. As the gratings are never 100 % homogeneous over the full slot width, there will be variations in the transmission, the phase and the visibility during the scanning procedure. To account for this, an additional phase stepping is performed (by moving G0 over one period) and the fringe scanning is repeated for all positions of the G0. With this approach, it is possible to calculate an individual reference intensity $A_i^{\text{ref}}(x)$, phase $\varphi_i^{\text{ref}}(x)$ and visibility $V_i^{\text{ref}}(x)$ for all relevant relative positions x on the grating with conventional phase-stepping processing algorithms.

3.5.2.2 Sample-Scans

The sample scans are performed with a single swing motion of the gratings across the detector. As the sample scans are usually performed with a much higher tube power, all images are normalized to their individual tube power. The sample transmission T_i^{sam} , phase φ_i^{sam} and darkfield D_i^{sam} can then be calculated by fitting the measured detector intensities to the function:

$$I_i^{\text{sam}}(x) = T_i^{\text{sam}} \cdot A_i^{\text{ref}}(x) \cdot \left(1 + D_i^{\text{sam}} \cdot V_i^{\text{ref}}(x) \cdot \cos(\varphi_i^{\text{sam}} - \varphi_i^{\text{ref}}(x))\right) \quad (3.7)$$

To allow this kind of processing, a precise synchronization of the motor and the X-ray exposures for all scans of the flat-field as well as the sample scan is required.

3.6 Summary: Design

In this chapter, the main design aspects for a novel X-ray dark-field chest imaging system were discussed and the actual prototype was manufactured and assembled.

Gratings The optimal gratings were estimated by comparisons with prior experiments and extensive wave-optical simulations. The simulations showed that a system based on three attenuation-gratings that does not rely on interferometric effects is superior under the given design constraints. Further, it was shown that a system based on conventional phase gratings would not work here and that even advanced grating shapes like trapezoidal gratings are still less optimal for the anticipated prototype.

Large FOV The large field-of-view was achieved by combining a stitching procedure with a slot-scanning approach and a motorization concept for the latter was elaborated. In particular, the effects of parallax errors due to planar movements were discussed and a solution via a swing motion of the gratings on an arc was introduced. The motion concept was designed to suppress vibrations and to be without a backlash in the turn-point of the restoring force acting on the swing.

In the next chapter of this thesis, the performance of the developed prototype is evaluated.

Chapter 4

Characterization of the prototype scanner

In this chapter, the main performance indicators of the developed prototype system are evaluated. First, the basic functionality of the prototype is demonstrated in section 4.1 for the full FOV on a scan of a fruit ensemble. In the next step, the achievable visibility is analyzed (section 4.2) and the optimal tube voltage for thorax imaging is estimated (section 4.3). The reduction of the visibility by Compton-scattering is discussed in section 4.4 and a correction method for the latter is developed and presented in section 4.5. Beam/visibility-hardening effects are discussed in section 4.6 together with their correction approaches. Finally, technical measurements of the applied radiation dose (section 4.7), the achievable image resolution (section 4.8) and the maximum imaging speed (section 4.9) are discussed.

Contents

4.1	Large field-of-view	62
4.2	Visibility	62
4.3	Tube voltage optimization	67
4.4	Visibility reduction by Compton-scattering . . .	71
4.5	Compton-scatter-correction for sample data . .	80
4.6	Beam/visibility-hardening effects	85
4.7	Radiation dose	95
4.8	Resolution limits	97
4.9	Scanning speed optimization	102
4.10	Summary: Characterization of the prototype .	105

parameter	value
FOV	$32 \times 35 \text{ cm}^2$
kVp	70
#shots total	460
#shots per pixel	25
X-ray per shot	20 ms
total scan time	40 s
detector binning	3×3

Table 4.1 Standard slot-scan parameters: Standard parameters for images acquired with the slot-scanning method.

4.1 Large field-of-view

One of the very first samples imaged with the new scanner is the fruit ensemble presented in Fig. 4.1 with the imaging parameters listed in Table 4.1. These parameters are defined as the *standard scan* and are used for all other slot-scanning images in this thesis, unless stated differently. This image was used to analyze the performance of the new scanner over the full FOV. As the sample is placed on the table level, it will get magnified on the detector and the width of the FOV will therefore be smaller than the 40 cm of the G1 grating. In total a FOV of $32 \times 35 \text{ cm}^2$ was achieved and the three imaging modalities could be retrieved for the full image without major artifacts.

To highlight that the new design concept with three attenuation gratings is indeed able to measure XDF signals, the tip of the banana was squeezed a few hours prior to the experiment. This treatment destroys the cellular structure of the banana which then results in a loss of dark-field activity (Fig. 4.1b). The attenuation signal (Fig. 4.1a) however remains unaltered as no material was removed. The differential-phase signal (Fig. 4.1c) shows mainly the edges of the fruits.

This simple experiment validated that the basic concept of the scanner is working and that artifact free retrieval of the three imaging modalities is feasible.

4.2 Visibility

4.2.1 Motivation

The (fringe) visibility is one of the most important system parameters as it is inversely proportional to the image noise in the XDF and phase-contrast

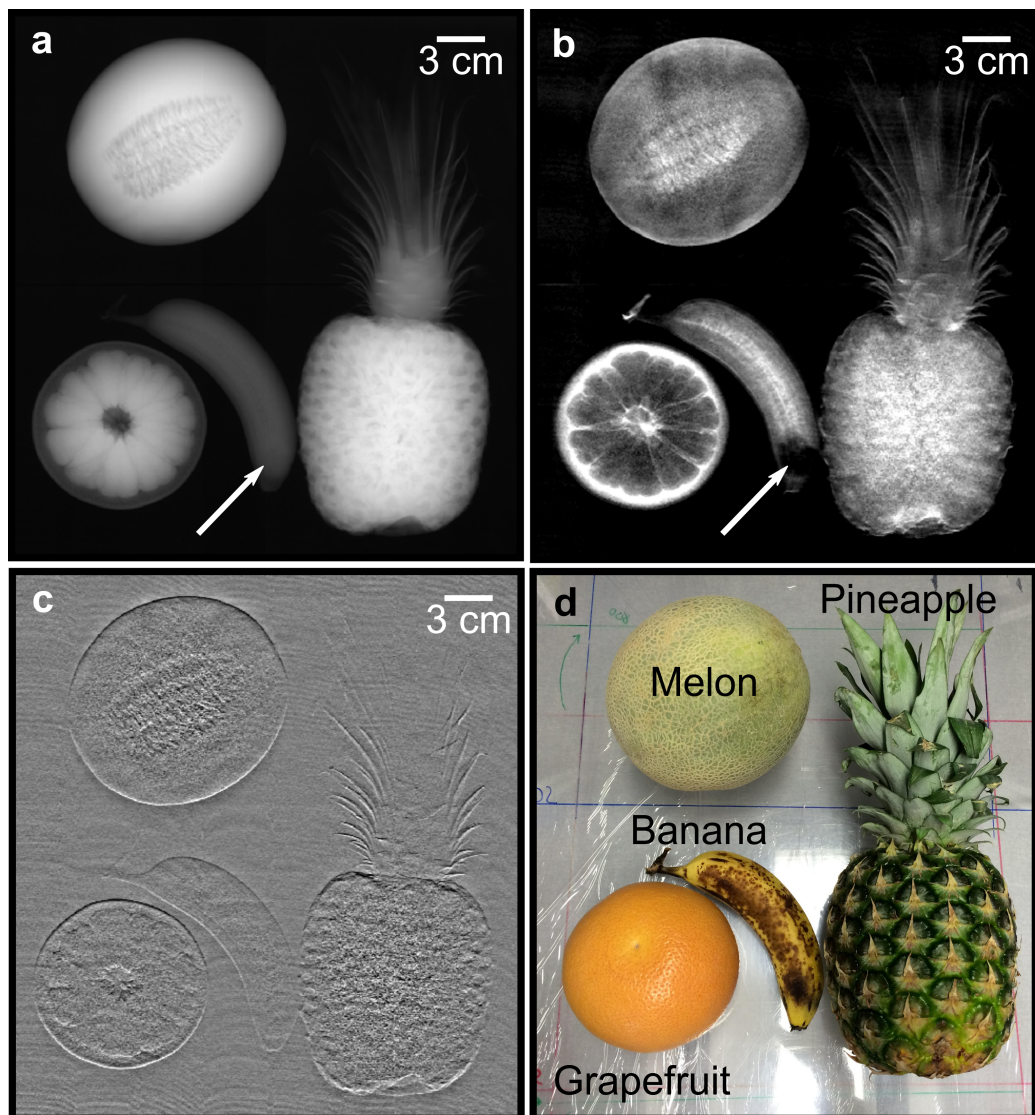


Figure 4.1 Full-field multi-contrast X-ray radiographs of a fruit arrangement. (a) Full-field X-ray attenuation, (b) XDF, (c) differential-phase radiographs, and (d) photograph of a fruit arrangement used as a test phantom to visualize the performance of the scanner across the entire FOV ($32 \times 35 \text{ cm}^2$). Note that the XDF channel provides complementary information not accessible from the conventional attenuation image: in the lower tip of the banana the fibrous cellular structure was destroyed by squeezing it prior to imaging, detectable in the XDF image as a loss in scattering signal (white arrow). The differential-phase mainly shows the edges of the fruit. Attenuation and XDF images are given on a logarithmic color scale. Please note, that this figure is also published as supplementary material in [68].

images[107, 108]. The energy-resolved visibility (also often called the “visibility spectrum”) can be considered the “fingerprint” of any XDF system. As the finally measured effective visibility is the integral over this visibility spectrum, weighted with the actual X-ray energy spectrum, it is very important to know this parameter as precisely as possible to be able to optimize the system.

4.2.2 Methods

4.2.2.1 Measurement of energy-resolved visibility

To measure the energy-resolved visibility, an X123 CdTe X-ray spectrometer (AMPTEK Inc., Bedford, USA) is used. This detector has an active layer of 1mm CdTe and is therefore well suited for the high X-ray energies (>40 kVp). To correct for the internal escape events of the CdTe, the XRS-FP Software, based on the results presented in [109], was used. By using a conventional phase stepping, the visibility for every energy bin can be calculated. However, the measurement can only be performed for a single pixel/position in the field-of-view. The sensor head was therefore positioned in the middle of the grating slot as indicated by the black arrow in Fig. 4.2.

4.2.2.2 Measurement of integrated visibility

In contrast, the effective visibility is measured with the energy-integrating Trixell flat panel detector (see section 3.4) for every pixel at once (as shown in Fig. 4.2b). This measured value is always dependent on the applied X-ray spectrum (tube voltage, pre-filtering and sample absorption).

4.2.3 Results & Discussion: integrated visibility

Fig. 4.2a shows a raw image of the detector with the Moiré fringe pattern adjusted for the fringe scanning procedure. With a conventional phase stepping, the effective visibility can be calculated. Fig. 4.2b visualizes such a visibility map, acquired at 70 kVp with seven phase steps. Due to the small gaps between the individual grating tiles, there are 14 lines with reduced visibility (seven gaps each in G1 and G2). The visibility of the individual grating tiles is slightly different due to inhomogeneities in the fabrication process (mostly due to differences in the gold height). Therefore, the gratings with the lowest visibilities were placed at the outer edges during the stitching procedure. The overall visibility is very high with $V = 31 \pm 4\%$ over the full slot at 70 kVp. This high visibility will allow for rather low radiation doses (see chapter 4.7 on page 95).

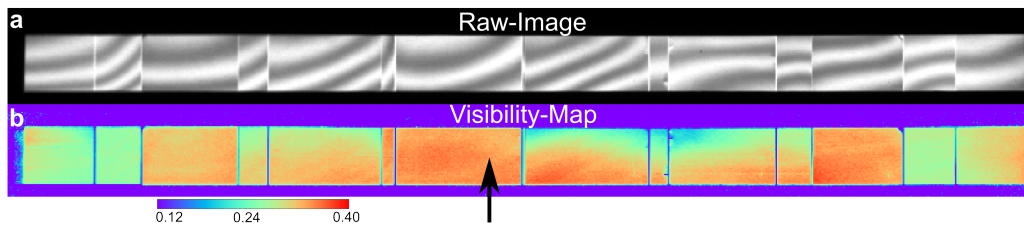


Figure 4.2 Images of the slot: (a) Raw detector image with Moiré-fringes and (b) visibility-map of the slot, acquired at 70 kVp with a conventional phase stepping approach, by moving $G0$ in 7 steps over one full grating period. As both $G1$ and $G2$ are tiled there are 14 small gaps with reduced visibility. Due to manufacturing differences in the gold heights, the visibility differs slightly over the different sub tiles, but is generally very high. The black arrow marks the position of the X123 CdTe spectrometer used for the energy-resolved measurements.

4.2.4 Results & Discussion: energy-resolved visibility

Fig. 4.3 shows the measured visibility spectrum (in the central grating tile of the slot, see black arrow in Fig. 4.2) and compares it to the simulation based on the parameters given in Table 4.2. As can be seen, there is an excellent agreement between the simulation and the measurement (consult chapter 2.5 for more details on the simulation method). The sharp increase in the visibility at around 80 keV is a result of the gold K-edge, leading to an increased attenuation efficiency for energies above this edge. However, this results in rather poor visibility values between 60-80 keV. A pre-filtering by adequate K-edge filters would help to reduce the photons in this “valley of no visibility”. Nevertheless, this will also drastically reduce the photon flux in all other energy bins. Further simulations showed that it is much more efficient to reduce the applied acceleration voltage of the X-ray tube to 60-70kVp, rather than using a much higher voltage (>80kVp) and additional K-edge filters to optimize the resulting signal-to-noise ratio. However, if much more electrical tube power would be available, K-edge filtering might become an option.

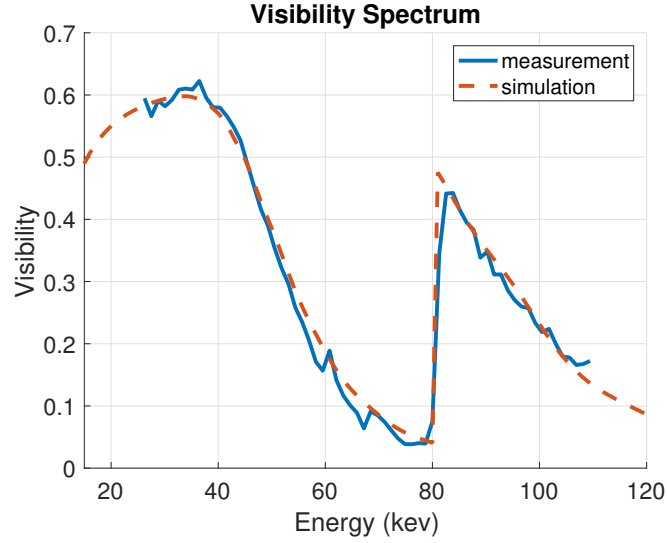


Figure 4.3 Energy-resolved visibility: The comparison between the simulation and the measurement shows a precise agreement. The sharp increase in the visibility above 80 keV is a result of the increased attenuation efficiency above the K-edge in the gold. However, the decreased attenuation efficiency below this edge results in rather poor visibility values between 60-80 keV.

	simulation	prototype
G0 period	68.72 μm	68.72 μm
G0 height	200 μm Au	240 \pm 20 μm Au
G0 duty cycle	0.7	0.7
G1 period	8.73 μm	8.73 μm
G1 height	170 μm Au	170 \pm 20 μm Au
G1 duty cycle	0.5	0.5 \pm 0.03
G2 period	10 μm	10 μm
G2 height	170 μm Au	>150 μm Au
G2 duty cycle	0.5	X
distance G0-G1	1571.4 mm	1570 \pm 3 mm
distance G1-G2	228.6 mm	230 \pm 3 mm
G1 ripple	0.1	X
σ_{smooth}	0.075	X

Table 4.2 Simulation parameters for the wave-optical simulations: The measured values for the gratings are averaged over the different grating tiles. Values marked with an X could not be measured.

4.3 Tube voltage optimization

4.3.1 Background & Motivation

For conventional X-ray imaging of the thorax, tube voltages between 60 and 120 kVp are usually used. This range is split into a lower kVp range around 70 kVp for imaging of the ribs and a higher voltages above 100 kVp for imaging of the lung parenchyma. This is done because lower tube voltages yield images with greater bone contrast which is undesired especially for diagnosis of (small) lung nodules[110]. However, recent studies reported an increase in signal-to-noise ratio and overall image quality at identical *effective dose* values for chest images acquired at lower kVp settings, both in phantom[111–114] as well as in clinical[113, 115] studies. This is mostly related to the increased soft-tissue contrast and increased detector efficiency at these energies.

For XDF no such guidelines are yet formulated. Therefore, in the following sections an optimization of the tube voltage for XDF lung imaging is performed with the developed prototype.

To find the optimal tube voltage for XDF imaging of highly attenuating samples like a thorax, different parameters have to be taken into account simultaneously. Most important are the effective visibility V , the XDF signal $\log(D)$ and the number of photons N that pass through the sample and are registered on the detector. With these three parameters a simplified equation for the resulting SNR can be formulated[107, 108]:

$$\text{SNR}_{\text{simple}}^{\text{XDF}} = \frac{\log(D)}{\sigma_{\log(D)}} \propto \log(D) \cdot V \cdot \sqrt{N}. \quad (4.1)$$

All three factors are dependent on the applied tube voltage. With lower X-ray energy the image noise in the XDF images will benefit from the higher visibility, however will suffer on the reduced transmittance of the sample and the therefore increased photon noise. Additionally, the XDF signal itself is also energy-dependent and will in most cases decrease for higher energies[56, 57, 65].

4.3.2 Methods

To analyze these effects in detail and to find the optimal operating point in terms of the X-ray spectrum, an experiment was performed. To mimic the attenuation of a realistic thorax, a slab of Polyoxymethylene (POM) with a height of 96 mm was placed on the sample table. To mimic the coherent scattering caused by the lung, epoxy plates with embedded micro-bubbles (sub-millimeter hollow glass spheres) were used. On top of the POM stack,

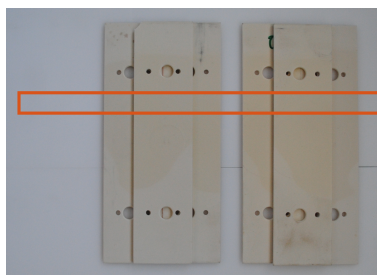


Figure 4.4 Test phantom: The photograph shows the two pyramids of the scatter-plates placed in top of 96 mm POM with the indicated ROI of the grating slot used for the evaluation.

scatter-plates were arranged in a staircase-like manner, resulting in areas with zero, one and two levels of scatter-plates. These should represent different thicknesses in the lung. Fig. 4.4 shows a photograph of the phantom and Fig. 4.5a shows the resulting XDF signal of the indicated region-of-interest (ROI). To measure the XDF signal, the visibility and the attenuation of the sample most accurately, a stepping scan with seven phase steps was performed. To exclude the effects of beam-hardening in this experiment, both the sample as well as the flat-field scan were performed with the POM in the beam.

Additionally, the tube power was chosen so that an adult human would receive an effective dose of 0.08 mSv at each of the kVp settings. This was calculated using a conversion procedure described in chapter 4.7. This is necessary to allow for a fair comparison between the different tube voltages values.

4.3.3 Results

As can be seen in Fig. 4.5b, there is an opposite trend for the visibility and the recorded detector counts (given in “LSB”) in the background region (behind 96 mm POM). There are almost 60 times more LSB counts for the 120 kVp scan, compared to the 40 kVp scan which is mostly due to the increased transmission of the POM, but also based on the energy-integrating feature of the detector. A 120 keV photon is weighted three times as much as a 40 keV photon. Nevertheless, if only these two parameters would define the SNR of the XDF signal, 60 kVp would be optimal as the visibility drops from almost 36 % for 40 kVp to about 11 % for 120 kVp. However, as the XDF signal itself is also energy-dependent (see 4.5c), this shifts the optimal SNR towards lower tube voltages as can be seen in Fig. 4.5d. For the strong signal

of the two stacked scatter-plates, the kVp optimum is not very narrow but in the same range as for the weak scattering single plate. The significant width of the maximum comes from the fact that the scattering of the object also reduces the visibility significantly and the simplified equation (Eq. 4.1) might not be sufficient to describe the SNR.

4.3.4 Discussion & Summary

For this test phantom the optimal kVp was found to be in the range of 50-70 kVp with a broad optimum. However, as the scatter-plates might not mimic the energy-dependent XDF signal of lung tissue very well, the optimum might be slightly different for real lung samples. In addition, the chosen thickness of 96 mm POM is only one example for a possible thorax thickness. For significantly thicker and thinner thoraxes the optimum might again be shifted. Additionally, there might be a strong gradient in the attenuation even within the thorax of an individual person/pig. Nevertheless, this experiment already gives a good starting point for an optimal kVp value. In section 5.2.3 on page 113, this experiment is repeated with a porcine thorax, as a more realistic case.

A further technical limitation for the tube voltage optimization is the available tube power. Usually the output power of X-ray tubes increases significantly for higher voltages. Especially for the currently installed MRC X-ray tube, it becomes impossible to apply even the very low dose of 80 μSv in a single slot-scan of the full FOV for voltages below 60 kVp. Therefore, in this experiment a conventional stepping approach was used which allows for much higher tube powers due to the limited FOV. Table 4.3 gives an overview over the maximum available tube powers and resulting dose levels for a standard slot-scan.

kVp	40	50	60	70	80	90	100	120
$I_{\max}[\text{mA}]$	420	560	700	800	890	950	990	800
$K_{\max}[\mu\text{Gy}]$	206	540	1055	1711	2593	3664	4874	5797
$ED_{\max}[\mu\text{Sv}]$	6	30	81	162	285	452	660	933

Table 4.3 Maximum tube power: Maximum tube current I_{\max} and achievable dose values in air kerma K at the sample position and converted equivalent dose ED using factors given in section 4.7 for a standard slot-scan of the full FOV with 20 ms exposure window per shot. Especially tube voltages below 60 kVp do not allow for tube powers necessary to achieve sufficient dose values for imaging of thick samples.

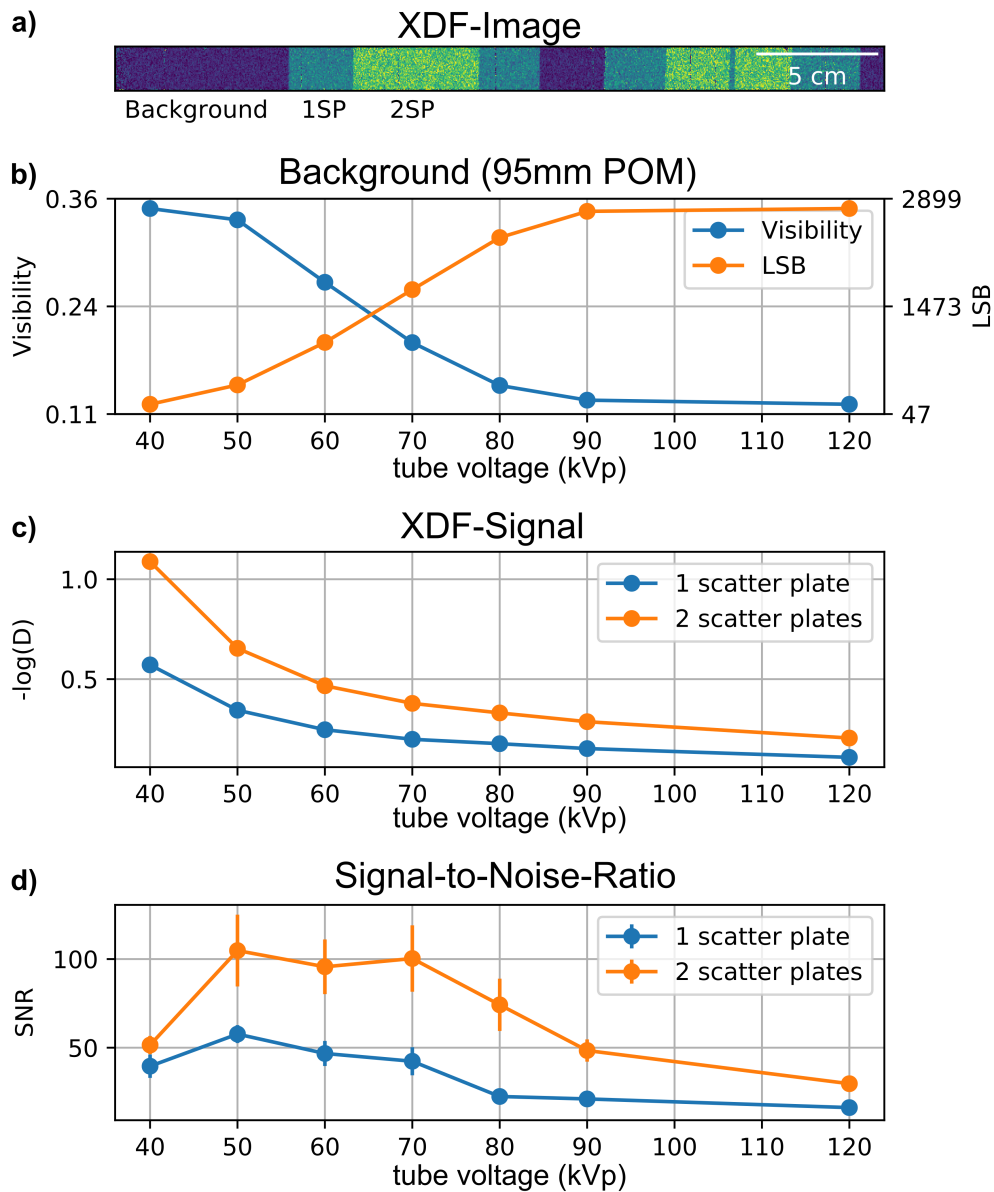


Figure 4.5 Tube voltage optimization with fixed dose: Two sets of scatter-plates (SP) were placed on a background of 96mm POM and scanned in the stepping mode with different kVp values but with a constant effective dose of $80\mu\text{Sv}$ for a corresponding PA exposure for a human thorax. Panel (a) shows the XDF image of the slot with the two scatter plate arrangements (zero, one and two plates stacked in a staircase-like manner). The resulting visibility of the background region (with the POM) is shown in (b) together with the raw detector counts (in LSB). Panel (c) shows the decreasing XDF signal for higher kVp and (d) gives the resulting signal-to-noise ratios (SNRs) of the XDF signals. The error bars in (d) represent the uncertainty to the SNR value with respect to the different ROIs for the two sets of scatter-plates.

4.4 Visibility reduction by Compton-scattering

4.4.1 Background & Motivation

Compton-scattering is one of the main mechanisms (besides the photoelectric effect) which is responsible for the attenuation of X-rays in matter at clinically relevant energies. However, Compton-scattered photons are generally not absorbed in a sample but just redistributed in all directions with slightly reduced energy. As most of these scattered photons will not reach the detector anymore, it is reasonable to account Compton-scattering as a significant contribution to the measured attenuation. However, in every realistic imaging experiment there will be a certain amount of Compton-scattered photons still reaching the detector, although they will most likely be recorded in a different pixel than the non-scattered photons with the same initial trajectory. As these scattered photons contain little to no imaging information, they are often referred to as the “Compton background” in the image. The detector signal I can therefore be written as

$$I = a_0 + a_C \quad (4.2)$$

with a_0 standing for all photons reaching the detector directly and a_C standing for all photons that are Compton-scattered at least once before reaching the detector. The ratio between these two is defined as the scatter-fraction

$$\text{SF} = \frac{a_C}{a_0}. \quad (4.3)$$

As the measured visibility V_{meas} is defined as the ratio between the measured oscillation amplitude a_1 divided by the mean intensity I_0 , it is heavily affected by these additional Compton events which result in an offset of the stepping curve:

$$V_{\text{meas}} = \frac{a_1}{a_0 + a_C} \quad (4.4)$$

$$= \frac{a_1}{a_0} \cdot \frac{1}{1 + \frac{a_C}{a_0}} \quad (4.5)$$

$$= V_0 \cdot \frac{1}{1 + \frac{a_C}{a_0}} \quad (4.6)$$

$$= V_0 \cdot D_{\text{CS}}. \quad (4.7)$$

D_{CS} becomes significant for high values of the scatter-fraction, e.g. for small

values of a_0 behind highly attenuating samples which additionally produce a lot of Compton-scatter.

In order to reduce this pseudo dark-field signal D_{CS} , different approaches (and their combinations) are possible:

1. Reducing the X-ray energy will reduce the amount of Compton-scatter, as the photoelectric effect is the dominant effect for lower X-ray energies.
2. Reducing the sample thickness would also reduce the amount of scattering and would additionally increase a_0 as the sample would become more transparent.
3. Using a slot-scanning approach, rather than a full-field approach will drastically reduce the amount of recorded scatter.
4. Estimating the amount of scattered photons either from simulations or from dedicated measurements would allow to correct for them.

As points 1 and 2 are impractical approaches for a targeted chest X-ray system, approaches 3 and 4 are evaluated in the following sections. Here especially the Compton-scattering reducing effects of G1 as an attenuation grating behind the sample as well as the effects of the slot-scanning geometry are analyzed.

4.4.2 Methods

4.4.2.1 Monte-Carlo simulation framework

To be able to estimate the amount of Compton-scattering in different geometries, a simulation based on Geant4/Gate[89] was implemented. The simulation includes the X-ray source, the detector, the X-ray gratings G1 and G2, the sample table and different voxelized phantoms. An image of the simulation geometry is shown in Fig. 4.6. Either the ICRP-AF phantom[116] or a pig phantom created from a CT scan of one of the pigs used in chapter 5.1 on page 107 can be imported in the simulation.

The X-ray gratings are explicitly modeled as ensembles of parallel gold lamellas from a given grating period, duty cycle and absorber height. This approach is computationally intensive but the most accurate one. The gratings can either be implemented as bent, full-field gratings or in a moving slot, to account for the slot-scanning approach. To achieve a robust photon statistic in the simulation, usually about 10^{10} photons are started from the source point towards the detector, resulting in a computation time of a few days even

on powerful compute servers. To reduce computation time, the $43 \times 43\text{cm}^2$ detector is divided into only 120×120 pixel which is justified as the Compton signal does not contain any high frequency features. For reference a flat-field is simulated with the same geometry, except for the sample/phantom, similar as in a real experiment.

To further save computation time, the photons are only tracked up to the surface of the detector. Internal conversion in the scintillator of the X-ray photons to visible light and an electric read out signal is not simulated. Instead, the conversion efficiency of the detector layer is included in the effective X-ray spectrum. Nevertheless, the energy-integrating property of the detector is taken into account in the MC simulation.

4.4.2.2 Different geometries

In this chapter, different system configurations for a hypothetical XDF-scanner are evaluated for their performance regarding Compton-scattering suppression. Four cases are of special interest:

1. The “reference” system is the developed XDF slot-scanning prototype with two attenuation gratings (G1 & G2) behind the sample.
2. A similar slot-scanning system as the prototype, however with G1 not affecting the Compton-scattering (e.g. G1 designed as a phase grating or placed before the sample).
3. A slot-scanning device with no gratings at all.
4. A full-field approach with both G1 and G2 as attenuation gratings as a benchmark to identify the Compton-scattering suppression efficiency of the slot itself.

All simulations were performed with a pre-filtered 70 kVp tungsten spectrum in the geometry of the developed XDF-scanner as listed in Table 4.2 on page 66. The detailed MC simulation parameters for these four configurations are listed in Table 4.4.

4.4.3 Results

Case #1 provides the best performance regarding Compton-scattering suppression, while the other three are less effective as can be seen in the resulting Compton-scattering signal of the ICRP-AF phantom in Fig. 4.7. The removal of the G1 attenuation grating (e.g. G1 realized as a non-absorbing

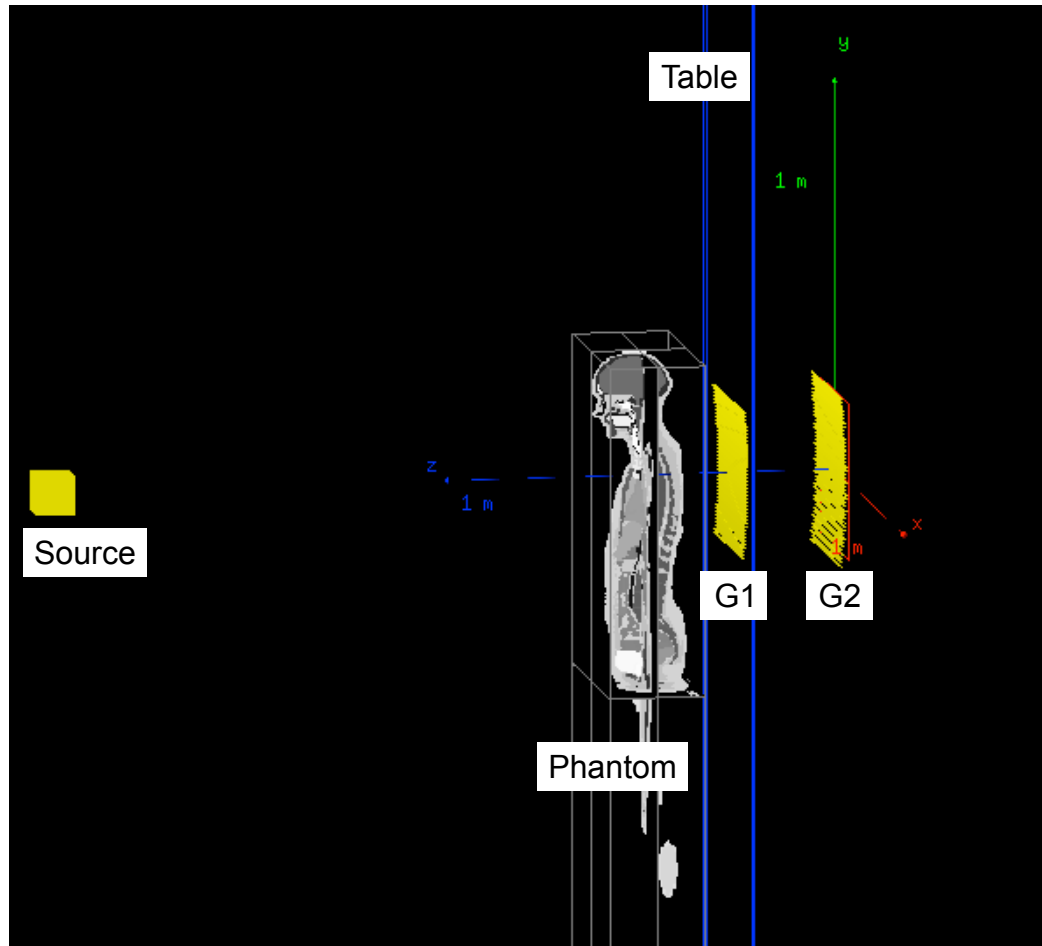


Figure 4.6 Geometry of the Monte-Carlo simulation: The ICRP-AF phantom is placed on top of the table. The X-ray gratings are shown here as bent full-field gratings but can also be simulated in a moving slot-scan geometry, depending on the simulation task. The collimators are not visualized here.

mode	G1	G2	phantom	slot collimator	side collimator	spectrum
slot-scanning #1	yes	yes	ICRP-AF	yes	no	70 kVp
slot-scanning #2	no	yes	ICRP-AF	yes	no	70 kVp
slot-scanning #3	no	no	ICRP-AF	yes	no	70 kVp
full-field	yes	yes	ICRP-AF	no	no	70 kVp

Table 4.4 Monte-Carlo simulation parameters: Parameters for the four different configurations. The side collimators are not used here, as the thorax of the human phantom was wide enough to cover the full FOV (in contrast to the pigs). If the slot collimator is used, it is moved across the FOV, similar to the real experiments.

phase grating, Fig. 4.7b) does not have a significant influence on the scattering ($a_{C, \text{withG1}} = a_{C, \text{noG1}} = 0.9\%$ intensity of the flat-field, for the red ROI indicated in Fig. 4.7a).

This can be explained by the similar acceptance angles of the two absorption gratings with $170 \mu\text{m}$ gold height and an opening of $x = p/2$:

$$\alpha_{G1} = \arctan\left(\frac{p_1}{h_1}\right) \approx 1.5^\circ \quad (4.8)$$

and

$$\alpha_{G2} = \arctan\left(\frac{p_2}{h_2}\right) \approx 1.7^\circ. \quad (4.9)$$

This means, that almost every scattered photon that would be blocked by G1 on the first hand would also be blocked by G2, if G1 is not there¹.

Please note: Photons that are scattered less than 1.5° (and which are therefore not blocked by G1) still might result in a reduction of the visibility due to the large distance between the G1 grating and the detector: after a propagation of 23 cm , this angle still allows for a lateral shift of about $600 \mu\text{m}$, which is equivalent to 60 periods of the G2.

For future applications, where the attenuating G1 grating is replaced by a non-absorbing phase-grating for dose efficiency, this is an encouraging result. If both gratings are removed (Fig. 4.7c), the overall scattering is more than doubled ($a_{C, \text{noGratings}} \approx 1.9\%$), and most interestingly, any sample features get completely blurred out. This happens because of the rather asymmetric scattering reduction by the gratings. If the system is changed from a

¹This requires G1 & G2 to provide significant stopping power to all relevant photons.

slot-scanning approach to a full-field approach (Fig. 4.7d), the scattering background is increased to about $a_{C, full-field} = 2.4\%$ of the flat-field intensity.

Fig. 4.8 shows the resulting scatter-fractions SF for these configurations. As the Compton background is a rather low frequency and smooth image (compare Fig. 4.7), the scatter-fraction is high at regions with rather low transmission values. Even for case #1, which has the best scattering reduction properties, there is still up to 50% scatter-fraction behind thick bones and a SF of about 14% behind the lung (red ROI in Fig. 4.8a). Behind the relatively transparent lungs, this effect converts to about 10% of pseudo dark-field signal (see Fig. 4.9). Additionally, this value would even increase for increased body fat before or behind the lung. For the two extreme cases, i.e. without additional gratings (Fig. 4.7c) or without the slot-scanning (Fig. 4.7d), there is above 50% SF for most parts of the thorax and about 25% pseudo dark-field signal D_{CS} behind the lungs (compare Fig. 4.7 and 4.9).

4.4.4 Summary & Outlook

In this chapter, it was shown that Compton-scattering has a significant influence on the measured dark-field signal. For the developed prototype, the pseudo XDF signal in the human lung is expected to be in the range of about 10%. Further it was shown that the G1 grating has only a minor influence on the Compton-scattering reduction, if realized as an attenuation grating which is encouraging for future systems with a phase grating for G1. For full-field gratings this problem becomes severe with up to 25% of pseudo XDF signal D_{CS} behind the lung in the analyzed geometry. However, these results are so far only based on a single human phantom. For much thinner or thicker samples these results might change. Therefore, a larger simulation with different patient sizes (e.g. with the XCAT phantoms[117]) should be performed in future, to get a better understanding of the influence of inter-patient size on the additional pseudo signal.

As shown, the remaining Compton-scattering is still significant and may affect the outcome of an XDF based diagnosis in future clinical applications. Therefore, a method to correct this via a Monte-Carlo simulation is presented in the next chapter.

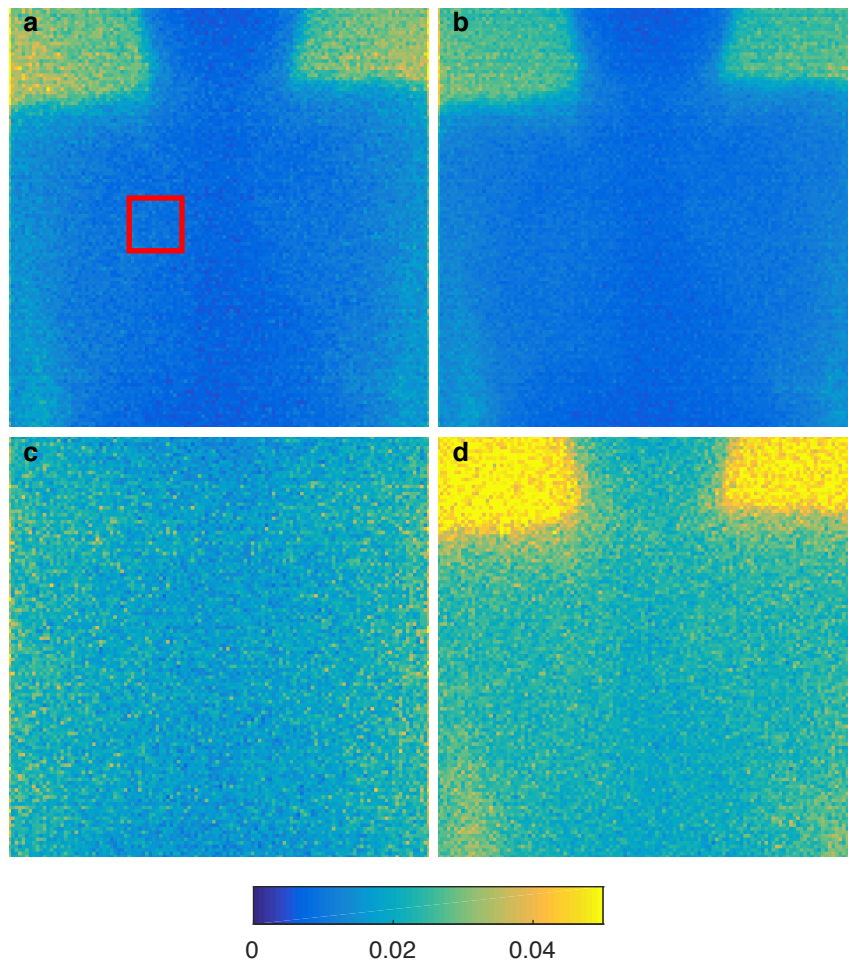


Figure 4.7 Simulated scattering signal a_C for ICRP adult female phantom: (a) Slot-scanning geometry (#1) of the developed scanner with $G1$ and $G2$ realized as attenuation gratings. (b) Slot-scanning geometry (#2) with only $G2$ as an attenuation grating. (c) Slot-scanning geometry (#3) without gratings. (d) Full-field geometry with both $G1$ and $G2$ as attenuation gratings. The signal is given as a fraction of the total intensity in the flat-field to allow for an easy comparison between the different configurations. The red rectangle in panel (a) defines the ROI for the quantitative analysis in all images.

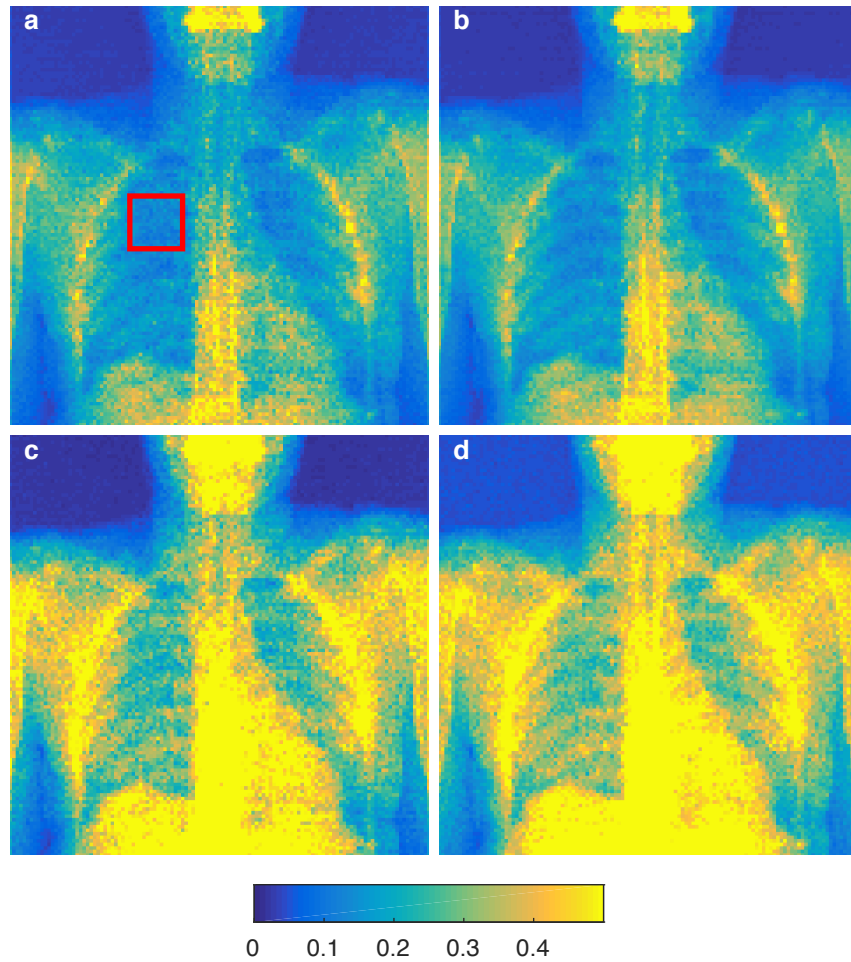


Figure 4.8 Simulated scatter-fraction: Subfigures (a)-(d) are defined equal to Fig. 4.7(a)-(d). The scatter-fraction is given as the ratio between the scattered and un-scattered photons. A value of 1 would mean that there are as many scattered photons as un-scattered photons registered in this pixel. Behind thick bones, the SF is up to 50% even for the best case with two attenuation gratings and a slot-scanning approach (see panel (a)). For the full-field approach (d), the scatter-fraction exceeds the 50% in most areas of the thorax. The resulting pseudo dark-field caused by this scattering is shown in Fig. 4.9.

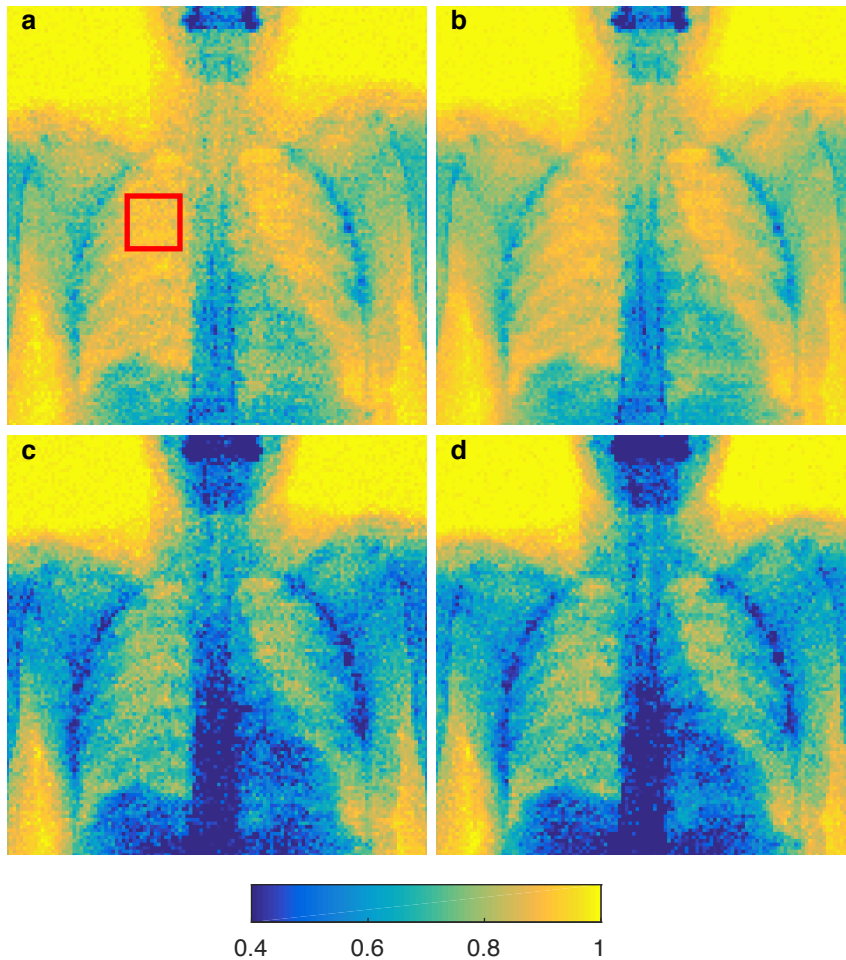


Figure 4.9 *Simulated pseudo dark-field D_{CS}* : Subfigures (a)-(d) are defined equal to Fig. 4.7(a)-(d). D_{CS} is calculated by Eq. (4.4) from the scatter-fraction shown in Fig. 4.8 and is given with a linear colormap. A value of 1 therefore stands for “no signal”, while a value smaller than one indicates a loss in visibility and therefore a D_{CS} signal. In case (a), the pseudo signal behind the lung (red ROI) is not too high, but still sums up to a visibility loss of around 10%. For the worst case of no gratings (c), or no slot (d), this pseudo signal might increase up to 25%.

4.5 Compton-scatter-correction for sample data

4.5.1 Motivation

In order to make a diagnostic decision based on the XDF signal of the (human) lung, the additional pseudo signal D_{CS} should be corrected as much as possible. Otherwise, e.g. differences in body weight would result in very different dark-field signals of the lung. Additionally, the contrast of the dark-field active lung and the non dark-field active parts of the thorax can be drastically reduced by the pseudo signal behind the heavily attenuating body parts, up to the point where heavily attenuating parts would show as much or even more XDF signal than the lung itself.

However, to be able to correct the measured signal D_{meas} for the Compton-scattering via

$$D_{\text{noCS}} = \frac{D_{\text{meas}}}{D_{CS}}, \quad (4.10)$$

the value of D_{CS} needs to be known precisely. In general there are three possible approaches on how to estimate this:

1. Monte-Carlo simulations of the Compton-scattering for every individual sample.
2. Estimation of the samples' Compton signal by fitting the sample image to pre-calculated generic MC data.
3. Direct measurement of the Compton signal.

4.5.2 Methods

In this chapter, the first approach from the list above is evaluated in more detail, as for at least some of the samples acquired at the XDF scanner also conventional CT data is available. With the CT data, an individual 3D phantom can be designed for the corresponding sample. This is done by a material decomposition based on the quantitative Hounsfield-units (HU)[118] of the CT data. A rendering of this phantom is shown in Fig. 4.10. For this phantom, a full MC simulation is then performed with the parameters of the XDF-scanner (gratings, distances, geometry etc. as listed in Table 4.2 and Table 4.5). With the obtained a_0 and a_C images (see Fig. 4.11c and d), the resulting pseudo signal D_{CS} (see Fig. 4.11e) can be calculated according

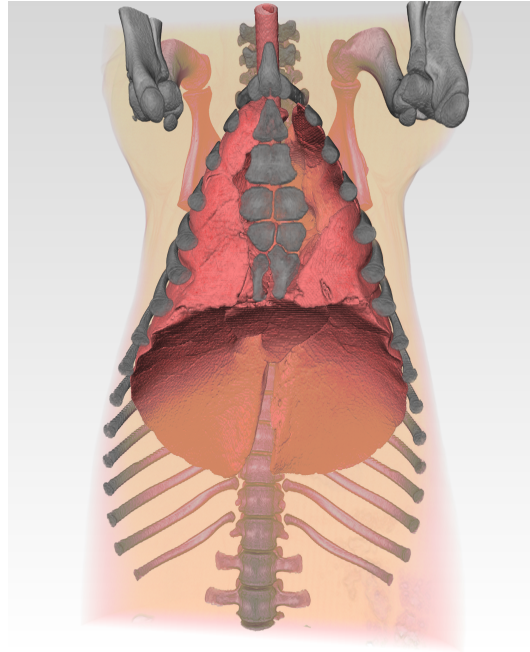


Figure 4.10 Rendering of the pig phantom: Visualization of the segmented pig phantom with the Amira-Avizo 3D Software (FEI, Hillsboro, Oregon, USA). The segmented lung and bones are shown here on a transparent background of soft-tissue.

to equation (4.4). Finally, a *scatter-corrected* XDF image (Fig. 4.11f) is obtained by using Eq. (4.10).

4.5.3 Results & Discussion

Fig. 4.11 visualizes this approach for one example dataset of one of the pigs (compare section 5.1). The pseudo XDF signal behind the lung is not very dominant in this case ($D_{CS} < 5\%$), especially compared to the findings of the human phantom in the previous chapter. This is mostly due to the additional

mode	G1	G2	phantom	slot collimator	side collimator	spectrum
slot-scanning #1	yes	yes	pig	yes	yes	70 kVp

Table 4.5 MC simulation parameters for the numerical pig phantom.

lead shielding at the sides of the animal which reduce the scattering along the “sensitive” axis (grating lines are parallel to the slot which is scanned from bottom to top in this case).

A major issue with this approach is the geometric correlation of the CT-data with the acquired XDF-projections. In the example shown in Fig. 4.11, this was achieved by manual alignment of the 3D phantom (rotation and translation), followed by an image registration process performed with the “imregister” function of MATLAB (2016b, The MathWorks, Natick, USA). However, both of these corrections can only correct for geometric distortions up to a certain level. Physiological changes in the two scans, like differences in respiration depths, cannot be corrected at all.

The more generic simulation approach (#2 in the list above) would therefore be much better. Instead of doing the MC simulation for every individual sample, it would be beneficial to precompute the Compton-scattering contributions of various different samples (e.g. water spheres of different sizes) and then fit the measured sample to this database. However, this is not easy to implement and would exceed the scope of this thesis. An implementation of such an approach for conventional radiography can be found in commercially available products (e.g. the Philips Skyflow software[119–122]). Such a software package could be extended to also include the X-ray gratings, necessary for XDF-scanners.

4.5.4 Summary & Outlook

As the Compton-scattering can have a significant influence on the measured dark-field signal, this might affect the outcome of an XDF based diagnosis in future clinical applications. To prevent this, a method was developed to correct for this pseudo signal via a Monte-Carlo simulation. For the developed scanner, the pseudo XDF signal in the lung is only about 5 % for porcine thoraces compared to about 10 % for human ones. This is based on the reduced FOV (and therefore reduced Compton-scatter) due to the narrower thorax. The main uncertainty in this correction method comes from the alignment of the two datasets. An improvement in the alignment could be achieved, if D_{CS} is not calculated from both the simulated *no-scattering* and *scattering* images but rather from the measured transmission image and only the simulated scattering image:

$$D'_{CS} = \frac{1}{1 + \frac{a_C}{T_{meas}}}. \quad (4.11)$$

This is beneficial, as the *scattering* image does not contain any high frequency features like edges or anatomical details. Therefore a small error in the

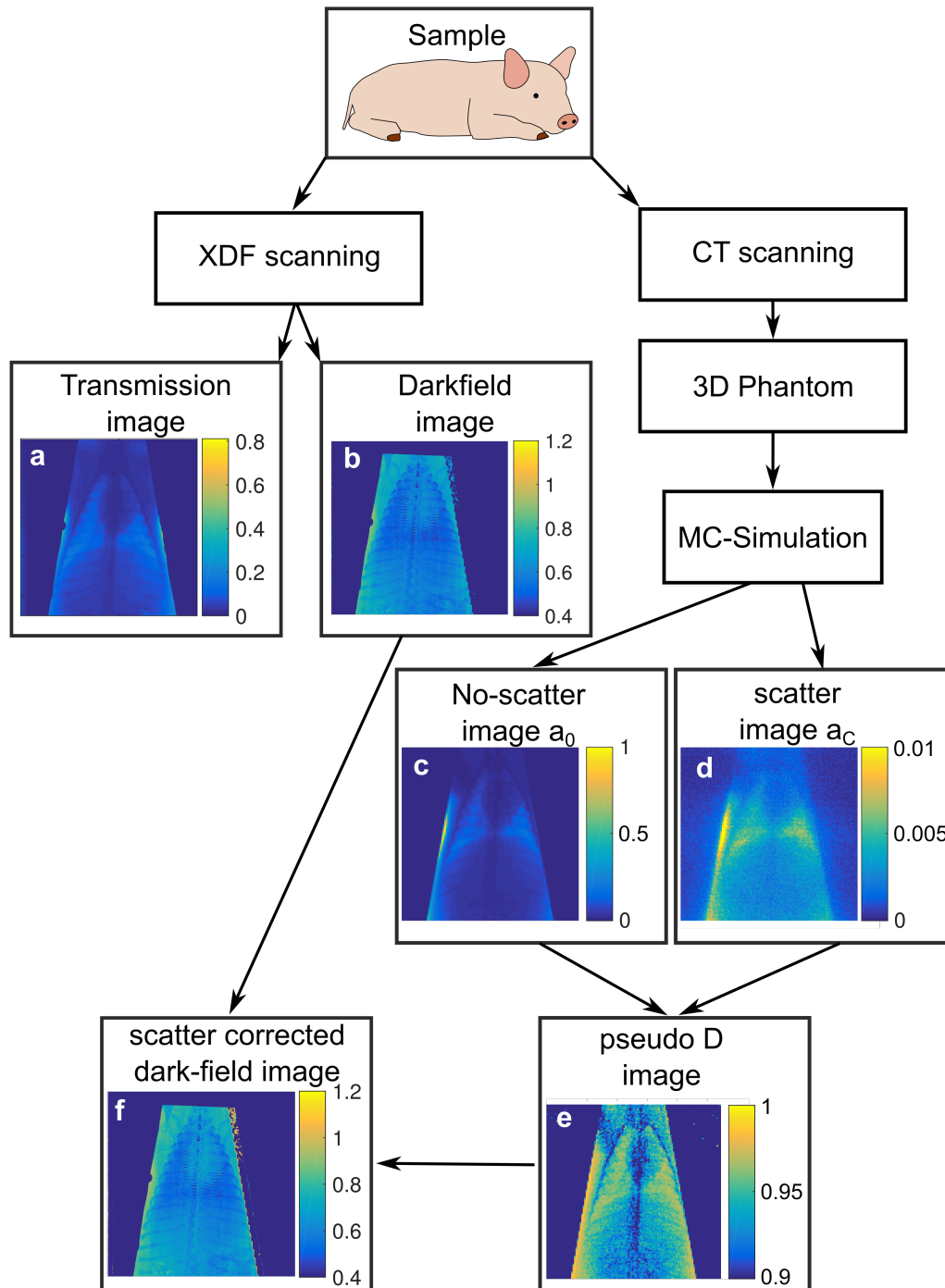


Figure 4.11 Flowchart of the CS correction pipeline: The sample is scanned in the XDF-scanner and in a CT-Scanner. From the CT data, a 3D phantom is designed for the MC-simulation. From this simulation a pseudo XDF image can be calculated and the acquired dark-field image can then be corrected with the simulation. The alignment of the two datasets is a rather large source of uncertainties.

registration of the simulated scattering image will not result in a strong error in D'_{CS} , as all the anatomical information (especially the position of the bones) comes from the measured transmission T_{meas} . This approach should be tested in future research.

A completely different approach would be a direct measurement of the Compton-scattering contribution. So far, this is only a theoretical consideration but with a slot-scanning device, it should in principle be possible to calculate the amount of Compton-scattering from the signal measured behind the edges of the slot collimators as sketched in Fig. 4.12. In the most simplified assumption, all counts behind the slot blades can be considered as Compton background and their mean could simply be subtracted from the individual slot image. But also more complex interpolation schemes are conceivable. A implementation of this method should be part of follow-up research.

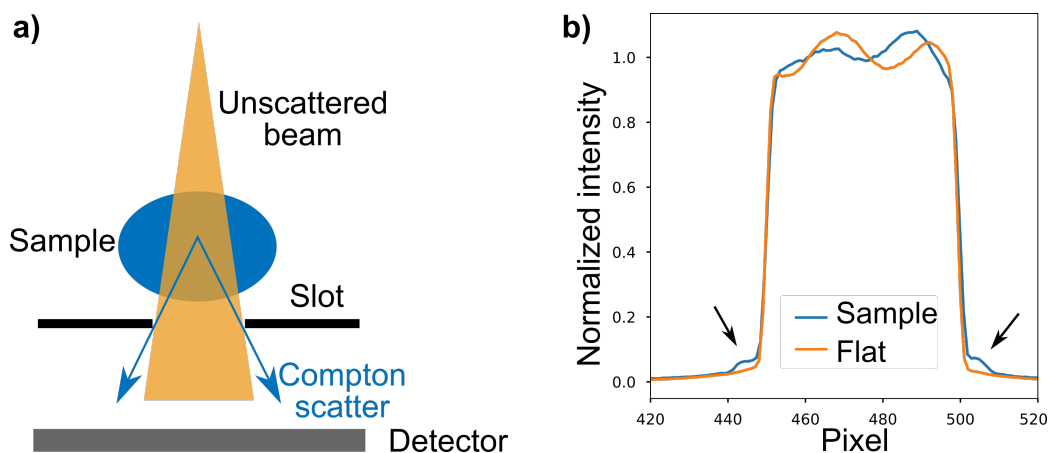


Figure 4.12 *Direct measurement of the Compton background:* (a) Schematic of the basic idea for the measurement of the Compton background. Compared to the flat-field scan, there should be some additional detector intensity behind the slot collimator blades, which are proportional to the overall scattering intensity of this sample. (b) The line-profiles of a measured example slot-image of 10 cm of POM reveals the additional Compton counts compared to the flat-field behind the lead blades (black arrows). Both curves are normalized to their mean intensity.

4.6 Beam/visibility-hardening effects

4.6.1 Background & Motivation

As the visibility of the developed scanner is energy-dependent (as shown in Fig. 4.3) the measured visibility will be dependent on the effective X-ray spectrum reaching the detector. This effect is often called *beam-hardening* but is more precisely *visibility-hardening*[123–125]. The main problem is the change in the X-ray spectrum by heavily attenuating samples, compared to the unfiltered spectrum in the reference scan. This will result in artifacts in the measured XDF images, as the reference visibility is no longer valid.

In the following sections, a correction method for these artifacts is introduced, followed by a discussion of suitable calibration materials. Finally, the experimental acquisition procedure is discussed in detail and the difficulties in the actual calibration measurements are discussed.

4.6.2 Calibration & Correction method

To account for the visibility change between the flat-field and actual sample scan, a calibration is performed with different thicknesses of an equivalent absorber[124, 125]. For all thicknesses of the absorber, both the transmission T as well as the visibility-hardening $D_{\text{VH}}(T)$ are measured with a conventional phase-stepping measurement. To correct the measured XDF signal D_{sample} for a certain pixel in a sample scan, this value is corrected with the calibration data $D_{\text{VH}}(T)$ at the same transmission value T_{sample} as the sample value:

$$D_{\text{VH,corrected}}(D_{\text{sample}}, T_{\text{sample}}) = \frac{D_{\text{sample}}}{D_{\text{VH}}(T_{\text{sample}})}. \quad (4.12)$$

As only a finite number of calibration points can be acquired, an interpolation step is necessary to account for the continuous range of transmission values present in a sample. Empirically it was found (compare Fig. 4.13) that the visibility-hardening in the calibration data can be fitted very well by a model function

$$D_{\text{VH}}(T) = a \cdot T^b + c, \quad (4.13)$$

with three fitting parameters a , b and c . This method requires therefore at least three measurement points. However, in practice, as many calibration points as possible should be used to reduce the effect of noise. Please note that the model function in Eq. (4.13) is basically a result of the applied X-ray spectrum and the visibility spectrum of the scanner. For a completely different set of gratings (and therefore a different visibility spectrum), maybe another model function might fit the data better. However, for the developed

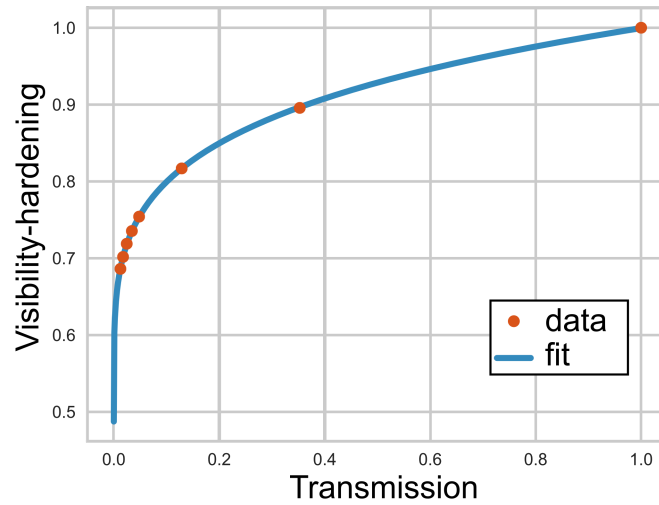


Figure 4.13 Visibility-hardening curve: The figure shows the fitting of one measured example visibility-hardening curve (POM, 60 kVp) with the model from Eq. (4.13). The fit quality is very good.

prototype the introduced model was found to fit well to calibrations with tube voltages between 50 and 120 kVp.

4.6.3 Choice of calibration material

In principle, the calibration material should be identical to the imaged sample. As this is impossible for biological samples, a substitution material has to be found which mimics the sample as well as possible in terms of its interaction with X-rays. However, in contrast to mammography, where the human breast can be modeled by a single soft-tissue equivalent absorber[98], this is not possible for thorax imaging. In the thorax, there are at least two fundamental different materials present: soft-tissue (e.g. fat, muscles and the inner organs) and bones (e.g. ribcage, backbone and the shoulder blades).

A correction method only for soft-tissue will result in remaining artifacts for bones and vice versa. To analyze which material suits best as a calibration material for a thorax image, a simulation was performed. The 3D phantom of the pig (see chapter 4.5) was used to simulate the amount of visibility-hardening VH with the wave-optical simulation (results are shown in Fig. 4.14a). In addition, the visibility-hardening calibration curves (as they would have been measured in a real calibration measurement) were simulated for four different materials and were used to correct the simulated

VH-XDF signal of the pig.

Fig. 4.14c-f shows the virtually corrected XDF images for the four different calibration materials. As expected, a correction with “soft-tissue(ICRU-44)” leads to the best results for all areas of the thorax except for the bones. If corrected by a soft-tissue-equivalent absorber, bones will always be under-corrected and will stay therefore in the image with a remaining VH-XDF signal. A correction with pure adipose tissue (ICRU-44) will result in an overall under-correction of the visibility-hardening. As a calibration with real soft-tissue material is not possible, POM (polyoxymethylene) and water were also simulated as equivalent absorbers. As can be seen in Fig. 4.14c and d, water would be a slightly better substitution for soft-tissue than POM. However, POM was chosen for the following experiments, as a solid calibration material is much easier to handle. Further, the calibration can only be an estimation of the visibility-hardening signal. The actual sample composition will (in contrast to the case here in the simulations) never be known exactly which results in uncertainties as there is quite a difference between adipose and soft-tissue. Therefore, POM is considered to be a suitable calibration material for soft-tissue measured in the developed prototype. For other systems and/or other energy ranges, this might again be different. The correction of the remaining bone artifacts is discussed in detail in section 4.6.5 on page 89.

4.6.4 Calibration measurements

4.6.4.1 Compton-scattering content

The experimental measurement of the pure visibility-hardening curves of any equivalent absorber poses substantial challenges for different reasons. The main issue is the measurement of additional pseudo XDF signal by inherent Compton-scattering, especially for thick calibration materials. To analyze this effect, Fig. 4.15 compares different sets of measurements. One set of measurements was performed with the POM slabs placed at the same position as the actual sample would have been (on the table). Here, a lot of Compton-scattered photons will reach the detector, resulting in a high amount of additional pseudo XDF signal, besides the visibility-hardening signal. For the other set of measurements, the POM slabs were placed close (30-40 cm) to the focal spot of the X-ray source. This set of measurements is expected to contain almost no Compton signal. As can be seen in Fig. 4.15, there is a major difference in the curves for “source” and “table” which is exactly due to the mentioned influence of Compton-scattering.

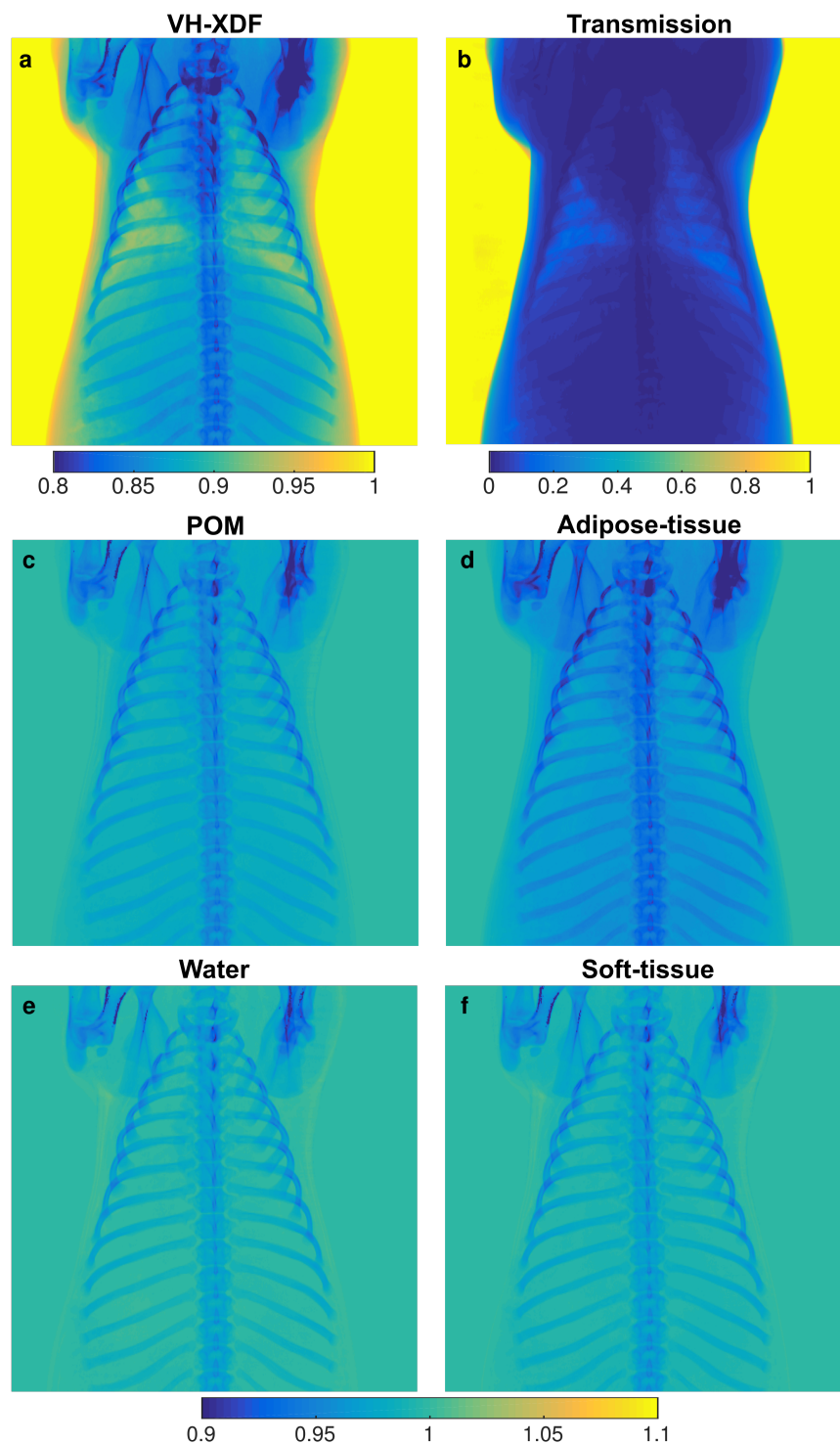


Figure 4.14 *Simulation of visibility-hardening corrections with different calibration materials:* Simulation of (a) VH-XDF signal caused by the visibility-hardening for the pig phantom and (b) corresponding transmission image for a 70 kVp tungsten spectrum (all other simulation parameter are listed in Table 4.2). Panel (c)-(f) show the virtually corrected XDF images of the pig for corrections with POM (c), adipose-tissue (d), water (e) and soft-tissue (f).

Strip Frequency N	Grid Ratio r	Focus distance f_0
36 l/cm	12	180 cm

Table 4.6 Parameters of the anti-scatter-grid.

4.6.4.2 Effects of additional anti-scatter-grids

To further study the effects of Compton-scattering, an additional anti-scatter-grid (parameters listed in Table 4.6) was placed on top of the detector with its lines orthogonal to the gold gratings. As can be seen in Fig. 4.15, there is almost no effect for the measurements with the POM slabs close to the source, as there is already almost no Compton-scattering in this data. For the measurement of the POM slabs on the table, there is a small reduction in the Compton-scattering content by the additional ASG, however it is not very effective, compared to the measurement with the POM slabs close to the source.

The calibration should therefore be performed with the equivalent absorber close to the X-ray source and the Compton-scattering should be corrected separately as discussed in section 4.5. A completely different approach would be a calibration with the POM slabs on the table with the assumption that the sample to be calibrated (e.g. a human or porcine thorax) will create a similar amount of Compton-scattering and that therefore a single calibration is sufficient to correct for both effects. However, this would require rather strong assumptions and simplifications about the sample which will easily result in under or over correction.

4.6.5 Correction of bone artifacts

Please note: For the methods explained in the following section, a patent application is pending.

4.6.5.1 Motivation

After the correction of a thorax solely with POM, there will remain some bone artifacts, as visible in Fig. 4.14c. These artifacts result from the under-correction of dense bone tissue with POM. In the following section, a two fold correction approach is proposed which addresses this issue. The basic idea here is to segment the measured sample into its two main components, namely soft-tissue and bones:

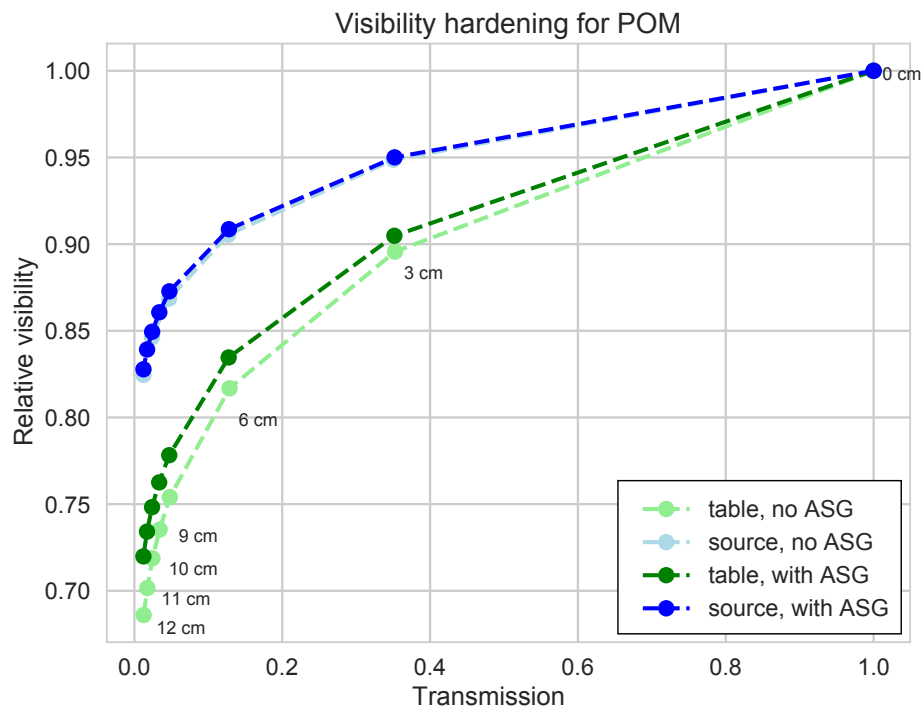


Figure 4.15 Compton content in VH correction curves: The figure shows the measured VH curves for POM in different configurations. One dataset was acquired with the POM slabs placed on the table and for the other, the POM slabs were placed close to the X-ray source. Both measurements were also repeated with an additional anti-scatter-grid (ASG) placed on the detector, whose parameters are listed in Table 4.6. The lamellas of the ASG were orthogonal to those of other gratings.

$$T_{\text{total}} = T_{\text{softTissue}} \cdot T_{\text{bones}} \quad (4.14)$$

which simplifies for the logarithmic transmission signal T' to

$$T'_{\text{total}} = T'_{\text{softTissue}} + T'_{\text{bones}}. \quad (4.15)$$

$T_{\text{softTissue}}$ and T_{bones} represent here the individual contribution to the attenuation signal caused by each material. These two material maps should ideally be proportional to the (projected) thickness of their corresponding materials. With this segmentation, the visibility-hardening correction is then separated in a calibration step for the soft-tissue by POM and a calibration step only for bones by e.g. aluminum²:

$$D_{\text{corr}} = \frac{D_{\text{measured}}}{D_{\text{VH}}^{\text{POM}}(T_{\text{softTissue}}) \cdot D_{\text{VH}}^{\text{alu}}(T_{\text{bones}})}, \quad (4.16)$$

or for the logarithmic images

$$\bar{D}_{\text{corr}} = \bar{D}_{\text{measured}} - \bar{D}_{\text{VH}}^{\text{POM}}(\bar{T}_{\text{softTissue}}) - \bar{D}_{\text{VH}}^{\text{alu}}(\bar{T}_{\text{bones}}). \quad (4.17)$$

However, such a segmentation is not easy to create, especially in the case of projection imaging. Three different approaches are suggested in the following which can provide such a segmentation into the two material maps “bone” and “soft-tissue”:

4.6.5.2 CT data

The first approach is only suitable for samples, where quantitative CT data is available. Based on the 3D volume, a segmentation of the bones is easily possible, either by simple thresholding of the HU values or by more sophisticated segmentation algorithms. With this segmentation, an individual visibility-hardening correction can then be performed for both bones and soft-tissue on the forward projected 2D images in the geometry of the XCF scanner³.

4.6.5.3 Dual-energy decomposition

One way to get a material decomposition also for 2D images, is the so called dual-energy decomposition[127–131]. Here a decomposition of the two materials is enabled by two conjunct measurements of the same sample with

²Aluminum is often used as a substitute for bones as it is close to calcium (the main content of bones) in the periodic table[126].

³If the XDF images are acquired also in CT mode (e.g. by a phase-contrast CT machine), the visibility-hardening correction could also be directly applied to the 3D volume.

different X-ray spectra (usually a very low kVp and a high kVp scan with additional low-energy filtering). This method allows in theory for a good segmentation between soft-tissue and all bones. However, in practice the segmentation will never be ideal, as on the one hand there will be a significant overlap in the X-ray spectra and on the other hand, imaging noise will complicate the segmentation even further. Additionally, this method requires some calibration effort. Nevertheless, for the scanning geometry implemented in the actual prototype, such a measurement could easily be implemented by rapid kVp switching between the individual X-ray pulses.

4.6.5.4 Bone removal algorithms

Another elegant way is the segmentation and removal of the bones directly from an imaging processing step[132], as this method does not require any additional measurements or calibrations. This rib removal software can either be applied directly to the XDF-images to remove all signal of the ribs, or can be used to estimate the thickness of the ribs (based on the transmission image), to apply the two fold visibility-hardening correction explained above. The second approach would preserve any real XDF signal coming from the microstructure of the ribs, while the direct image processing based removal would allow for a better assessment of the lung, similar to the purpose of conventional rib removal software for transmission images. However, there is no software available yet which also removes the spine and other bones. It is therefore only suitable to address the VH-XDF signal behind the ribs.

4.6.5.5 Results: proof-of-principle

To verify the feasibility of the two fold correction approach, for the pig phantom the two material maps (“bone” and “soft-tissue”) were calculated using the projection of the segmented CT data of the pig. In Fig. 4.16 the application of this correction approach on the simulated pig data is shown. Fig. 4.16a presents the VH-XDF image of the pig without any corrections. The remaining bone artifacts after a simple correction with POM are shown in Fig. 4.16c. As for the phantom a bone segmentation based on the HU values was available, the VH-XDF signal solely caused by these bones is visualized in Fig. 4.16b. To correct for the remaining bone artifacts, Fig. 4.16d presents the results of two fold correction of the segmented soft-tissue by POM and the segmented bones by aluminum with Eq. (4.16). Here almost no artifacts are visible anymore. As can be seen in the line plots (Fig. 4.16e), the two-fold correction with POM and aluminum corrects the original visibility-hardening artifacts almost completely, without introducing new artifacts. As

neither POM nor aluminum mimic soft-tissue or bones perfectly, there are still some very small artifacts left which will never be corrected to 100% unless a correction with an identical calibration material is performed.

4.6.6 Discussion & Summary

In this chapter, the effects of visibility-hardening on the XDF images of heavily attenuating samples like a thorax were discussed. It was shown that POM is a suitable calibration material for soft-tissue, however not for bones. To correct for the remaining bone artifacts, the image has to be decomposed into a “soft-tissue” component and a “bone” component and the visibility-hardening correction has to be applied separately (soft-tissue corrected by POM, and the bones corrected by aluminum).

To obtain these bone and soft-tissue maps, different approaches were discussed. However, the feasibility of such a segmentation and the resulting correction was only shown on simulation results. For real samples, one has to either accept the bone artifacts, or would have to apply one of the other segmentation approaches discussed. These will be most likely the dual-energy decomposition or image-based approaches, as CT data generally might not be available for most imaged samples. In addition, the correlation of projection images with CT data is usually not easy for real measurements (as already discussed in section 4.4).

Further, the measurement process for such VH-calibration datasets has been discussed, especially with the focus of additional Compton-scattering contributions in these datasets. It was shown that a positioning of the equivalent absorber close to the X-ray tube reduces the Compton content significantly.

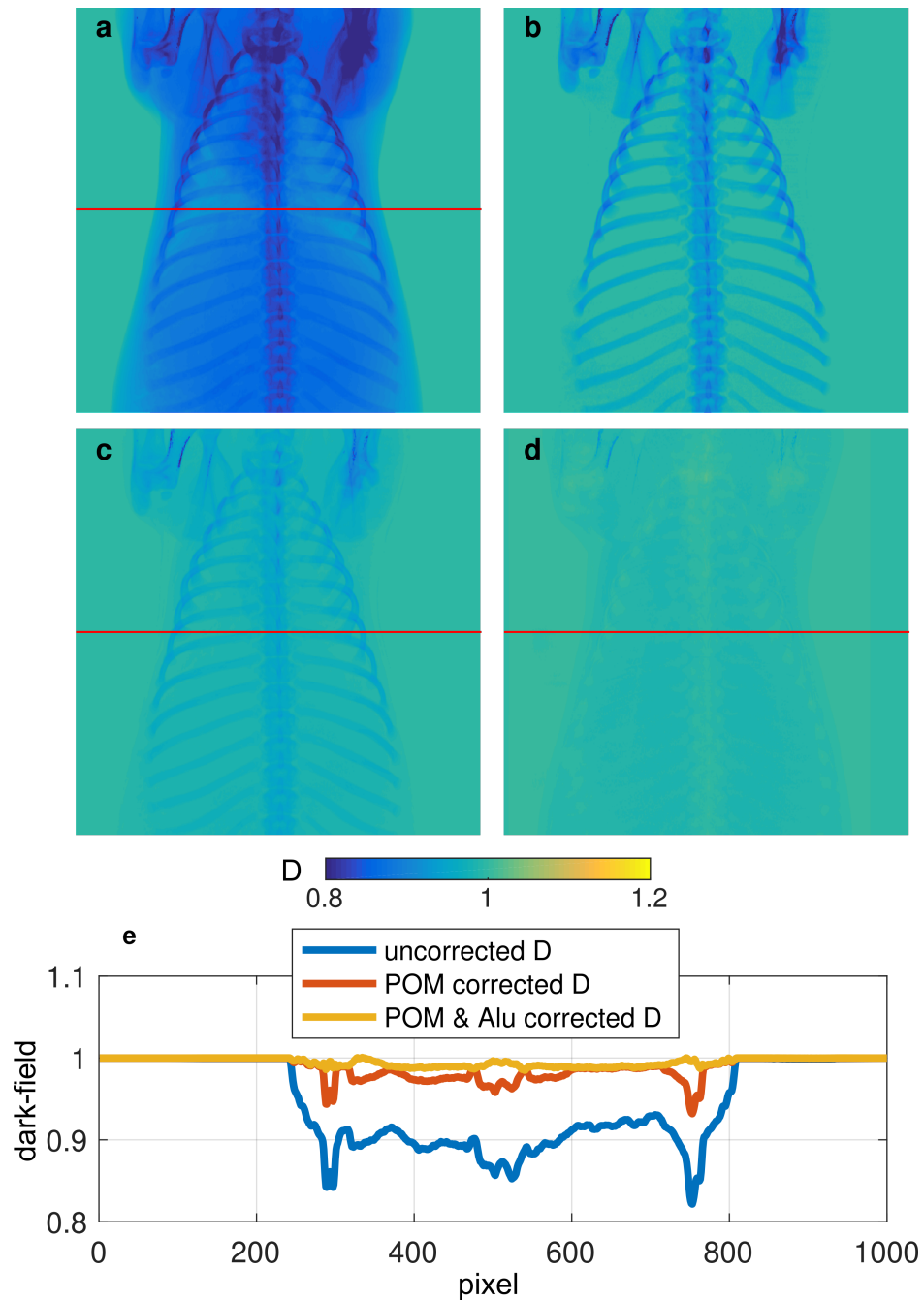


Figure 4.16 Correction for the bone artifacts remaining after a POM calibration: (a) VH-XDF signal caused by the visibility-hardening of the pig as already shown in Fig. 4.14. (b) VH-XDF signal solely of the bones, (obtained by a segmentation of the CT data into a bone map and a soft-tissue map). (c) Remaining bone artifacts after a VH-correction of (a) solely with POM. (d) Two-fold VH correction with POM and aluminum using Eq. (4.16). (e) Line-profiles of the three red lines to better compare the different correction methods.

kVp	50	60	70	80	90	100	120
$K[\mu\text{Gy}]/\text{mA}$	0.96	1.51	2.14	2.91	3.86	4.92	7.25
$\text{CF}[\text{mSv}/\text{mGy}]$	0.056	0.077	0.095	0.110	0.123	0.135	0.161

Table 4.7 Measured dose values: Measured incident air kerma (K) per tube current (mA) for a standard slot-scan with 25 pulsed exposures per pixel (20 ms X-ray window). In addition, the interpolated conversion factors CF from Fig. 4.17 are listed for the different tube voltages.

4.7 Radiation dose

Assuming an adequate similarity between porcine and human thoraxes (at least for PA projections), the conversion factors given in ICRU 103 together with the organ doses from [133] were used to calculate a rough estimate of the effective radiation dose applied to the pigs and other samples. As explained in section 2.4 on page 24, this conversion factor CF can be used, to convert the measured incident air kerma K into an effective patient dose ED

$$ED[\text{mSv}] = CF \left[\frac{\text{mSv}}{\text{mGy}} \right] \cdot K[\text{mGy}], \quad (4.18)$$

under the assumption that the imaging procedure and the sample of interest are sufficiently similar to the chest imaging procedure defined for a standard human in ICRU 103. As these conversion factors are only tabulated for a few kVp values, a cubic interpolation was applied to get conversion factors also for other kVp values. The results of this interpolation are given in Fig. 4.17. For the developed prototype, the incident air kerma at the table was measured by a PTW NOMEX dosimeter (PTW, Freiburg, Germany) for different kVp values for a standard slot-scan of the full FOV. For such a scan with 25 pulsed exposures with 20 ms X-ray window, the dose values listed in Table 4.7 were recorded. Additionally, the table gives the interpolated conversion factors CF for the effective dose.

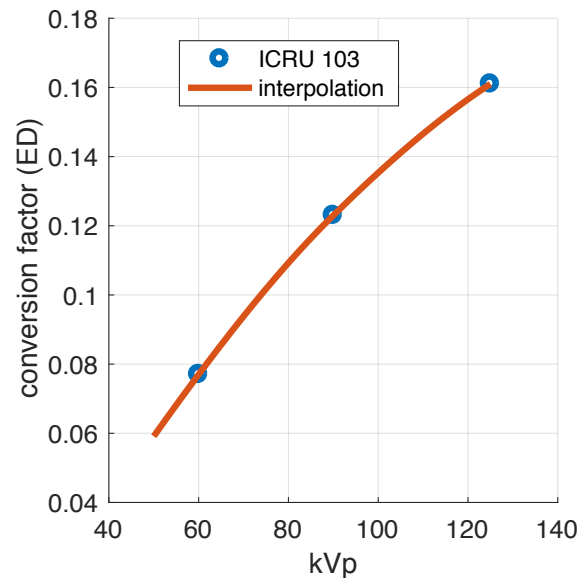


Figure 4.17 Dose conversion factors: Conversion factors calculated from [76] and [133] and their cubic interpolation to get values for other kVp.

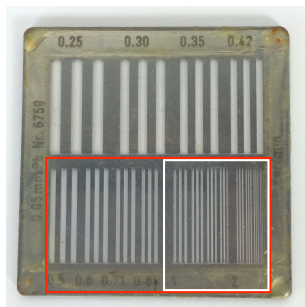


Figure 4.18 Resolution pattern: Photo of the resolution test pattern with the two ROIs analyzed in Fig. 4.20 (red) and Fig. 4.21 (white).

4.8 Resolution limits

4.8.1 Motivation

For human X-ray imaging applications the German guideline “Richtlinie für Sachverständigenprüfungen nach der Röntgenverordnung (SV-RL)”[134] regulates the resolution limits which have to be achieved for different types of diagnostic X-ray exposures. The resolution is only defined for attenuation images and is typically measured with a line-pattern made of lead as shown in Fig. 4.18. It is given as the highest number of line-pairs per mm (lp/mm) which still can be resolved by the human eye (of the evaluating expert) in the X-ray attenuation images. In order to further standardize the procedure, the guideline requires the measurements to be done with a certain detector dose (not patient dose).

For example, the guidelines require for a generic radiographic exposure “*Untersuchungen mit digitaler Durchleuchtung u. Radiographie allgemein*”[134, point 12, page 142] a resolution of $R_{Gr} \geq 1.2 \text{ lp/mm}$ at a maximum detector dose of $2 \mu\text{Gy}$. In general, the guidelines allow more dose for exposures with higher resolution and vice versa. However, as XDF imaging is not part of these guidelines, there are no limits for this new method yet defined. Additionally, in case of lung imaging a strict resolution limit for the XDF images seems unreasonable, as the increased image noise (compared to the conventional attenuation images) has to be counterweighted by increased post-processing smoothing of the XDF images. Therefore, in this paragraph the resolution limits of the developed XDF-scanner are measured only in the attenuation images under different conditions to evaluate the compliance of the developed prototype with the current guidelines. This information might help in future to register the scanner (or its successor versions) for human

binning	real pixel size [μm]	effective pixel size [μm]	frame rate [Hz]
1x1	148	120	4
2x2	296	240	6
3x3	444	360	12

Table 4.8 Available detector modi.

applications.

4.8.2 Methods

As it would be beneficial for the registration process to meet the requirements of an existing imaging method as close as possible, the measurements were done with two different dose levels: a “low dose” version with $2.5 \mu\text{Gy}$ detector dose per image and a “high dose” version with $5 \mu\text{Gy}$. The detector dose was calculated from the detector pixel counts (LSB) in the image using a factory conversion factor given by the manufacturer which is valid for the used 70 kVp tungsten spectrum. For the detector, the modi shown in Table 4.8 were used.

For comparison and classification of the measurements, the theoretical resolution limits were calculated [135, 136] from the system parameters by using the post-sample Modulation-Transfer-Function (MTF). The results are shown in Fig. 4.19. This function quantifies the loss in contrast/resolution due to the blurring caused by the focus size and most importantly the sampling with a finite pixel size (therefore called “post-sampling”). Please note, that this MTF differs from the pre-sampling MTF which is usually measured by an edge and that excludes especially the influence of the pixel size. The theoretical resolution limit in line-pairs per mm is given by the zero-crossing of the post-sampling MTF. However, the realistically achievable resolution will always be (much) smaller than this theoretical optimum.

4.8.3 Results

Fig. 4.20 and Fig. 4.21 show the attenuation images of the resolution pattern, imaged at 70 kVp with a conventional phase stepping approach with 5 steps for different detector binning modes (1×1 , 2×2 and 3×3) and different focal spot sizes (0.3 mm and 1.0 mm). As can be seen in the images, the dominating factor for the resolution is the detector binning as expected from the theoretical calculations (compare Fig. 4.19). The focal spot size becomes

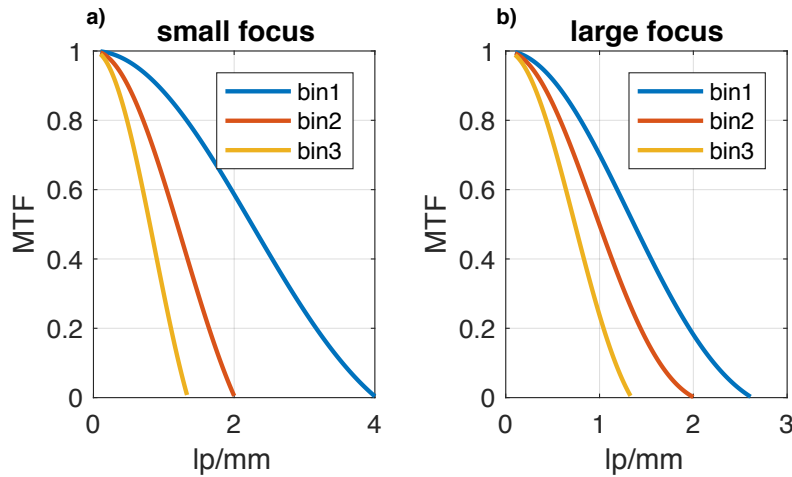


Figure 4.19 Calculated post-sampling modulation-transfer-function: (a) MTF for the small focus (0.3) and (b) large focus (1.0) with the three binning modes. The theoretical resolution limit ($MTF=0$) is only for the 1×1 binning defined by the focus size. For larger binning (2×2 and 3×3) the pixel size is the dominant factor.

the bottleneck only for the 1×1 binning. An overview of the resolution limits is given in Table 4.9 together with the theoretical values. As can be seen, the measurements are well compatible with the latter. For the 3×3 binning a maximum resolution of about 1 lp/mm can be expected. The measurements with double the dose appear a little less noisy, however with the discrete number of structured fields in the line patterns, the doubling in the dose is not sufficient to increase the measured resolution limit to the next step. For line-patterns with finer samplings the slight increases in the resolution might become measurable.

4.8.4 Discussion & Summary

For a realistic operation mode (3×3 binning, large focus), the developed prototype does not comply with the current guidelines for medical X-ray devices. Most likely a new device category needs to be defined for XDF devices with relaxed constraints on the achievable resolution in the attenuation image. However, if higher resolutions than the currently achievable 1 lp/mm are still requested from the authorization agency, a faster detector would be needed as for the current detector only the 3×3 binning allows for a scanning time of 40 s or less, due to the limited detector readout speed (12 Hz for 3×3 binning and only 4 Hz for 1×1 binning). With a faster detector, the raw

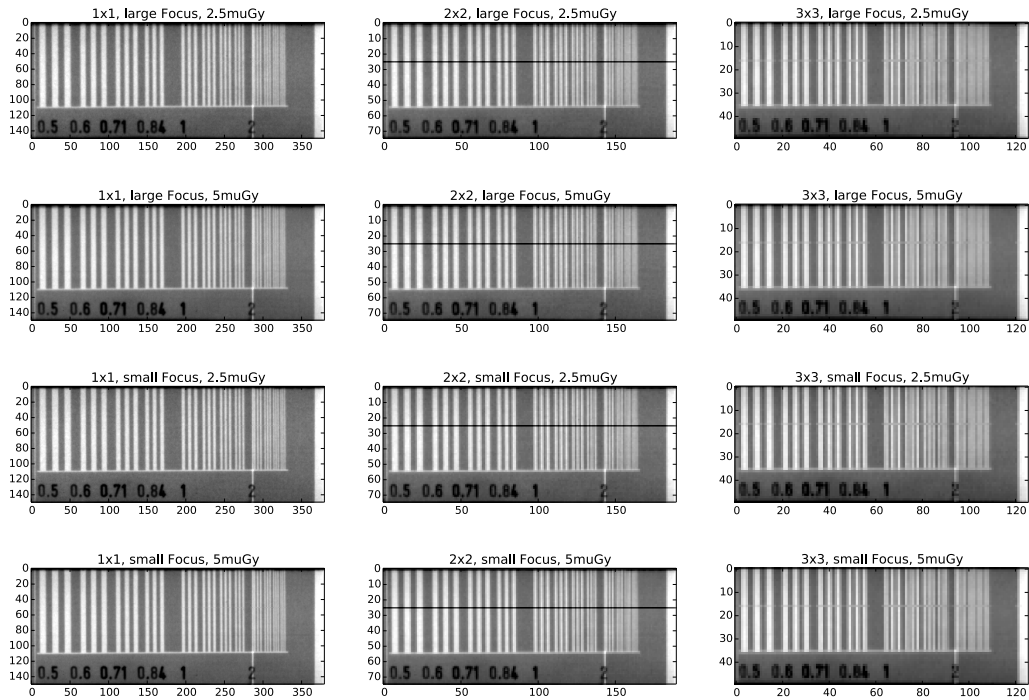


Figure 4.20 Resolution measurements - overview: Transmission images of the resolution pattern with the two different focal sizes (0.3 mm and 1.0 mm), with the three binning types (1×1 , 2×2 and 3×3) and for a “low” detector dose of $2.5 \mu\text{Gy}$ and a “high” detector dose of $5 \mu\text{Gy}$. The black line for the 2×2 binning results from a broken detector pixel line which is also visible in the 3×3 binning. The achievable resolutions are summarized in Table 4.9.

data could be acquired in a 1×1 or 2×2 binning mode, allowing for a high-resolution attenuation image, while the data could still be software binned when calculating the XDF image (to reduce the noise). Using a smaller focal spot is generally undesired, as it would reduce the maximum available tube power drastically, due to heat problems.

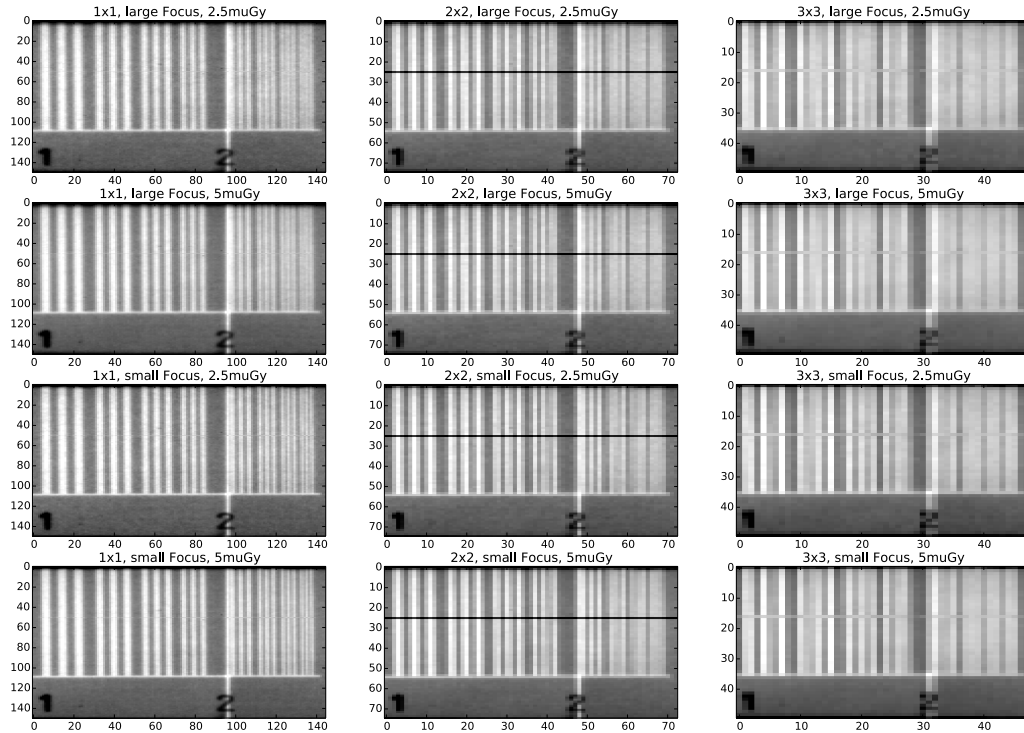


Figure 4.21 Resolution measurements - zoom: Magnification of the high frequency part of the images shown in Fig. 4.20.

	binning	low-dose	high-dose	theory
large focus	1×1	2.25	2.25	2.61
	2×2	1.50	1.50	2.0
	3×3	1	1	1.33
small focus	1×1	2.5	2.5	4.0
	2×2	1.5	1.5	2.0
	3×3	1	1	1.33

Table 4.9 Summary resolution limits: The number of line pairs per mm which can be distinguished by eye, estimated from Fig. 4.20 and 4.21 and the theoretical limits from Fig. 4.19.

parameters	“standard”	“medium”	“fast”
motor speed [mm/s]	11	14	22
scan time [s]	40	30	20
detector frame rate [Hz]	11.6	16	16
X-ray window [ms]	20	10	10
#shots per pixel	25	25	17

Table 4.10 Scanning parameters: Additional scanning configurations to allow for faster scanning.

4.9 Scanning speed optimization

4.9.1 Motivation

The image of a full thorax should be acquired during a single scan with paused breathing, as otherwise motion artifact would occur. For animal welfare, this (induced) breath stop should not last longer than one minute for pigs. For human application, already 20 seconds would be very demanding, especially for patients with impaired lung functions. In the following, the performance of the developed XDF-scanner under different scanning speeds is analyzed with the aim of finding the shortest possible scan time.

4.9.2 Methods

To allow for higher imaging speeds, the X-ray window has to be reduced to allow for higher read out speeds of the detector, or by reducing the number of exposures per pixel. With this two handles two more scanning modes were defined and are listed together with the “standard” one in Table 4.10. The drawback of both these scanning modes is that they allow only for half or even less tube power as used for the standard scan.

4.9.3 Results

Fig. 4.22 shows the XDF images of an arrangement of several scatter-plates, acquired with three different motor speeds for the swing motion. For speed settings above 12 mm/s, the motor starts to vibrate and these vibrations couple into the gratings, resulting in the wave like imaging artifacts shown in Fig. 4.22b and Fig. 4.22c. The same happens for much lower speeds around 3 mm/s (not shown), as the gear of the motor gets into resonance here. A scanning speed of 11 mm/s does not show any vibration artifacts

(Fig. 4.22a), however, limits the scanning time to about 40 s for the full FOV of $32 \times 35 \text{ cm}^2$.

4.9.4 Discussion & Summary

Obviously the motor used for the swing is sufficient for animal imaging but not the optimal choice, due to the vibrations introduced for speeds above 12 mm/s. As this motor allows only for a scan time of around 40 s it is unsuitable for human applications. A better motor (with fewer vibrations) would allow for faster scanning. However, the X-ray tube and detector will become the bottleneck at some point. Faster scanning would therefore also require faster readout of the detector which is possible using the latest version of the Pixium RF 4343 that allows for a readout speed of up to 23 Hz. At some imaging speed, also the X-ray tube will no longer be able to provide the necessary X-ray power in the desired scan time and will therefore also require an upgrade. Increasing the slot width would then help to relax the constraints on the X-ray tube again, as less power would be wasted. For example, if the slot size would be doubled to 5 cm, and the latest version of the detector would be implemented, it would easily allow for scan times below 20 s, with the same applied radiation dose as the current “standard scan”. However, this would then also require a new, vibration-less motor.

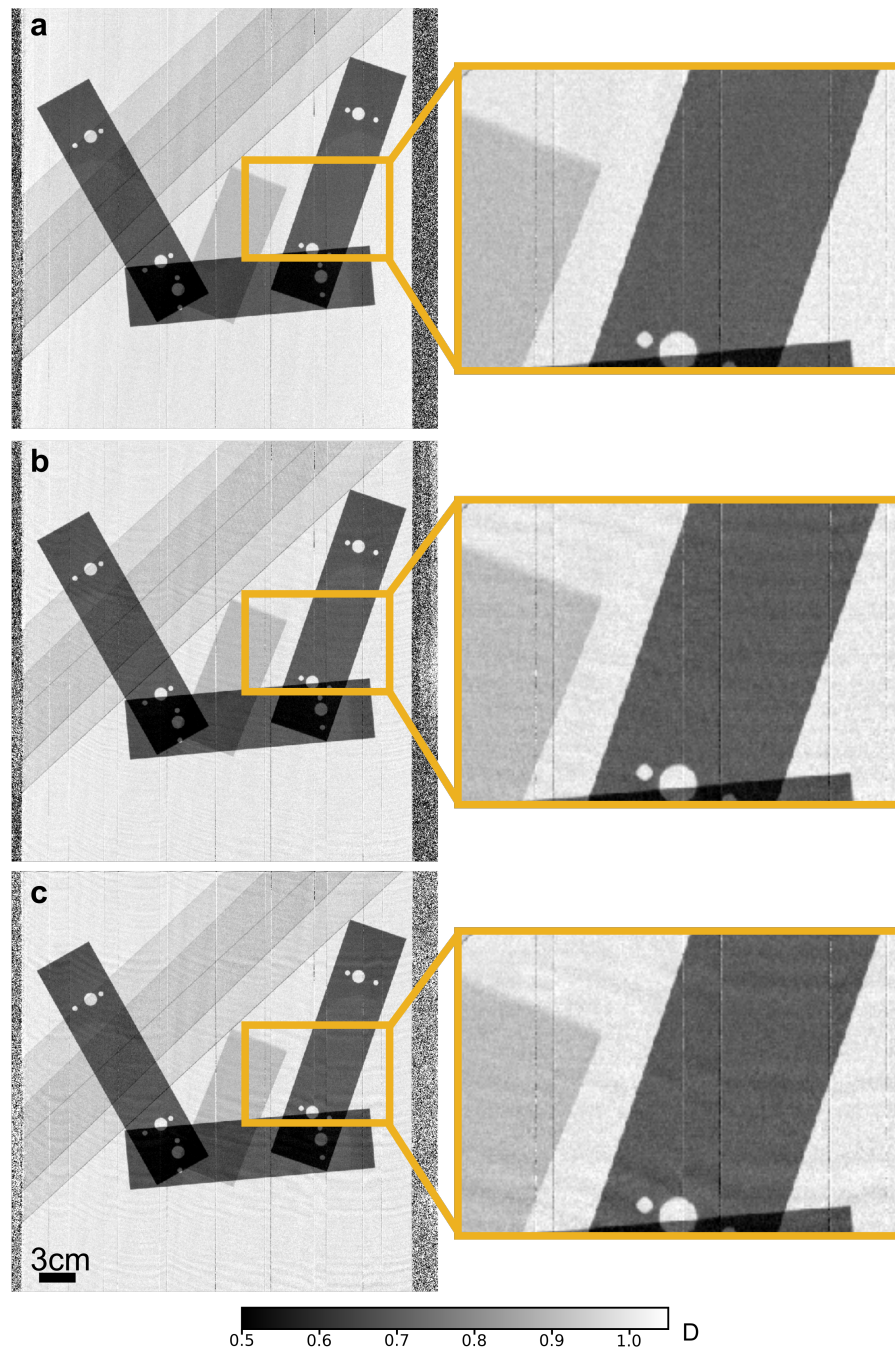


Figure 4.22 *Vibration artifacts.* XDF images of some scatter-plates, imaged with three different speeds ((a) 11 mm/s, (b) 14 mm/s and (c) 22 mm/s) of the swing motor, resulting in scan times of 40 s, 30 s and 20 s, respectively. Above 11 mm/s motor speed (b), vibration artifacts show up which increase for the highest speed of 22 mm/s (c).

4.10 Summary: Characterization of the prototype

In this chapter, the developed prototype was characterized extensively. The achievable visibility was measured energy-resolved and compared to simulations. Together with further measurements of a test phantom, the optimal tube voltage was estimated to be around 60-70 kVp for an XDF image of a thorax. Lower tube voltages might even be better, however are hindered by the limited output power of the tube at these energies.

In a next step, the influence of Compton-scattering on the expected XDF images of a thorax were analyzed. It was found that Compton-scattering creates a pseudo XDF signal especially behind heavily attenuating structures like bones. Based on the Monte-Carlo simulations, a correction method for these artifacts was proposed.

Further, the influence of beam/visibility-hardening was analyzed. To correct for the artifacts introduced by the visibility-hardening, a two-step calibration method was proposed which corrects bones and soft-tissue separately.

Finally, the measurement protocol was optimized with respect to the achievable imaging speed. With the currently implemented hardware a scanning of the full FOV of $32 \times 35 \text{ cm}^2$ is possible in about 40 s. However, this requires the detector to be operated in a hardware binning of 3×3 pixels which limits the resolution to about 1 lp/mm. To further increase the imaging speed and/or to increase the resolution, improved hardware components would be needed.

All together the performance of the system is very satisfying and there are no more concerns to continue with the first in-vivo experiments with real pigs.

Chapter 5

Applications: Porcine chest imaging

In the previous two chapters, the technical functionality of the developed scanner was discussed in detail. As the image quality and scan speed were sufficiently high, it was justified to continue with the first in-vivo imaging experiments. The results of these experiments are presented in the following chapter. Note that parts of the content of this chapter have been published previously by Gromann, De Marco et al. in Nature Scientific Reports (2017). Figures and text passages in this section may appear similar or identical as in the publication.

Contents

5.1	First in-vivo porcine chest images	107
5.2	Tube voltage optimization	113
5.3	Motion artifacts	114
5.4	Visibility-hardening and CS corrections	116
5.5	Summary & Outlook	117

5.1 First in-vivo porcine chest images

5.1.1 Motivation

The lung consists of several hundred million air-tissue interfaces (formed by alveoli walls) that provide sufficient gas exchange for breathing. As clinically used conventional attenuation-based radiography of the lung cannot resolve these microstructures, its diagnostic window is mostly restricted to indirect signs caused by late-stage pathologies. In contrast, XDF radiography[12] is

sensitive to the pulmonary micro-morphology itself, as the aforementioned interfaces cause significant ultra-small-angle X-ray scattering and a corresponding XDF signal. Recent small-animal studies demonstrated that XDF imaging enhances pulmonary diagnosis, e.g. for the early detection and staging of COPD[18, 22, 24, 26], pulmonary fibrosis[25], pneumothoraces[27] and neonatal lung injury associated with mechanical ventilation[28]. Furthermore, the assessment of pulmonary carcinoma[29, 67], edema, as well as pneumonia may significantly benefit from XDF imaging. These pathologies are characterized by a destruction (as in the case of COPD) or densification (by fibrotic or tumorous tissue) of the natural alveolar structure as the disease progresses. The loss of air-tissue interfaces consequently results in a reduction of the XDF signal compared to the distinct signal of healthy lung tissue. Hence, variations in the XDF lung pattern can indicate pathological changes. The combination of XDF with conventional imaging can further be used for differential diagnosis[137].

However, XDF chest imaging has until now been limited to the investigation of small animals or ex-vivo samples. In-vivo imaging of larger mammals still posed substantial technical challenges. Therefore, in this chapter the first in-vivo XDF chest radiographs with a FOV of $32 \times 35 \text{ cm}^2$ of living pigs are presented.

5.1.2 Methods

5.1.2.1 Animal handling

For these experiments German Landrace Hybrid pigs (wild-type, Institute of Molecular Animal Breeding and Biotechnology, Ludwig Maximilian University Munich breeding facility) were used. All animal procedures were performed with permission of the local regulatory authority, Regierung von Oberbayern (ROB), Sachgebiet 54, 80534 Munich, approval number AZ 55.2-1-54-2532-61-2015. The application was reviewed by the ethics committee according to §15 TSchG German Animal Welfare Law. All experiments were performed in accordance with relevant guidelines and regulations.

If not stated differently for the individual experiments, all animals were treated identically: first, the animals were sedated by intramuscular application of Ketamine (Ursotamin®, Serumwerk Bernburg, Germany, 20 mg/kg) and Azaperone (Stresnil®, Elanco Animal Health, Bad Homburg, Germany 2 mg/kg). Anesthesia was then continued by intravenous injection with Propofol (Propofol 2%, MCT Fresenius, Fresenius Kabi, Langenhagen, Germany) using a syringe pump (Injectomat® MC Agilia, Fresenius Kabi, Langenhagen, Germany) with the dose adjusted to the animals response. The

intubated animals were kept under automated ventilation throughout the full experiment by an anesthesia machine (Dräger Fabius Plus®, Draegerwerk AG & Co. KGaA, Lübeck, Germany). For imaging, ventilation was paused for the duration of the scan (maximal 60 s at a time) with a constant pressure of about 11 mbar in the airways, simulating an intermediate depth of respiration. Heart rate and oxygenation were monitored continuously. To terminate the experiment, the animals were euthanized under anesthesia by intravenous injection of T61® (Intervet GmbH, Unterschleissheim, Germany) according to the manufacturer's instructions.

Fig. 5.1 shows how the intubated, anesthetized and mechanically ventilated animals were placed on the sample bed/table in the scanner. The schematic in Fig. 5.1a illustrates how the gratings are moved relative to the body axis of the animal. The photographs in Fig. 5.1b-c show the additional lead shielding ("side collimators") which are visible next to the animal, as well as the silicon pipes for the automatic breathing control via the intubation tube.

5.1.2.2 Imaging parameters

The proof-of principle images presented in the following were acquired with the standard scan parameters as listed in Table 4.10 for a 70 kVp spectrum with 340 mA tube current. The X-ray tube at the time of the experiment was a Philips RO 1750 ROT 360 (Philips Medical Systems, Hamburg, Germany). The dose for this experiment was measured and calculated as described in section 4.7 to be approximately 80 μSv per scan. For the XDF images, a visibility-hardening correction with solely POM (on-table method which also tries to correct for Compton-scatter, see section 4.6.4) has been applied.

5.1.3 Results & Discussion

Fig. 5.2 illustrates as an example the results obtained for one animal (ear-number #4752, 23 kg) in posterior-anterior view with 19.5 cm chest thickness (PA, Fig. 5.2 top row) and in lateral view (lying on its right side) with 16 cm lateral chest thickness (LAT, Fig. 5.2 bottom row), respectively. Both exposures (PA and LAT) were conducted with the same dose area product (DAP) of $0.5 \text{ Gy} \cdot \text{cm}^2$, resulting in an effective dose of approximately 80 μSv for the PA exposure. This value is compatible with conventional chest radiographs (20 μSv for PA examinations[138, 139]) and equals around ten days of natural background radiation[138].

When comparing XDF (Fig. 5.2c-d) with the conventional radiographs (Fig. 5.2a-b), the diagnostic benefit of scatter-sensitive imaging in lung diagnostics becomes apparent: the XDF signal allows functional assessment of

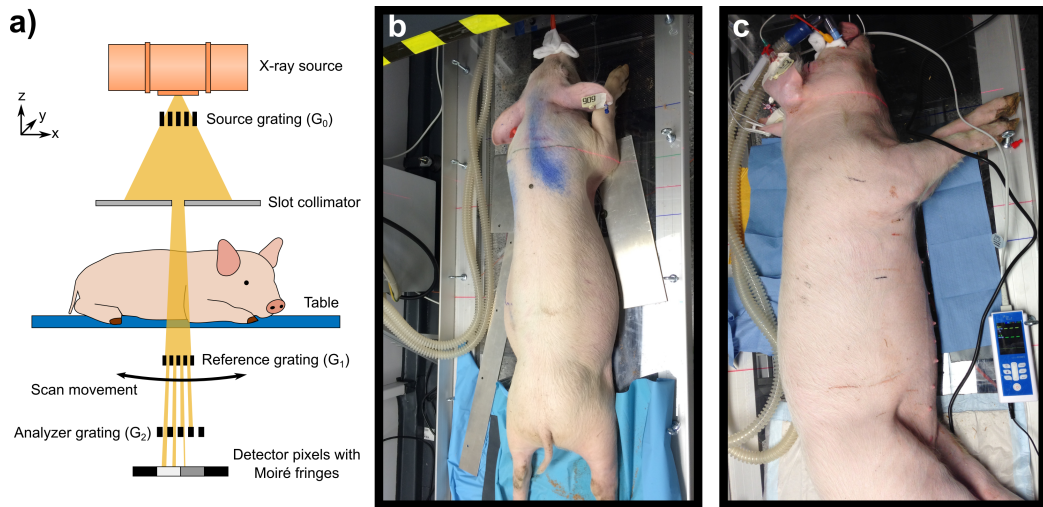


Figure 5.1 Photographs and sketch of the experimental setup with the animals: (a) Sketch of the imaging system with the animal placed on the table, (b) photograph of an animal in posterior-anterior (PA) position and (c) photograph of another animal in lateral (LAT) position. As the image in (c) was taken after termination of the experiment, there is no heartbeat visible on the pulsoximeter. Next to the animals, the additional lead shielding (“side collimators”) are visible, as well as the pipes for the automatic breathing control via the intubation tube. The red laser line is used for positioning of the animals. Please note that an adapted version of panel (a) is also published in [68].

the porcine lung, since the associated scattering signal is dominant in the thorax region. At the same time, the overlying and surrounding structures (e.g. fat, muscles and bones) hardly exhibit any scattering and therefore appear “dark-field transparent”. Thus, they do not compromise the assessment and delineation of the lung, as it is the case in attenuation radiographs. Note that the presented radiographs have sufficient quality to guarantee a meaningful radiographic assessment of the lung: the XDF signal exhibits a homogenous distribution/pattern throughout the lung, as expected in healthy animals. In order to demonstrate the potential of the complementarity between XDF imaging and conventional radiography, Fig. 5.3 shows two regions of interest with similar attenuation but different XDF characteristics: healthy lung tissue with a large number of alveolar interfaces yielding a strong XDF signal versus the air-filled stomach with no inherent microstructure and thus no XDF contrast. Experiments with mice[22, 24–28, 140] proved that the XDF signal strength is directly correlated to the number of intact alveolar interfaces.

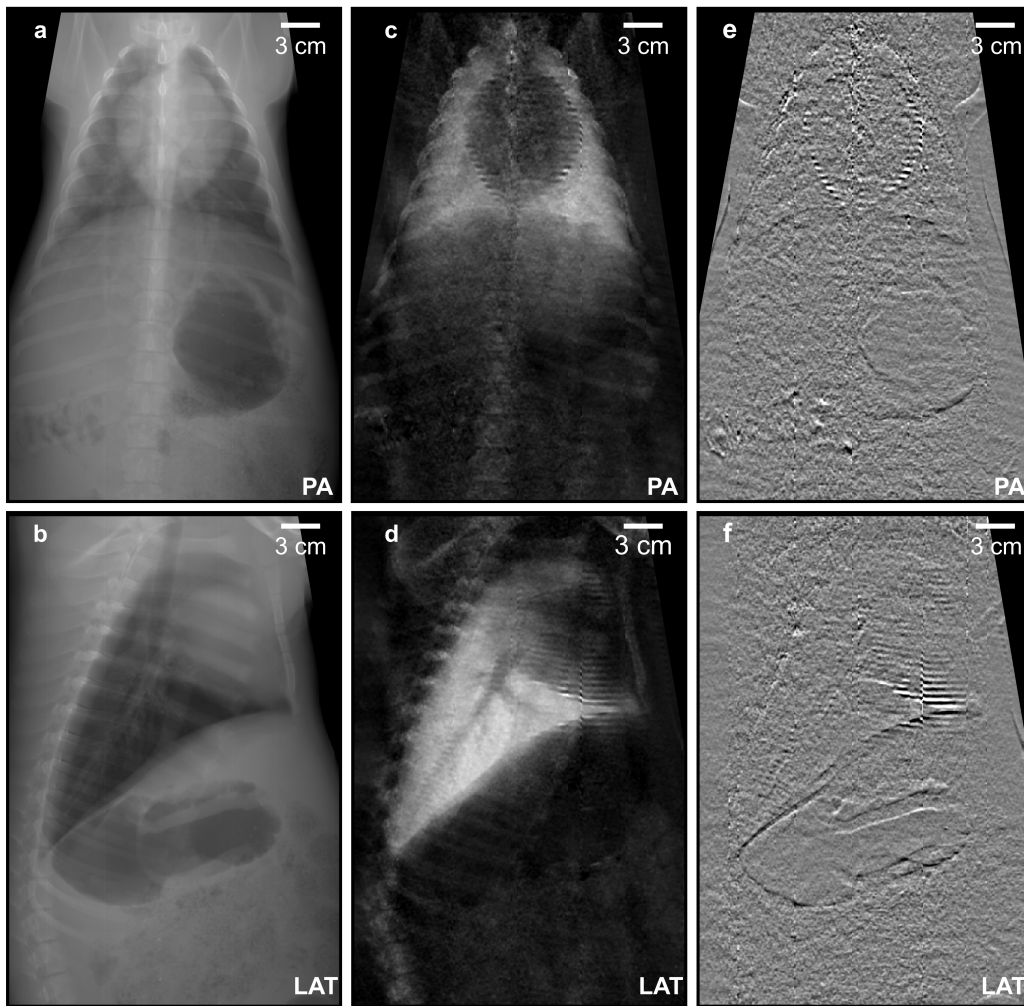


Figure 5.2 *First in-vivo porcine multi-contrast chest radiographs. Attenuation (a, b), X-ray dark-field (c, d) and differential phase (e, f) chest radiographs of a healthy, living pig in posteroanterior (PA) and lateral (LAT) view (top and bottom row respectively). Both scans were conducted using imaging parameters compliant with animal care, namely 40 seconds total scan time and a radiation dose of approximately $80 \mu\text{Sv}$. In particular the XDF radiographs (c, d) allow for an easy and unambiguous assessment of the pig lung, since overlying structures (e.g. fat) present only negligible scattering, and the XDF signal strength is correlated to the number of alveolar interfaces. Please note: images (a-d) are displayed as the neg. natural logarithm of relative transmission and visibility loss respectively. This figure is also published in [68].*

Therefore, any pathology associated with their loss will continuously reduce

the XDF signal up to the point where no interfaces are left at all. This opens up a new diagnostic window to detect early stages of respiratory diseases which typically appear radiolucent on the attenuation radiograph. The extreme case, in which lung tissue/alveolar interfaces are completely displaced by air, would e.g. occur in a pneumothorax or bulla, for which the air-filled stomach is only considered as an educational and demonstrative model here. The scatterplot in Fig. 5.3b further demonstrates the feasibility (in the case of pigs) of discriminating tissues with similar attenuation properties based on their XDF signal intensities.

Besides the attenuation and XDF images, GBI also provides differential-phase images[10, 11, 47]. These are shown in Fig. 5.2e-f. However, note that the system was designed to accommodate the strong signal expected for pulmonary XDF imaging and hence only yields a moderate phase sensitivity[63]. Therefore, the differential-phase images of the in-vivo pig in these experiments provide little additional information (compare Fig. 5.2e-f).

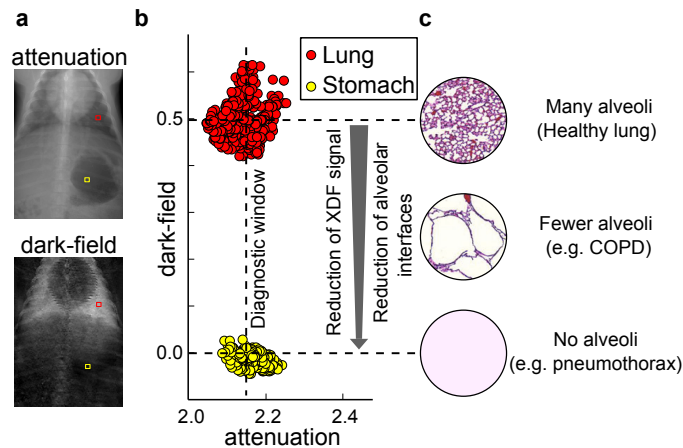


Figure 5.3 Potential of XDF imaging. (a) Two regions of interest with similar attenuation signals but different XDF behavior showcase the diagnostic potential of XDF imaging. (b) Scatterplot comparing healthy lung tissue (red) with intact alveolar interfaces and a strong XDF signal vs. the air-filled stomach (yellow) with no internal microstructure and thus a small XDF value. As the XDF signal strength is directly correlated to the number of alveolar interfaces, a loss of the latter due to respiratory diseases, as indicated in the example of histopathological slices in (c), can be diagnosed even if the attenuation signal remains unaltered. The diagnostic window ranges up to the point where no alveoli are left which is the case e.g. in a pneumothorax. For this extreme case, the air-filled stomach is considered only as a demonstrative model here. This figure is also published in [68].

kVp	60	70	90	120
dose [μ Sv]	70	142	120	175

Table 5.1 Scan parameter for the kVp series.

5.2 Tube voltage optimization

5.2.1 Motivation

So far, the optimal tube voltage for XDF imaging of a chest was only estimated for a technical phantom in section 4.3. To verify that these results are also valid for imaging of a real thorax, these experiments are repeated here for a porcine thorax.

5.2.2 Methods

For this experiments, the much stronger MRC X-ray tube was used (see chapter 3.4) to allow for consecutive scans with no delay time. A pig (ear-number #1893, female, 25 kg) was imaged several times in PA position with different kVp values as listed in Table 5.1. The procedures for the animal handling are the same as discussed in section 5.1.2.1. As the appropriate dose-conversion factors were not yet available at the time-point of the experiments, the dose could not be kept completely constant for the different kVp values and the corresponding values are therefore given in the table as well. Again, a visibility-hardening correction with solely POM (on-table method) has been applied and the images are given with a logarithmic colormap.

5.2.3 Results & Discussion

Fig. 5.4 shows in the upper row the attenuation and in the lower row the XDF images for different kVp values. As can be seen, the thorax becomes slightly more transparent for the higher kVp values and the contrast of the bones decreases (Fig. 5.4a-d). From a radiological point of view the XDF image is best for 60 kVp (Fig. 5.4e) and gets continuously worse for higher kVp, as anatomical details of the lung are best visible for 60 kVp. This is correlated with the high XDF signal of the lung at these energies. Besides the loss in signal strength additional artifacts are introduced for higher tube voltages. The origin of these artifacts is not yet fully understood but might be related to problems in the data processing due to the low visibility for higher kVp values. The quantitative evaluation of the white ROI from Fig. 5.4 is

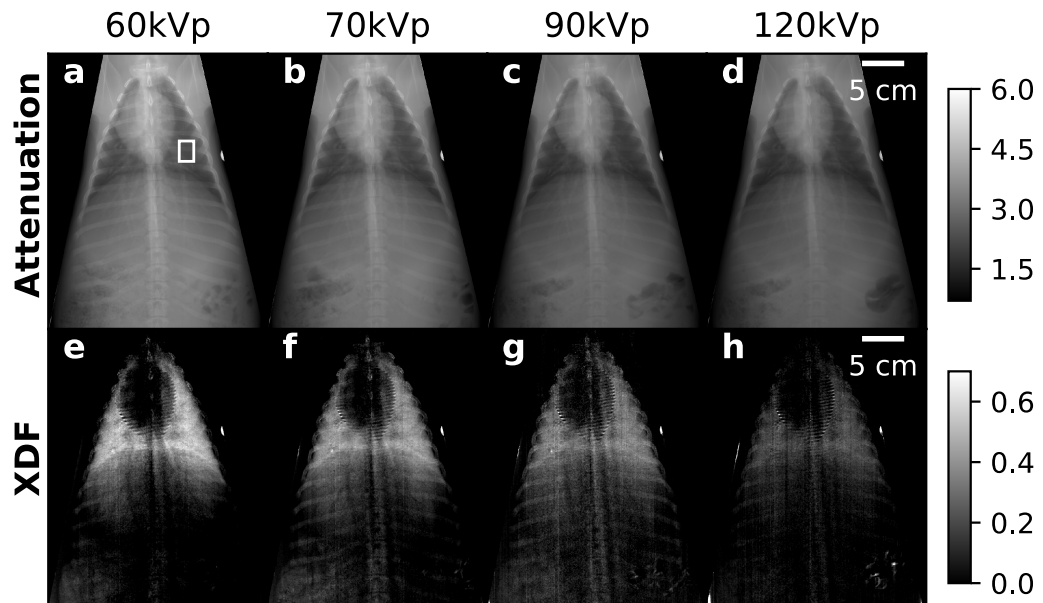


Figure 5.4 kVp Series: Pig imaged at different kVp values with the dose values given in Table 5.1. The XDF images for the lowest energy of 60 kVp yield the best quality with decreasing performance for higher kVp values.

presented in Fig. 5.5. As already expected from the experiments presented in section 4.3, the XDF signal decreases for higher energies (compare Fig. 5.5a). In addition, also the SNR (normalized to the applied dose), decreases for higher energies (compare Fig. 5.5b), as the increase in the noise by the loss in visibility cannot be outweighed by the increase in transmission. This is compatible with the results from section 4.3. A further reduction of the tube voltage is not possible due to the limited tube output at energies below 60 kVp, as already discussed.

5.3 Motion artifacts

5.3.1 Motivation

In this section, the motion artifacts inherent for in-vivo imaging are studied. Especially the beating heart, as the major source of motion during a scan, is expected to introduce artifacts. The inherent motion of a living object was

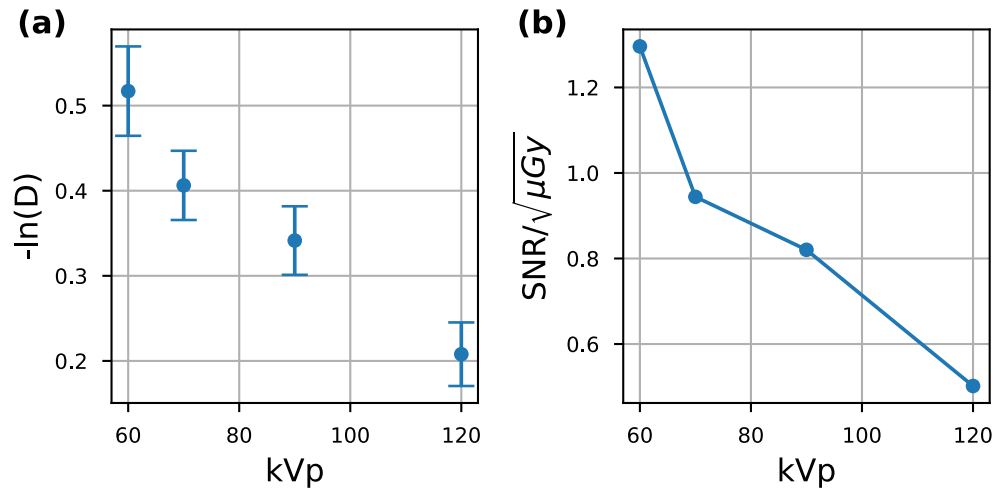


Figure 5.5 Quantitative analysis: (a) averaged XDF signal and corresponding standard deviation of the white ROI inside the lung (see Fig. 5.4). (b) SNR of this ROI, normalized to the applied dose which was not constant for the different scans (see Table 5.1). The lowest kVp yields the best results.

often considered as a major threat in the translation of XDF imaging from bench to bedside.

5.3.2 Methods

To study different types of motion artifacts, a first pig (ear-number #4450, male, 33 kg) was imaged twice; once without breathing control resulting in a quite strong movement of the freely breathing thorax during the scan. For a second scan, the amount of narcotics was increased, and the automatic breathing control was activated. Here the breathing was paused during the scan. For a third scan (pig #4456, female, 30 kg), the Moiré fringe pattern was adjusted to reduce the remaining motion artifacts. All three scans were performed at 70 kVp with a dose of about 80 μSv per scan with the RO 1750 X-ray tube.

5.3.3 Results & Discussion

For a freely breathing animal, the image information is completely lost (see Fig. 5.6a). Holding the breath is therefore inevitable for XDF imaging. Further, the experiments showed that the shape of the Moiré fringe pattern (see upper images in Fig. 5.6) determines the strength of the image artifacts in-

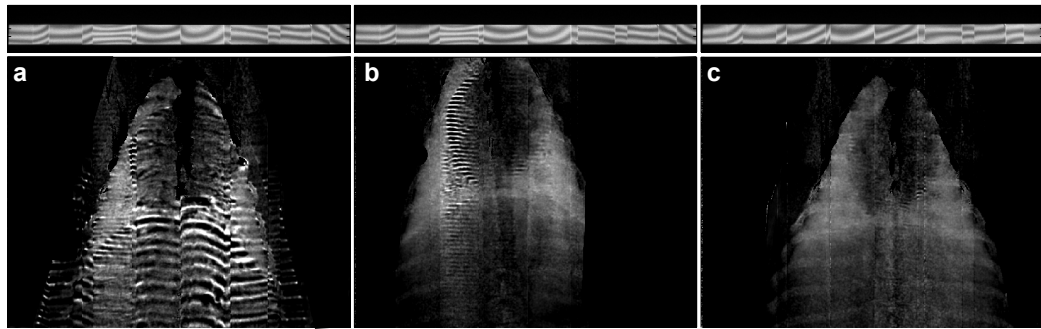


Figure 5.6 *Resulting motion artifacts for different grating alignments. (a) Artifacts resulting from a continuous breathing motion during the scan. (b) Motion artifacts due to bad alignment of one grating tile. (c) optimal alignment of all grating tiles. The upper row shows the raw image of the grating slot with the actual alignment of the Moiré fringes.*

troduced by the beating heart. The fringe scanning procedure assumes that all intensity modulations during a scan are the result of “scanning” through the phase of the Moiré fringe. However, the beating heart introduces an additional intensity fluctuation, especially at the heart-lung boundary, resulting in data inconsistencies. A high frequency in the Moiré pattern amplifies these artifacts as shown for the badly align grating tile in Fig. 5.6b. To reduce these artifacts, a larger fringe period seems to be beneficial (with the upper limit being determined by the requirement that one full period must still be contained in the grating slot to employ the fringe-scanning algorithm). As the remaining artifacts (see Fig. 5.6c) are limited to the heart-lung boundary, they should not degrade the diagnostic quality of the images.

5.4 Visibility-hardening and CS corrections

5.4.1 Motivation

So far, all presented XDF images of pigs (see Fig. 5.2, Fig. 5.4 and Fig. 5.6) have been corrected for visibility-hardening and Compton-scattering at once with the method “POM on table” (compare section 4.6.4), due to the lack of further calibration data. However, this may result in strong image artifacts and wrong quantitative numbers for the XDF signal as discussed in sections 4.4 and 4.6. To allow more quantitative analysis of the XFD signal, the advanced correction methods discussed in the aforementioned sections are applied to real data of the pig.

5.4.2 Methods

Using the Monte-Carlo simulation and the acquired CT data of the pig (ear-number #1893, imaged at 60 kVp in PA with the XDF-scanner), the Compton background was simulated. Using the approach discussed in section 4.4, the measured XDF image is corrected for the pseudo XDF signal caused by Compton-scattering. In a second step, a visibility-hardening correction is applied with the POM slabs placed close to the focal spot. These corrections are then compared to the “old” calibration with POM on table which aimed to correct for visibility-hardening and CS at once. For convenience of visualizing the differences, the images in this section here are color-coded and given with a linear colorbar.

5.4.3 Results & Discussion

For pig #1893, the uncorrected XDF image of the pig is shown in Fig. 5.7a and the correction with the old method “POM on table” is shown in Fig. 5.7b. The profile through the red line is visualized in Fig. 5.8. As can be seen from these images/line plots, there is a strong over-correction in areas outside of the lung (e.g. the shoulders) with XDF signals of up to 1.2 (=20% excess). This is a result of the overestimated Compton-scattering contribution from the POM calibration; The porcine thorax exhibits much less scattering for the same thickness compared to the POM. To correct for this, Fig. 5.7c shows the measured XDF image corrected for the Compton influence by using the results of the MC simulation and Eq. (4.10). In a last step (Fig. 5.7d), a visibility-hardening correction with POM close to the focal spot, is applied. As can be seen, this correction brings areas outside of the lung close to $D=1$ which is expected for these regions, as there is no scattering tissue present. However, there are still bones visible in the image as the two-fold correction discussed in section 4.6.5 could not be applied here. To allow for such a correction a segmentation of the bones would be required first.

5.5 Summary & Outlook

5.5.1 First in-vivo porcine XDF chest images

The very first in-vivo XDF chest images represent a breakthrough in the translation of XDF imaging to clinical applications. As neither simulations nor ex-vivo studies could prove that a translation of the technique from mice to humans is feasible, living pigs were used as the last intermediate step. The results presented address the major challenges of chest XDF imaging,

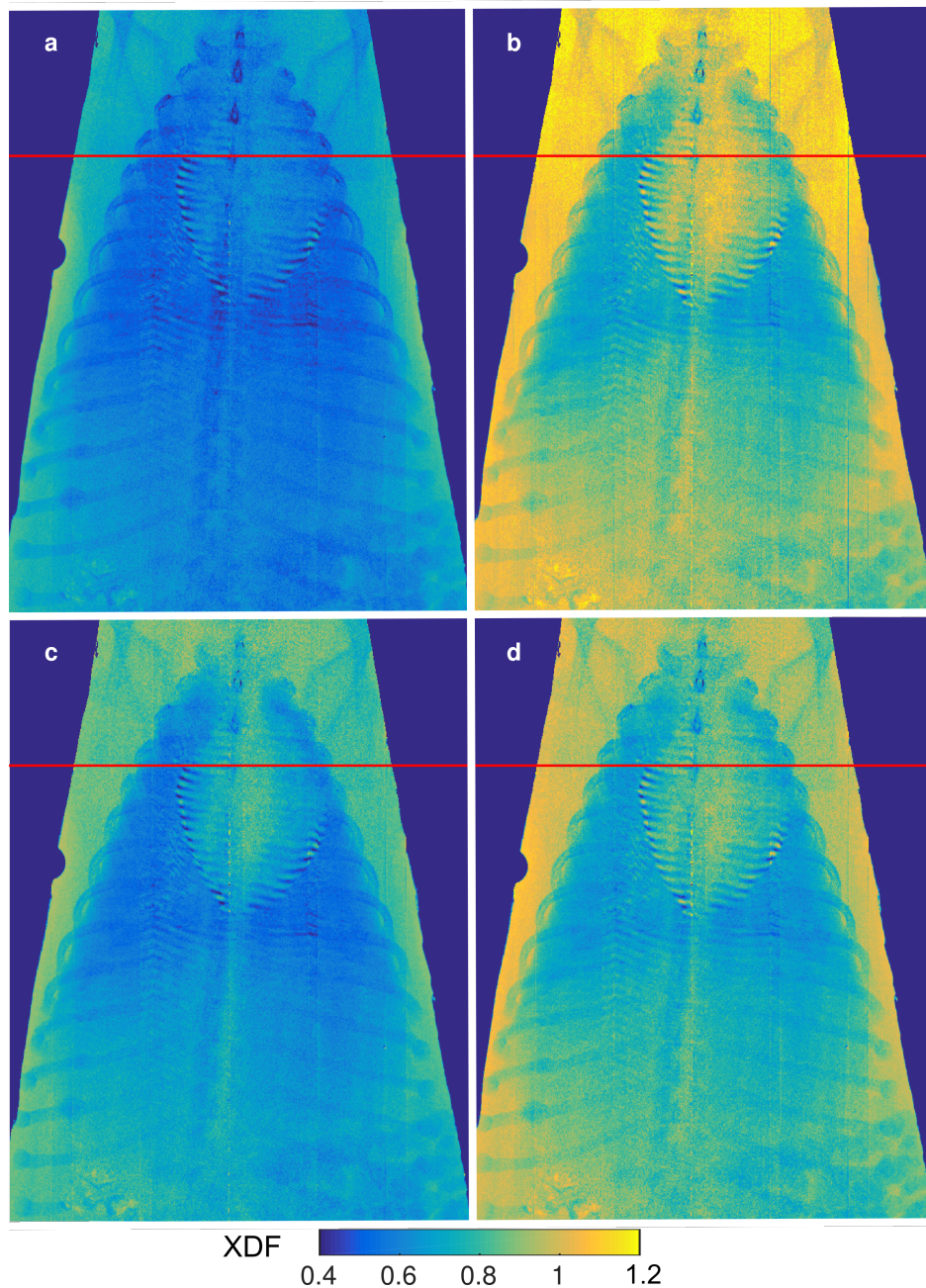


Figure 5.7 Different correction methods: (a) Uncorrected XDF image. (b) “Old” visibility-hardening correction with POM on table. This method results in overcorrection ($D > 1$) for heavy attenuating regions, as the influence of CS is overestimated. (c) Compton-scattering corrected XDF image obtained by the results from the Monte-Carlo simulation. (d) Additionally visibility-hardening corrected version of (c), with the POM calibration acquired close to the focal spot. The line profiles of the red lines are shown in Fig. 5.8. The scan was performed with 60 kVp and all images are given with a linear color map.

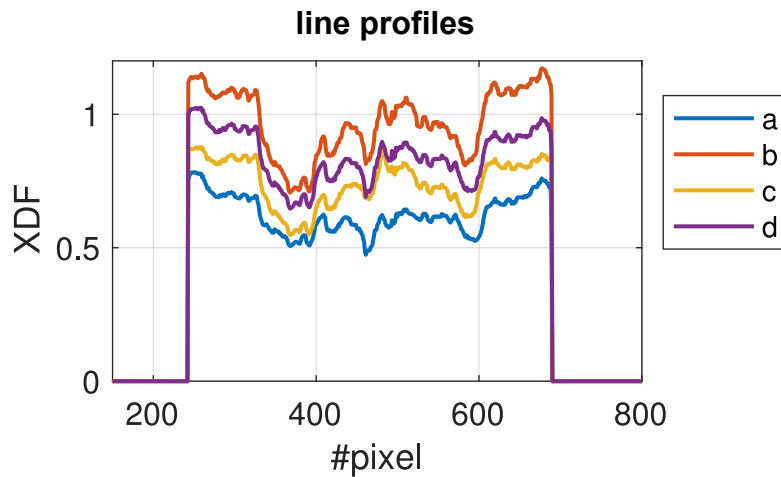


Figure 5.8 Line profiles of Fig. 5.7: (a) Uncorrected XDF image. (b) “Old” visibility-hardening correction with POM on table. (c) Compton-scattering corrected XDF image, by the results from the Monte-Carlo simulation. (d) Additionally visibility-hardening corrected version of (c), with the POM calibration acquired close to the focal spot.

namely: achieving a large FOV, high visibility at clinically compatible X-ray energies, a short acquisition time and a clinically acceptable radiation dose. The findings with the study of healthy pigs support the assumption that the XDF signal seen in the porcine lung originates from the same morphological structure, namely the air-tissue interfaces of the alveoli, as shown in various mice models. In the next step, follow-up studies are needed to quantify the diagnostic sensitivity and specificity of XDF imaging in further large animal models and/or clinical trials.

XDF chest imaging has the potential to close the diagnostic gap between microscopic but invasive histopathology and conventional macroscopic X-ray imaging. I believe that XDF imaging can be established as a functional imaging tool in clinical practice, soon. As lung diseases like COPD belong to the leading causes of mortality and morbidity in modern society[30], any improvements in establishing an early diagnosis for these diseases will benefit a large number of people.

5.5.2 Tube voltage optimization

Extending the work from chapter 4.3, it was also shown for a porcine thorax that the optimal tube voltage is around 60 kVp, as here the overall image quality as well as the quantitative SNR of the lung signal are best. However,

as all imaged animals had about the same weight and thorax dimensions, the next study should also include much thicker and thinner thoraxes, to estimate the optimal kVp also for those samples. Further, if gratings with smaller periods and higher absorber structures become available, this kVp maximum will most likely shift to higher energies.

5.5.3 Motion artifacts

First, it was shown that paused breathing is inevitable for XDF imaging. Second, it was shown that a proper alignment of the Moiré fringe pattern allows to reduce the heart beat artifacts to a tolerable level. Future improvements like cardiac gating and advanced processing might reduce these artifacts even further and should be evaluated in future projects.

5.5.4 Visibility-hardening and CS correction

In this experiment the advanced Compton-scattering and visibility-hardening correction methods from sections 4.5 and 4.6 were applied to a real measurement of a porcine thorax to increase the quantitative correctness of the XDF images. These methods were compared to the “old” approach where both Compton-scattering and visibility-hardening are corrected with a single calibration acquired from POM placed on the table.

It could be shown that the prediction of the Compton background via Monte Carlo simulations provides realistic results and that the overshooting of the XDF signal in heavily attenuating structures like the shoulders is prevented. However, as the registration of the CT dataset and the XDF measurement was not good enough to perform a segmentation of the bones, the two-fold visibility-hardening correction of the bones could not be applied. The image was therefore only visibility-hardening corrected for soft-tissue with POM, which results in remaining bone artifacts. Compared to the old “on table” method with a correction of solely POM, this approach with numerical CS simulation is much more trustworthy with respect to the quantitative numbers for the DXF signal. For future sample scans, an additional CT scan should therefore always be considered to allow for a retrospective simulation of the Compton-scattering contribution. A generic CS model of the scanner that allows for a fit of any measured sample to a pre-computed database would be even better.

Chapter 6

Advanced applications: drug screening in luggage

In the previous chapter the application of the developed XDF-scanner for lung imaging was presented and extensively discussed. However, this technology is not limited to biomedical applications. Therefore, another possible application of XDF imaging is presented in the following chapter: namely security screening. As the FOV of the developed scanner is large enough to handle full peaces of luggage at once, the feasibility of XDF contraband detection is evaluated next. Please note that the main results of this section are a part of a manuscript in preparation by Gromann et al. that will be submitted for publication soon. Figures and text passages in this section may appear similar or identically in the manuscript.

Contents

6.1	Motivation	121
6.2	Materials & Methods	122
6.3	Results	124
6.4	Discussion & Summary	127

6.1 Motivation

X-ray imaging is a frequently used tool in security inspection, e.g. in inspection of baggage at airports. It is mostly used in the form of dual-energy radiography to separate high Z materials (e.g. metals) from low Z materials (e.g. organics or plastics). Other X-ray techniques like CT imaging or coherent backscatter imaging are also possible but are seldom used in practice. X-ray (dual-energy) radiography is a powerful tool in the detection of suspi-

cious objects like metal weapons but is weak in the identification of organic contrabands in unsuspecting containers. These organic contrabands are often illegal drugs like cocaine and heroin[141]. The main problem in the detection of these powder-like drugs in conventional X-ray images is their similarity to harmless organic liquids (e.g. soap, shampoo and skin cream). In this chapter, it will be shown that XDF imaging may serve as a new tool to solve this security issue.

6.2 Materials & Methods

6.2.1 Drug phantom samples

Due to the fact that samples of real drugs (e.g. cocaine) were not available due to legal restrictions, samples of the two major adulterants commonly found in street-sold cocaine[142, 143] were used:

1. Lidocaine (SigmaAldrich©, Steinheim, Germany), a synthetic local anesthetic that is very similar to cocaine in its structural appearance and also numbs the gums when applied. It is therefore used to mimic the effect of cocaine on human mucosa (this “tongue test” is often used as a simple indicator for the quality of street sold cocaine). This adulterant might make up to 92% of the total mass of typical cocaine samples[143].
2. Lactose powder (dm©, Karlsruhe, Germany), a white powder sugar which is pharmaceutically inactive and only used to extend the volume of street sold cocaine.

As these two adulterants make up a significant amount of the mass of of street sold cocaine, they are a valid test phantom for a screening experiment. Additionally, their grain-size (which is the dominant factor for the strength of the XDF signal[57]) is structurally similar enough to cocaine to also serve as a valid phantom for pure cocaine.

For imaging, the two powders were hidden in unsuspecting containers (Falcon tubes and plastic bottles) which were then stored in typical luggage samples. Fig. 6.1 on the next page shows an example of an XDF and attenuation image of the falcon tube containers. As can be seen, only the powder-like substances are generating a scattering signal, whereas the liquid and the powders experience a similar attenuation signal and are therefore hardly differentiable in the attenuation image.

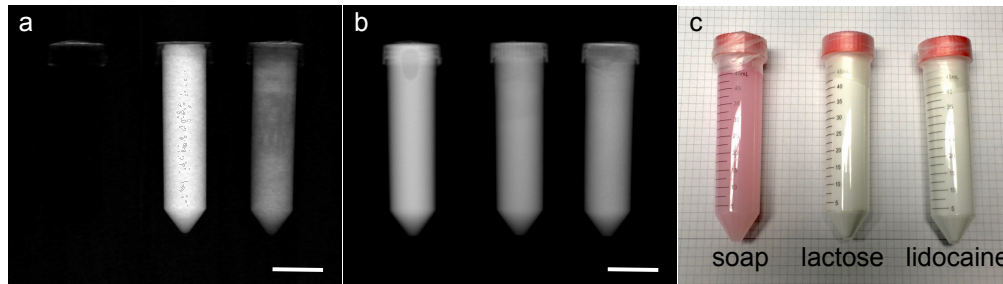


Figure 6.1 Multimodal X-ray radiograph of different substances. (a) XDF, (b) conventional attenuation and (c) photograph of three sealed falcon tubes filled with liquid soap, lactose and Lidocaine powder. As all three organic substances have a similar attenuation behavior, they all appear similar in the conventional attenuation image (b). In particular, it is impossible to differentiate between the harmless liquid soap and the powder-like potential contrabands. However, in the XDF image (a) only the two powders are visible, as the liquid does not scatter at all. And here, it is even possible to distinguish differently dense areas within the Lidocaine, which were caused by the tube filling process. The length scale is 3 cm and the images were acquired at 60 kVp with a 200 mA tube current.

6.2.2 Image fusion algorithm

To combine the scatter-based XDF image (D) with the attenuation-based image (A) into a single, fused image F, different approaches were suggested [144–147] which focused mostly on highlighting the differences in the imaging channels. Here, another very simple approach:

$$F = \log(D) \cdot \log(T) \quad (6.1)$$

is used which highlights features of the sample in pseudo color which are attenuating and scattering at the same time. However, also more sophisticated fusion algorithms may be applied in the future.

6.2.3 Tunable XDF sensitivity

The XDF signal D scales with

$$\log(D(E)) \propto \frac{1}{E^2} \cdot (G(E) - 1), \quad (6.2)$$

with the X-ray energy E and G(E) is the autocorrelation function of the sample [56–58, 65]. The autocorrelation function G(E) can be considered the “fingerprint” of a sample, incorporating the structural information of a

substance. This energy dependence (mostly the $1/E^2$ pre-factor) can further be used to tune the system to prevent signal saturation caused e.g. by thick layers of clothing. A higher tube voltage, also combined with pre-filtering to cancel out the lower energies of the X-ray beam, effectively reduces the XDF signal intensity.

6.3 Results

6.3.1 Real luggage sample

Fig. 6.2 shows the results of a leather backpack being imaged at 60 kVp with the XDF prototype scanner discussed in the previous chapters. In the conventional attenuation image (Fig. 6.2a), one can identify several bottles/containers inside the backpack which are slightly attenuating the X-rays (so most likely some organic content). However, no further evaluation of their content is possible. In contrast, only one of these containers generates a significant XDF signal (see Fig. 6.2b) which is further highlighted in the fused image (Fig. 6.2c). This suspicious container indeed contains the potential contraband Lidocaine, while the other containers just contain harmless liquids like skin cream and hand sanitizer. The photograph (Fig. 6.2d) shows a virtual overlay of the suspicious container over the backpack for illustration. This example shows that it is easily possible to identify powder-like contrabands in a real luggage example with this new method.

6.3.2 Adjusting the sensitivity with the X-ray energy

In order to visualize the energy dependency of the XDF signal, the samples shown in Fig. 6.1 were imaged again with different X-ray energies (kVp). Fig. 6.3 shows the averaged signal of the two regions of interest indicated by the blue and green box. As expected, the signal decreases with an increasing tube voltage. Please note that the curves are different for the two powders due to their different microstructures, or more precisely, their different auto-correlation functions. Although this behavior is not utilized here, it might be used to separate different powder types in the future (see discussion in section 6.4). Here, the energy dependence of the XDF signal is used exclusively to adjust the XDF sensitivity of the imaging system in order to prevent signal saturation from heavily scattering backgrounds like thick clothing. This is similar to the approach of increasing the X-ray energy to prevent signal saturation of heavily attenuating samples in conventional X-ray images. The application of an adjusted XDF sensitivity is shown in Fig. 6.4 for a

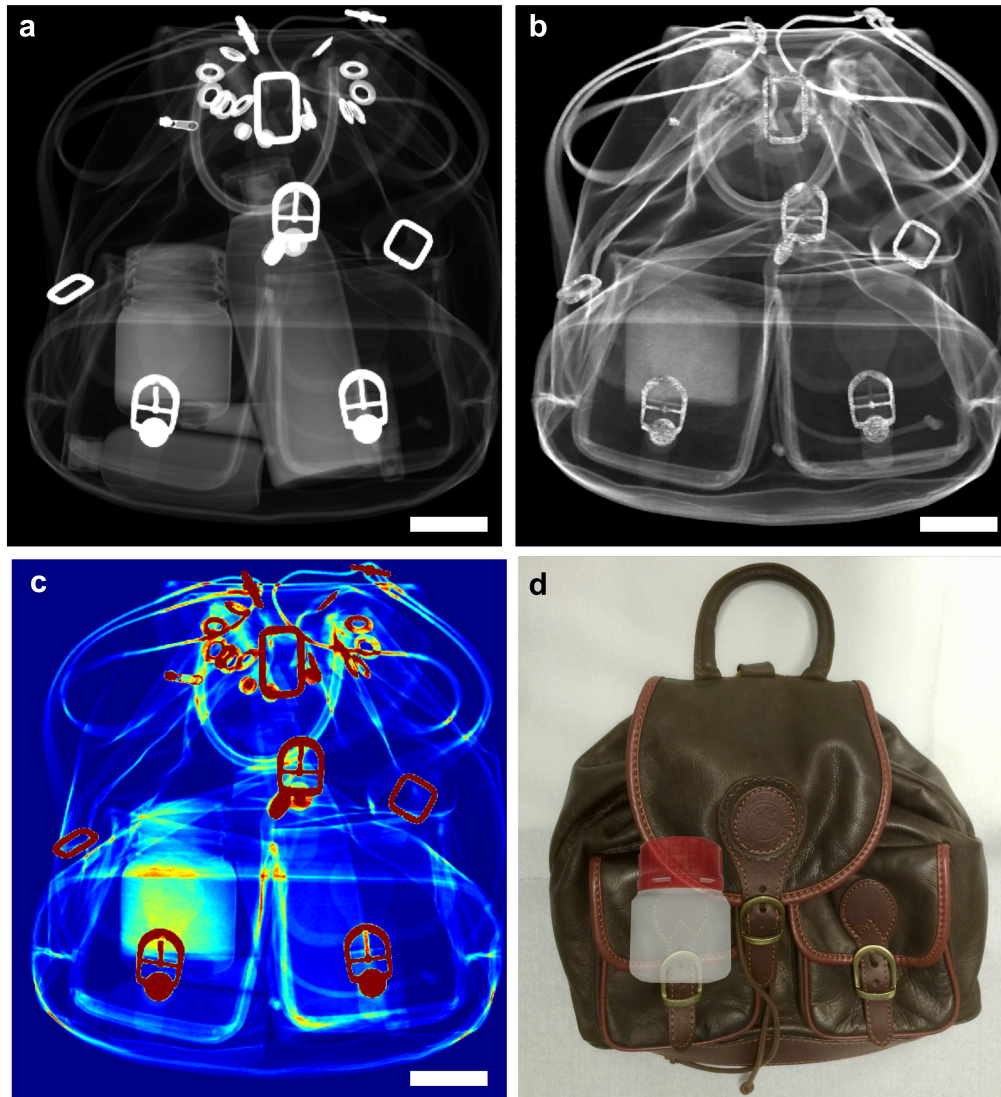


Figure 6.2 *Leather backpack with contraband phantom. (a) Conventional attenuation, (b) XDF and (c) fused image in pseudo color of a leather backpack and (d) photograph with a virtual overlay of the suspicious container. In the conventional attenuation image, it is impossible to discern the different organic contents of the various bottles. In contrast, in the XDF image, one bottle has a much higher XDF signal than the others. The fused image highlights this suspicious item even more which is indeed a plastic bottle filled with Lidocaine powder, a common cutting agent of cocaine. The other bottles contain harmless liquids like skin cream and sanitizer. The images were acquired with 60 kVp and the length scale in the images is 5 cm.*

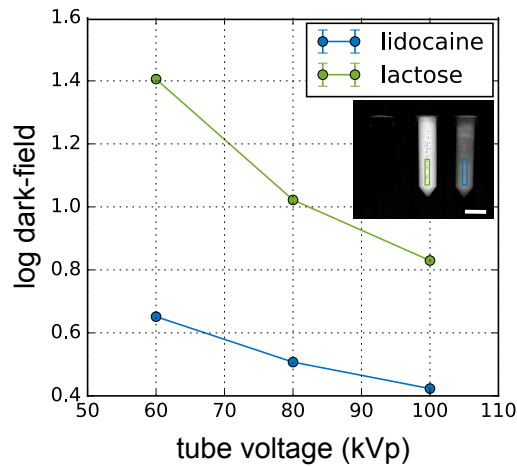


Figure 6.3 Tunable XDF sensitivity: Like the well-known energy dependency of attenuation images, the XDF signal is also highly energy dependent. By adjusting the energy of the X-ray spectrum, it is possible to adjust the signal intensity of scattering specimen to match the dynamic range of a given system. This can be used to prevent signal saturation of highly scattering samples like clothing. As an example, the figure shows the mean signal of the two powders - Lidocaine and lactose - over the green and blue ROI (from Fig. 6.1a). As expected, the signal declines with increasing X-ray energy, but the effect also depends on the microstructures of the samples (to be precise, on their autocorrelation functions (ACF)) and is therefore different for the two powders. In the future, the measurement of this ACF might be used to identify different types of powders.

second piece of sample luggage which is filled by more than 20 cm thick clothing. The attenuation image nicely shows two falcon tubes with similar attenuation properties which are hidden in the clothing. The suspicious container on the right side was filled with lactose powder and the harmless one on the left with liquid soap. However, in this case, the fibrous structure of the clothing also generates a significant XDF signal, up to the point where the scattering sample can no longer be distinguished from the background. In order to prevent this, the bag was scanned again with adjusted imaging parameters. The first scan was done with a 60 kVp spectrum while the second scan was performed at 80 kVp with an additional pre-filter made of 5 mm aluminum. As can be seen (white marker in Fig. 6.4b), the saturation is now prevented and the suspicious container can be identified again in the XDF image with an increase in the contrast-to-noise ratio (CNR) of more than a factor of 5 ($CNR_{60}^D = 0.2$ vs. $CNR_{80}^D = 1.1$ for the ROI's indicated in Fig. 6.4c). In order to enable a proper comparison, the imaging parameters were adjusted to keep the CNR in the attenuation image almost constant

($CNR_{60}^T = 6.1$ vs. $CNR_{80}^T = 6.3$) with a tube current of $I_{60} = 200$ mA and $I_{80} = 70$ mA, respectively.

6.4 Discussion & Summary

In this experiment, it was shown that the technology of X-ray XDF imaging is now mature enough to be implemented in a realistic luggage screening system. It was easily possible to detect powder-like contrabands hidden in commonly used containers that would have been missed with conventional attenuation imaging. A major concern with X-ray XDF imaging for luggage inspection was the problem of signal saturation due to large amounts of scattering clothing on top of the suspicious object. Therefore, it was shown that tuning the XDF sensitivity by adjusting the X-ray spectrum is feasible but may require a second scan of the sample if the first one experienced signal saturation. Since the radiation dose is not critical in luggage inspection, this may only require a little more scan time. In addition, the suspicious object can (and should) be removed from the luggage and scanned separately from the clothing. This would be similar to the standard operating procedure currently used by airport security for liquids in hand luggage. When a suspicious object is found and separated from the background, a measurement of the autocorrelation function of the sample would give the unique “fingerprint” of the material and would allow for a non-destructive identification of the sample (container does not need to be opened) by comparing the information with a previously acquired database. This measurement could either be performed by a variation of the energy (or energy-resolved measurement), a variation of the sample-to-grating distance or by measurement with an additional set of gratings. The latter in particular would be very suitable for a slot-scanning device, as the additional gratings could simply be placed next to the first one (in the scanning direction).

Here, the focus was exclusively on powder-like contrabands such as cocaine and heroin which occur frequently in smuggling due to their high resale prices. However, other publications[12, 148] also suggested that more threatening items like explosives also have a strong XDF signature due to their inherent microstructure. In the future, this should also be tested with the new scanner. Currently, the FOV of the scanner is only large enough to scan smaller bags that are the size of typical hand luggage. However, there is no longer a strict limitation on the FOV, as the stitching of additional grating tiles would be no longer a problem. Therefore, scanners for larger samples like suitcases would also be possible.

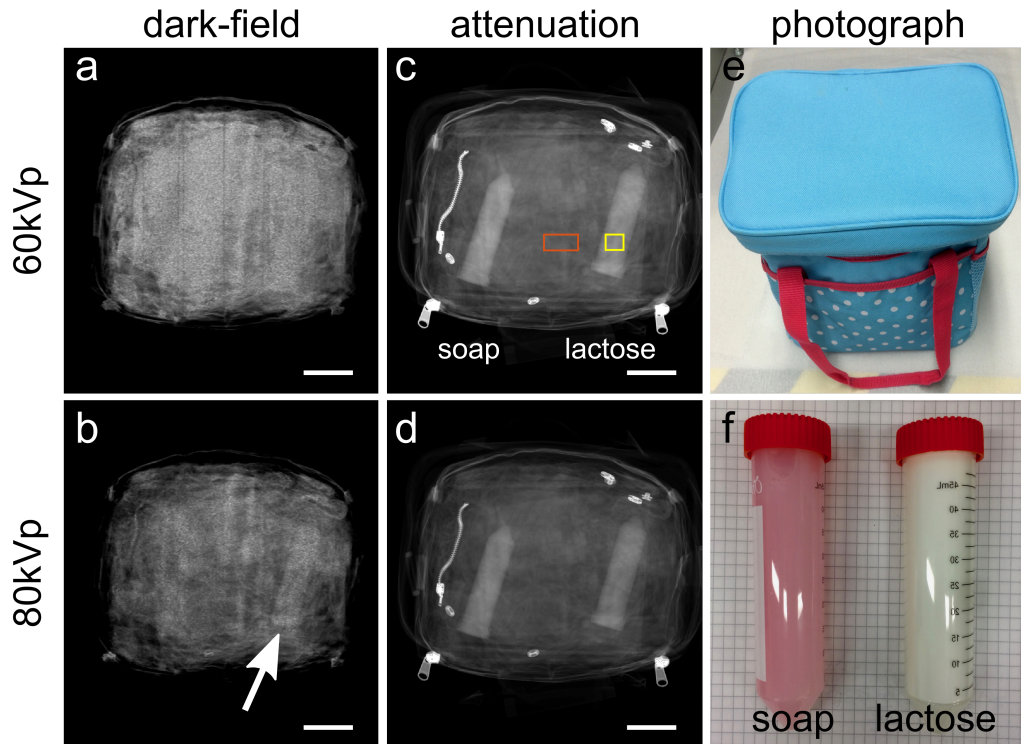


Figure 6.4 Adjusting the XDF sensitivity. XDF (a, b) and conventional attenuation images (c, d) of a bag (e) filled with about 20 cm of clothing (three t-shirts, a pair of shorts and a hoody). Additionally, two falcon tubes (f), one filled with lactose powder the other filled with liquid soap, were placed in the bag. Due to the fact that saturation of the XDF signal by such thick clothing samples may be a problem, the bag was imaged once with a lower voltage of 60 kVp (top row) and then with an increased voltage of 80 kVp and an additional pre-filter of 5 mm Al (bottom row). At the lower energy, the XDF saturates and the powder filled container cannot be distinguished from the background ($CNR_{60}^D = 0.2$ between orange and yellow ROI). Please note that the ROIs are identical for all four images. In contrast, at the higher energy and thus lower XDF sensitivity, the container with the suspicious powder is visible again (white arrow, with a $CNR_{80}^D = 1.1$). The imaging parameters were chosen in a way to keep the CNR in the attenuation image almost constant ($CNR_{60}^T = 6.1$ vs. $CNR_{80}^T = 6.3$) with a tube current of $I_{60} = 200$ mA and $I_{80} = 70$ mA.

Chapter 7

Summary, Discussion & Outlook

In this chapter, the main results of the work performed in the context of this PhD thesis are briefly summarized with the focus to reveal future research directions (sections 7.1-7.3). For a detailed discussion of the results, the reader is referred to the corresponding sections of the main manuscript. In section 7.4, the achievements of this thesis are discussed in context to other research in the field.

Contents

7.1	Design of the large-animal XDF-scanner	129
7.2	Characterization of the scanner	130
7.3	Applications:	132
7.4	Discussion with other research in the field . . .	134
7.5	Final conclusions	135

7.1 Design of the large-animal XDF-scanner

In chapter 3, the boundary conditions for the development of a large-animal XDF-scanner were discussed with the focus on solutions for the dominating challenges that prevented a translation of XDF imaging from small animals to human-sized animals:

- The large FOV was achieved by combining linear stitched gratings with a resulting size of about $2.5 \times 40 \text{ cm}^2$ with a slot-scanning approach. Further, the gratings are not moved linearly but on an arc to prevent parallax errors in the images. This enabled a total FOV of $32 \times 35 \text{ cm}^2$. To allow for a smooth motion of the grating slot, a backlash free mo-

torization concept was developed, which is coupled via a steel-rope to the gratings to suppress vibrations.

- To achieve a high visibility at clinically relevant energies of above 60 kVp all three gratings were optimized by using wave-optical simulations. The simulations revealed that three attenuation gratings will perform best in the anticipated geometry. This is a different approach compared to “classical” Talbot-Lau interferometers, which are based on a phase grating and interferometric effects.
- Acquisition of the imaging data is performed in a Moiré fringe scanning approach. As both the intensity and visibility differ across the grating, an additional phase stepping is performed during the flat field acquisition to obtain a reference intensity, phase and visibility for all relative coordinates within the grating slot.

Further research should focus on the optimization of advanced phase gratings with shapes different from a binary mask. As already indicated in the corresponding section, a triangular shaped grating might perform equally to a binary attenuation grating with the advantage of saving half of the dose. Additionally, a larger grating area would allow for even larger FOV and more importantly for much faster image acquisition. Nevertheless, this would require bent gratings whose fabrication also needs further investment.

7.2 Characterization of the scanner

In chapter 4 of the thesis, the performance of the developed scanner was evaluated in detail:

- The achievable visibility was measured energy-resolved and showed excellent agreement with the wave-optical simulations. The resulting visibility is about 31 % for a tube voltage of 70 kVp which is a very high value for a grating based imaging system. However, due to the finite height of the gold gratings, there is still a strong dependence of the visibility on the actual X-ray spectrum. With systematic measurements of a test phantom, the optimal tube voltage was estimated to be around 60- 70kVp for an XDF image of a realistic thorax. Lower tube voltages might even be better, however are hindered by the limited output power of the tube at these energies.
- This energy dependence of the visibility results also in strong XDF artifacts due to visibility-hardening effects. A correction of this effects

via calibration measurements with equivalent absorbers made of POM is therefore presented in the corresponding section. Additionally, a two-fold correction method is introduced which is able to correct for the remaining bone artifacts. These artifacts are a result of the under-correction of the visibility-hardening caused by bones solely with POM. However, this method requires a pixel-wise segmentation of the image into at least two materials (e.g. soft-tissue and bones). In this thesis, only a single prove-of-concept of the method based on simulations could be presented. Further research is therefore necessary to evaluate the segmentation in a realistic imaging experiments, e.g. based on a dual-energy decomposition or digital image processing.

- Another source of pseudo XDF signal is Compton-scattering. This pseudo signal is especially high behind heavily attenuating features like bones or thick parts of soft-tissue. Monte Carlo simulations showed that the current geometry (2.5 cm slot-width and three attenuation gratings) offers an optimized scattering suppression. However, even here a pseudo XDF signal of up to 10 % in the lung is expected for human like samples and up to 5 % for porcine samples. Other geometries with less attenuation gratings or without the slot perform even worse. However, these results are only based on a quantity of $n=1$ for both the human and the porcine chest phantoms. Further simulation studies are needed to evaluate the influence of e.g. differences in body weight and shape more precisely.
- To correct for the Compton pseudo signal, a correction method based on a Monte Carlo simulation was introduced. Here, a simulation of the expected Compton background for the individual sample is performed. With this information, the original XDF image can then be corrected. However, this simulation requires a registered 3D model of the imaged sample. Such a model can be generated from a corresponding CT of the sample (as done here), but is not available on a general basis. A better approach would be the fitting of the sample data to generic, pre-computed scatter-data. Further research should therefore be applied on the implementation of the X-ray gratings in currently available Compton-scattering calculation software packages (e.g. Philips Skyflow).
- The achievable image resolution in the attenuation images was measured according to the guideline applicable for conventional thorax imaging. The maximum resolution which could be achieved is about 1 lp/mm. This is a rather low value compared to conventional chest

X-ray systems however is inevitable due to the high detector binning necessary for the fast read-out-speed. Higher resolutions would require a faster detector. With the current hardware, a minimum scan time of about 40 sec can be realized. Additionally, faster image speeds introduce vibration artifacts and would therefore require a better motor as well.

7.3 Applications:

7.3.1 Porcine chest imaging

First in-vivo images The results in chapter 5 represent a breakthrough in the translation of XDF imaging to clinical applications:

- The prove-of-principle results of the very first in-vivo image of a porcine thorax overcame the major challenges so far related to chest XDF imaging: achieving a large FOV, high visibility at clinically compatible X-ray energies, a short acquisition time and a clinically acceptable radiation dose.
- The findings with the study of healthy pigs support the assumption that the XDF signal seen in the pig lung originates from the same morphological structure as in the mice, namely: the air-tissue interfaces of the alveoli. It is therefore justified to predict a similar behavior also for human lungs.
- Further studies should also include pathology models in pigs, to evaluate the improved diagnostic performance of the scanner. However, lung pathologies are not easily induced in pigs and from an animal welfare point of view it might be problematic to argue for such painful experiments (particularly for disease models that include a long incubation time without narcotics). Especially, as the data are already quite convincing to directly continue with first human experiments.

Tube voltage optimization Continuing the tube voltage optimization performed for the technical phantom above, this section evaluated the optimal tube voltage on a real thorax sample:

- Also for a porcine thorax it was shown, that the optimal tube voltage is around 60 kVp, as here the overall image quality as well as the quantitative SNR of the lung region was best. Future research should include pigs with different body weights and dimensions, as for much

thicker thoraces this optimum might be shifted to higher energies. The same might happen, if gratings with smaller periods and/or higher gold structures become available.

Heart beat motion Heart beat motion was considered as a major challenge in in-vivo XDF chest imaging. In this section the influence of the shape of the Moiré pattern on motions artifacts was therefore studied:

- It was found, that a proper alignment of the Moiré fringe pattern allows for in-vivo imaging, even with a beating heart. The resulting artifacts are then mostly restricted to the heart-lung boundary and do not affect overall diagnostic quality of the images. Nevertheless, future studies should invest improved image reconstruction algorithms that might incorporate cardiac gating and other advanced processing features, to further reduce these artifacts.

Visibility-hardening and CS correction As a prove-of-concept, the visibility-hardening and Compton-scattering correction methods introduced above, were applied to a real porcine thorax image:

- The application of both the Compton-scattering correction as well as the visibility-hardening correction to a porcine thorax image revealed a significant improvement of the quantitative XDF signal. This is especially the case for thick structures like the abdomen or the shoulders. However, only the simple correction based on POM could be performed here as a pixel-wise segmentation of the image in soft-tissue and bones was not available, resulting in remaining bone artifacts. As already discussed above, this should be done in future research e.g. based on a dual energy decomposition. Additionally, further research should be applied to characterize the amount of “real” XDF scattering of the bones due to their trabecular micro structure[99, 149, 150].

7.3.2 Drug screening

In this chapter it was shown that the developed scanner is also suitable as a security scanner with a focus on powder-like contrabands:

- In several realistic luggage examples it was easily possible to detect powder-like contrabands hidden in commonly used containers which would have been missed with conventional attenuation imaging. In conventional imaging it is impossible to distinguish an organic liquid from an organic powder. Nevertheless, as no real cocaine could be used

due to legal restrictions, the experiment should be repeated with real cocaine, as soon as the authorities approve the experiments.

- Saturation of the XDF signal by heavily scattering clothing inside of the suitcase could be prevented by increasing the X-ray energy and therefore decreasing the XDF sensitivity of the system.
- Separation of the suspicious container from any scattering background (as already done for liquid containers in hand luggage screening at most airports) would also allow for a (rough) measurement of the autocorrelation function of the substance either by an energy-resolving detector or by a measurement with different grating sets. This might even enable a differentiation of different types of powders.
- The system should in future also be tested for detection of other threatening items like explosives which are reported to have also an XDF active microstructure.

7.4 Discussion with other research in the field

Quite recently, also other groups from the field of X-ray dark-field and phase-contrast imaging published interesting research articles where they try to increase the field-of-view and X-ray energy of their imaging systems. However none of them were yet able to increase the performance of their systems enough to allow for in-vivo imaging of thick samples. As an overview some of the most important groups in the field and their individual approaches are discussed in the following and compared to the prototype developed for this thesis.

Group of Prof. Alessandro Olivo (University College London, UK):

Their approach of using coded apertures is from a physical point of view very similar to the idea of using three achromatic attenuation gratings for the G1 grating, as done in this thesis. However the data processing is very different and their method requires the detector mask to be aligned to the detector pixels as well. Very recently they also published a new, dose effective imaging system based on a slot scanning approach[55] which shows some promising results. However this system is still inferior to the prototype developed in this thesis as they can only scan very thin samples for two reasons: First, they apply a linear sample motion and cannot correct for parallax errors.

Second, as they do not use a G0 they require a micro-focus tube that does not allow for the large flux, necessary for imaging of thick samples. Finally, their scanning movement is still four times slower.

Group of Prof. Gisela Anton (Friedrich-Alexander-University Erlangen-Nuremberg, Germany): The group of Prof. Anton recently developed a new concept to use phase-gratings with duty cycles different from the conventional $dc=0.5$ [151]. With this approach a third possibility (besides using attenuation gratings or trapezoidal phase gratings for the G1 as already discussed in this thesis) is introduced that allows to reduce the system length for high-energy applications. They successfully applied this idea to an imaging experiment of a human knee[99]. Although, this new system seems to be quite dose effective, it's FOV is still very small and requires multiple movements of the sample in a checkerboard-like manner and digital stitching of the images.

Group of Prof. Atsushi Momose (The University of Tokyo, Japan): As discussed in section 3.5 on page 59, the fringe scanning approach proposed by Kottler et al, needs to be modified to account for differences in intensity and visibility across the grating. Bachche et al.[106] recently published another algorithm to solve this problem. Their introduced prototype-system allows for a nice slot scanning, however is again not suitable for thick samples due to parallax errors.

CSEM SA (Switzerland): One of the first proof-of-concepts for a imaging system with high-quality large 2D-stitched gratings was presented by a research-group from CSCM in Switzerland[102]. They were able to fabricate $20 \times 20 \text{ cm}^2$ large silicon gratings from stitching 2×2 grating tiles. This is a promising result for future applications of systems with full-field gratings.

7.5 Final conclusions

The main goal of this thesis, namely the development of an XDF-scanner for lung imaging was successfully reached and the whole project was successfully completed by the acquisition of the very first in-vivo XDF porcine chest images. Finally, the results of this thesis open the way for other XDF imaging applications that require large objects to be scanned in a relatively short time. This could include other medical applications such as foreign body detection, improved osteoporosis fracture risk assessment and novel XDF micro-bubble

contrast agents, as well as non-medical fields like airport security and material or food science.

Chapter 8

Appendix

Publications and scientific presentations

First-authored publications (peer-reviewed)

L. B. Gromann, D. Bequé, K. Scherer, K. Willer, L. Birnbacher, M. Willner, J. Herzen, S. Grandl, K. Hellerhoff, J. I. Sperl, F. Pfeiffer, and C. Cozzini, “Low-dose, phase-contrast mammography with high signal-to-noise ratio,” *Biomed. Opt. Express*, vol. 7, no. 2, pp. 381–391, 2016.

L. B. Gromann, F. De Marco, K. Willer, P. B. Noël, K. Scherer, B. Renger, B. Gleich, K. Achterhold, A. A. Fingerle, D. Muenzel, S. Auweter, K. Hellbach, M. Reiser, A. Baehr, M. Dmochewitz, T. J. Schroeter, F. J. Koch, P. Meyer, D. Kunka, J. Mohr, A. Yaroshenko, H.-I. Maack, T. Pralow, H. van der Heijden, R. Proksa, T. Koehler, N. Wieberneit, K. Rindt, E. J. Rummeny, F. Pfeiffer, and J. Herzen, “In-vivo X-ray Dark-Field Chest Radiography of a Pig,” *Nature Scientific Reports*, vol. 7, no. 1, p. 4807, 2017.

L. B. Gromann, et al., “Contraband detection with X-ray dark-field imaging”, prepared for submission in *NDT&E international*.

Co-authored publications (peer-reviewed)

K. Scherer, K. Willer, **L. B. Gromann**, L. Birnbacher, E. Braig, S. Grandl, A. Sztrkay-Gaul, J. Herzen, D. Mayr, K. Hellerhoff, and F. Pfeiffer, “Toward Clinically Compatible Phase-Contrast Mammography,” *PLoS One*, vol. 10, no. 6, p. e0130776, 2015.

A. Yaroshenko, T. Pritzke, M. Koschlig, N. Kamgari, K. Willer, **L. Gromann**, S. Auweter, K. Hellbach, M. Reiser, O. Eickelberg, F. Pfeiffer, and A. Hilgendorff, “Visualization of neonatal lung injury associated with

mechanical ventilation using x-ray dark-field radiography,” *Nature Scientific Reports*, vol. 6, no. 1, p. 24269, 2016.

T. J. Schröter, F. J. Koch, P. Meyer, D. Kunka, J. Meiser, K. Willer, **L. B. Gromann**, F. De Marco, J. Herzen, P. Noel, A. Yaroshenko, A. Hofmann, F. Pfeiffer, and J. Mohr, “Large field-of-view tiled grating structures for X-ray phase-contrast imaging,” *Rev. Sci. Instrum.*, vol. 88, no. 1, p. 15104, 2017.

K. Scherer, A. Yaroshenko, D. A. Bölükbas, **L. B. Gromann**, K. Hellbach, F. G. Meinel, M. Braunagel, J. von Berg, O. Eickelberg, M. F. Reiser, F. Pfeiffer, S. Meiners, and J. Herzen, “X-ray Dark-field Radiography - In-Vivo Diagnosis of Lung Cancer in Mice,” *Nature Scientific Reports*, vol. 7, no. 1, p. 402, 2017.

E. Braig, L. Birnbacher, F. Schaff, **L. B. Gromann**, A. A. Fingerle, J. Herzen, E. J. Rummeny, P. B. Noel, F. Pfeiffer and D. Münzel, “Simultaneous wood and metal particle detection on dark-field radiography”, *European Radiology Experimental*, 2017.

K. Hellbach, A. Bähr, F. De Marco, K. Willer, **L. B. Gromann**, J. Herzen, M. Dmochewitz, S. Auweter, A. A. Fingerle, P. B. Noël, E. J. Rummeny, A. Yaroshenko, I. Maack, T. Pralow, H. van der Heijden, N. Wieberneit, R. Proksa, T. Koehler, K. Rindt, T. J. Schroeter, J. Mohr, F. Bamberg, B. Ertl-Wagner, F. Pfeiffer, M. F. Reiser, “Depiction of pneumothoraces in a large animal model using x-ray dark-field radiography”, under review in *Nature Scientific Reports*, 2017.

K. Willer, A. A. Fingerle, **L. B. Gromann**, F. De Marco, J. Herzen, K. Achterhold, B. Gleich, D. Muenzel, K. Scherer, M. Renz, B. Renger, F. Kopp, F. Kriner, F. Fischer, C. Braun, S. Auweter, K. Hellbach, M. Reiser, T. Schroeter, J. Mohr, A. Yaroshenko, I. Maack, T. Pralow, H. van der Heijden, R. Proksa, T. Koehler, N. Wieberneit, K. Rindt, E. Rummeny, F. Pfeiffer and P. B. Noel, “X-ray dark-field imaging of the human lung”, under review in *Nature Scientific Reports*, 2017.

First-authored conference proceedings

L. B. Gromann, K. Scherer, A. Yaroshenko, D. A. Bölükbas, K. Hellbach, F. G. Meinel, M. Braunagel, O. Eickelberg, M. F. Reiser, F. Pfeiffer, S. Meiners, and J. Herzen, “First experiences with in-vivo X-ray dark-field imaging of lung cancer in mice,” *SPIE Proceedings Medical Imaging 2017*, vol. 10132, p. 101325L.

Oral presentations

Title: First in-vivo X-ray dark-field chest radiography: A feasibility study in living pigs and phantom samples, *International Symposium on BioMedical Applications of X-Ray Phase Contrast Imaging IMXP*, Garmisch-Partenkirchen, Germany, January 2017

Poster presentations

Title: High Talbot order grating-based phase-contrast mammography, *International Symposium on BioMedical Applications of X-Ray Phase Contrast Imaging IMXP*, Garmisch-Partenkirchen, Germany, January 2015

Title: X-ray Dark-Field Imaging of Pulmonary Carcinoma, *KNMF User Meeting*, Karlsruhe, Germany, 2016

Title: In-vivo X-ray Dark-Field Imaging of Lung Cancer in Mice, *SPIE Medical Imaging*, Orlando, USA, February 2017

Bibliography

- [1] W. C. Röntgen, “Über eine neue Art von Strahlen,” *Annalen der Physik*, 1898.
- [2] K. Lawniczak-Jablonska and J. Cutler, “X-ray techniques for innovation in industry,” *IUCrJ*, 2014.
- [3] A. Momose, “Recent Advances in X-ray Phase Imaging,” *Japanese Journal of Applied Physics*, vol. 44, no. 9A, pp. 6355–6367, 2005.
- [4] T. J. Vogl, W. Reith, and E. J. Rummeny, *Diagnostische und interventionelle Radiologie*. Berlin Heidelberg New York Bibliografische: Springer-Verlag Berlin Heidelberg, 2011, vol. 1.
- [5] A. Snigirev, I. Snigireva, V. Kohn, S. Kuznetsov, and I. Schelokov, “On the possibilities of x-ray phase contrast microimaging by coherent high-energy synchrotron radiation,” *Review of Scientific Instruments*, vol. 66, no. 12, pp. 5486–5492, 1995.
- [6] P. Cloetens, W. Ludwig, J. Baruchel, D. Van Dyck, J. Van Landuyt, J. P. Guigay, and M. Schlenker, “Holotomography: Quantitative phase tomography with micrometer resolution using hard synchrotron radiation x rays,” *Applied Physics Letters*, vol. 75, no. 19, p. 2912, 1999.
- [7] T. J. Davis, D. Gao, T. E. Gureyev, A. W. Stevenson, and S. W. Wilkins, “Phase-contrast imaging of weakly absorbing materials using hard X-rays,” pp. 595–598, 1995.
- [8] D. Chapman, W. Thomlinson, R. E. Johnston, D. Washburn, E. Pisano, N. Gmür, Z. Zhong, R. Menk, F. Arfelli, and D. Sayers, “Diffraction enhanced x-ray imaging,” *Physics in medicine and biology*, vol. 42, no. 11, pp. 2015–25, 1997.
- [9] U. Bonse and M. Hart, “An X-ray interferometer,” *Applied Physics Letters*, 1965.

- [10] A. Momose, S. Kawamoto, I. Koyama, Y. Hamaishi, K. Takai, and Y. Suzuki, "Demonstration of x-ray Talbot interferometry," *Japanese Journal of Applied Physics, Part 2: Letters*, vol. 42, no. 7 B, 2003.
- [11] F. Pfeiffer, T. Weitkamp, O. Bunk, and C. David, "Phase retrieval and differential phase-contrast imaging with low-brilliance X-ray sources," *Nature Physics*, vol. 2, no. 4, pp. 258–261, 2006.
- [12] F. Pfeiffer, M. Bech, O. Bunk, P. Kraft, E. F. Eikenberry, C. Bronnimann, C. Grunzweig, and C. David, "Hard-X-ray dark-field imaging using a grating interferometer," *Nature Materials*, vol. 7, no. 2, pp. 134–137, feb 2008.
- [13] A. Tapfer, M. Bech, B. Pauwels, X. Liu, P. Bruyndonckx, A. Sasov, J. Kenntner, J. Mohr, M. Walter, J. Schulz, and F. Pfeiffer, "Development of a prototype gantry system for preclinical x-ray phase-contrast computed tomography," *Med Phys.*, no. 0094-2405 (Print), 2011.
- [14] A. Velroyen, A. Yaroshenko, D. Hahn, A. Fehringer, A. Tapfer, M. Muller, P. B. Noel, B. Pauwels, A. Sasov, A. O. Yildirim, O. Eickelberg, K. Hellbach, S. D. Auweter, F. G. Meinel, M. F. Reiser, M. Bech, and F. Pfeiffer, "Grating-based X-ray Dark-field Computed Tomography of Living Mice," *EbioMedicine*, no. 2352-3964 (Electronic), 2015.
- [15] B. für Stahlschutz, "Röntgendiagnostik: Häufigkeit und Strahlenexposition," 2014. [Online]. Available: <https://www.bfs.de/DE/themen/ion/anwendung-medizin/diagnostik/roentgen/haeufigkeit-exposition.html>
- [16] H. Wen, E. E. Bennett, M. M. Hegedus, and S. Rapacchi, "Fourier X-ray scattering radiography yields bone structural information." *Radiology*, vol. 251, no. 3, pp. 910–918, 2009.
- [17] M. Stampanoni, Z. Wang, T. Thüring, C. David, E. Roessl, M. Trippel, R. A. Kubik-Huch, G. Singer, M. K. Hohl, and N. Hauser, "The First Analysis and Clinical Evaluation of Native Breast Tissue Using Differential Phase-Contrast Mammography," *Investigative Radiology*, vol. 46, no. 12, pp. 801–806, 2011.
- [18] S. Schleede, F. G. Meinel, M. Bech, J. Herzen, K. Achterhold, G. Potdevin, A. Malecki, S. Adam-Neumair, S. F. Thieme, F. Bamberg, K. Nikolaou, A. Bohla, A. Ö. Yildirim, R. Loewen, M. Gifford, R. Ruth, O. Eickelberg, M. F. Reiser, and F. Pfeiffer, "Emphysema diagnosis

- using X-ray dark-field imaging at a laser-driven compact synchrotron light source.” *Proceedings of the National Academy of Sciences of the United States of America*, vol. 109, no. 44, pp. 17880–5, oct 2012.
- [19] G. Potdevin, A. Malecki, T. Biernath, M. Bech, T. H. Jensen, R. Feidenhans'l, I. Zanette, T. Weitkamp, J. Kenntner, J. Mohr, P. Roschger, M. Kerschnitzki, W. Wagermaier, K. Klaushofer, P. Fratzl, and F. Pfeiffer, “X-ray vector radiography for bone micro-architecture diagnostics,” *Physics in Medicine and Biology*, vol. 57, no. 11, pp. 3451–3461, 2012.
- [20] A. Tapfer, R. Braren, M. Bech, M. Willner, I. Zanette, T. Weitkamp, M. Trajkovic-Arsic, J. T. Siveke, M. Settles, M. Aichler, A. Walch, and F. Pfeiffer, “X-Ray Phase-Contrast CT of a Pancreatic Ductal Adenocarcinoma Mouse Model,” *PLoS ONE*, vol. 8, no. 3, 2013.
- [21] F. Horn, C. Hauke, S. Lachner, V. Ludwig, G. Pelzer, J. Rieger, M. Schuster, M. Seifert, J. Wandner, A. Wolf, T. Michel, and G. Anton, “High-energy x-ray grating-based phase-contrast radiography of human anatomy,” in *Proc. SPIE 9783, Medical Imaging 2016: Physics of Medical Imaging*, vol. 97830, 2016, pp. 97 830P–97 830P.
- [22] A. Yaroshenko, F. G. Meinel, M. Bech, A. Tapfer, A. Velroyen, S. Schleede, S. Auweter, A. Bohla, A. Ö. Yildirim, K. Nikolaou, F. Bamberg, O. Eickelberg, M. F. Reiser, and F. Pfeiffer, “Pulmonary Emphysema Diagnosis with a Preclinical Small-Animal X-ray Dark-Field Scatter-Contrast Scanner,” *Radiology*, vol. 269, no. 2, pp. 427–433, 2013.
- [23] A. Yaroshenko, F. G. Meinel, M. Bech, A. Tapfer, A. Velroyen, S. Schleede, M. Muller, S. Auweter, A. Bohla, A. O. Yildirim, K. Nikolaou, F. Bamberg, O. Eickelberg, M. F. Reiser, and F. Pfeiffer, “Pre-clinical x-ray dark-field radiography for pulmonary emphysema evaluation,” in *Proceedings - International Symposium on Biomedical Imaging*, 2013, pp. 370–373.
- [24] F. G. Meinel, A. Yaroshenko, K. Hellbach, M. Bech, M. Müller, A. Velroyen, F. Bamberg, O. Eickelberg, K. Nikolaou, M. F. Reiser, F. Pfeiffer, and A. Ö. Yildirim, “Improved Diagnosis of Pulmonary Emphysema Using In Vivo Dark-Field Radiography,” *Investigative Radiology*, vol. 00, no. 00, pp. 1–6, 2014.

- [25] A. Yaroshenko, K. Hellbach, A. Ö. Yildirim, T. M. Conlon, I. E. Fernandez, M. Bech, A. Velroyen, F. G. Meinel, S. Auweter, M. F. Reiser, O. Eickelberg, and F. Pfeiffer, “Improved In vivo Assessment of Pulmonary Fibrosis in Mice using X-Ray Dark-Field Radiography,” *Scientific Reports*, vol. 5, p. 17492, 2015.
- [26] K. Hellbach, A. Yaroshenko, F. G. Meinel, A. Ö. O. Yildirim, T. M. Conlon, M. Bech, M. Mueller, A. Velroyen, M. Notohamiprodjo, F. Bamberg, S. Auweter, M. F. Reiser, O. Eickelberg, and F. Pfeiffer, “In Vivo Dark-Field Radiography for Early Diagnosis and Staging of Pulmonary Emphysema,” *Investigative Radiology*, vol. 50, no. 7, pp. 430–435, 2015.
- [27] K. Hellbach, A. Yaroshenko, K. Willer, T. Pritzke, A. Baumann, N. Hesse, S. Auweter, M. F. Reiser, O. Eickelberg, F. Pfeiffer, A. Hilgendorff, and F. G. Meinel, “Facilitated Diagnosis of Pneumothoraces in Newborn Mice Using X-ray Dark-Field Radiography,” *Investigative Radiology*, 2016.
- [28] A. Yaroshenko, T. Pritzke, M. Koschlig, N. Kamgari, K. Willer, L. B. Gromann, S. Auweter, K. Hellbach, M. Reiser, O. Eickelberg, F. Pfeiffer, and A. Hilgendorff, “Visualization of neonatal lung injury associated with mechanical ventilation using x-ray dark-field radiography,” *Scientific Reports*, vol. 6, no. 1, p. 24269, jul 2016.
- [29] K. Scherer, A. Yaroshenko, D. A. Bölükbas, L. B. Gromann, K. Hellbach, F. G. Meinel, M. Braunagel, J. von Berg, O. Eickelberg, M. F. Reiser, F. Pfeiffer, S. Meiners, and J. Herzen, “X-ray Dark-field Radiography - In-Vivo Diagnosis of Lung Cancer in Mice,” *Scientific Reports*, vol. 7, no. 1, p. 402, 2017.
- [30] WHO, “The top 10 causes of death,” <http://www.who.int/mediacentre/factsheets/fs310/en/>, 2014. [Online]. Available: <http://www.who.int/mediacentre/factsheets/fs310/en/>
- [31] E. P. Judge, J. M. L. Hughes, J. J. Egan, M. Maguire, E. L. Molloy, and S. O’Dea, “Anatomy and bronchoscopy of the porcine lung: A model for translational respiratory medicine,” *American Journal of Respiratory Cell and Molecular Biology*, vol. 51, no. 3, pp. 334–343, 2014.
- [32] M. Eckert, “Max von Laue and the discovery of X-ray diffraction in 1912,” *Annalen der Physik*, vol. 524, no. 5, pp. A83–A85, 2012.

- [33] D. Paganin, *Coherent X-Ray Optics*. Oxford University Press, jan 2006.
- [34] D. Attwood, *Soft X-rays and Extreme Ultraviolet Radiation: Principles and Applications*. Cambridge: Cambridge University Press, 1999.
- [35] J. Als-Nielsen and D. McMorrow, *Elements of Modern X-Ray Physics: Second Edition*, 2011.
- [36] P. Willmott, *An introduction to synchrotron radiation: Techniques and applications*, 2011.
- [37] C. T. Chantler, K. Olsen, R. A. Dragoset, J. Chang, A. R. Kishore, S. A. Kotochigova, and D. S. Zucker, “X-Ray Form Factor, Attenuation and Scattering Tables (version 2.1). [Online],” 2005. [Online]. Available: <http://physics.nist.gov/ffast>
- [38] A. Beer, “Bestimmung der Absorption des rothen Lichts in farbigen Flüssigkeiten.” *Annalen der Physik und Chemie*, vol. 86, no. 1, pp. 78–88, 1852.
- [39] J. W. Goodman, *Introduction to Fourier Optics*, 3rd ed. Stanford University, 2005.
- [40] W. H. F. Talbot, “Facts relating to optical science No. IV,” *Philos. Mag.*, vol. 9, pp. 401–407, 1836.
- [41] L. Rayleigh, “On copying diffraction-gratings, and on some phenomena connected therewith,” *Philosophical Magazine Series 5*, vol. 11, no. 67, pp. 196–205, 1881.
- [42] W. D. Montgomery, “Self-Imaging Objects of Infinite Aperture,” *Journal of the Optical Society of America*, 1967.
- [43] A. W. Lohmann and J. A. Thomas, “Making an array illuminator based on the Talbot effect,” *Appl. Opt.*, vol. 29, no. 29, pp. 4337–4340, 1990.
- [44] T. J. Suleski, “Generation of Lohmann images from binary-phase Talbot array illuminators,” *Appl. Opt.*, vol. 36, no. 20, pp. 4686–4691, 1997.
- [45] A. W. Lohmann, H. Knuppertz, and J. Jahns, “Fractional Montgomery effect: a self-imaging phenomenon,” *Journal of the Optical Society of America A*, 2005.

- [46] Z. Zhong, W. Thomlinson, D. Chapman, and D. Sayers, "Implementation of diffraction-enhanced imaging experiments: at the NSLS and APS," *Nuclear Instruments and Methods in Physics Research, Section A: Accelerators, Spectrometers, Detectors and Associated Equipment*, vol. 450, no. 2, pp. 556–567, 2000.
- [47] C. David, B. Nöhammer, H. H. Solak, and E. Ziegler, "Differential x-ray phase contrast imaging using a shearing interferometer," *Applied Physics Letters*, vol. 81, no. 17, pp. 3287–3289, 2002.
- [48] T. Weitkamp, A. Diaz, C. David, F. Pfeiffer, M. Stampanoni, P. Cloetens, and E. Ziegler, "X-ray phase imaging with a grating interferometer," *Opt. Express*, vol. 13, no. 16, pp. 6296–6304, 2005.
- [49] A. Olivo and R. Speller, "A coded-aperture technique allowing x-ray phase contrast imaging with conventional sources," *Applied Physics Letters*, vol. 91, no. 7, 2007.
- [50] Z. F. Huang, K. J. Kang, L. Zhang, Z. Q. Chen, F. Ding, Z. T. Wang, and Q. G. Fang, "Alternative method for differential phase-contrast imaging with weakly coherent hard x rays," *Physical Review A - Atomic, Molecular, and Optical Physics*, vol. 79, no. 1, pp. 1–6, 2009.
- [51] A. Olivo, L. Rigon, S. J. Vinnicombe, K. C. Cheung, M. Ibison, and R. D. Speller, "Phase contrast imaging of breast tumours with synchrotron radiation." *Applied radiation and isotopes : including data, instrumentation and methods for use in agriculture, industry and medicine*, vol. 67, no. 6, pp. 1033–41, jun 2009.
- [52] A. Olivo, S. Gkoumas, M. Endrizzi, C. K. Hagen, M. B. Szafraniec, P. C. Diemoz, P. R. T. Munro, K. Ignatyev, B. Johnson, J. a. Horrocks, S. J. Vinnicombe, J. L. Jones, and R. D. Speller, "Low-dose phase contrast mammography with conventional x-ray sources," *Medical Physics*, vol. 40, no. 9, p. 090701, 2013.
- [53] P. Modregger, T. P. Cremona, C. Benarafa, J. C. Schittny, A. Olivo, and M. Endrizzi, "Small angle x-ray scattering with edge-illumination," *Scientific Reports*, vol. 6, no. 1, p. 30940, nov 2016.
- [54] M. Endrizzi, A. Astolfo, F. A. Vittoria, T. P. Millard, and A. Olivo, "Asymmetric masks for laboratory-based X-ray phase-contrast imaging with edge illumination," *Scientific Reports*, vol. 6, p. 25466, 2016.

- [55] A. Astolfo, M. Endrizzi, F. A. Vittoria, P. C. Diemoz, B. Price, I. Haig, and A. Olivo, “Large field of view, fast and low dose multimodal phase-contrast imaging at high x-ray energy,” *Scientific Reports*, vol. 7, no. 1, p. 2187, 2017.
- [56] W. Yashiro, Y. Terui, K. Kawabata, and A. Momose, “On the origin of visibility contrast in x-ray Talbot interferometry,” *Optics Express*, vol. 18, no. 16, pp. 16 890–16 901, aug 2010.
- [57] S. K. Lynch, V. Pai, J. Auxier, A. F. Stein, E. E. Bennett, C. K. Kemble, X. Xiao, W.-K. Lee, N. Y. Morgan, H. Harold Wen, K. K. Camille, X. Xiao, W.-K. Lee, N. Y. Morgan, and H. H. Wen, “Interpretation of dark-field contrast and particle-size selectivity in grating interferometers,” *Applied Optics*, vol. 50, no. 22, pp. 4310–4319, 2011.
- [58] M. Strobl, “General solution for quantitative dark-field contrast imaging with grating interferometers.” *Scientific reports*, vol. 4, p. 7243, jan 2014.
- [59] A. Tapfer, “Small Animal X-ray Phase-Contrast Imaging,” PhD Thesis, TUM, 2013.
- [60] M. Chabior, “Contributions to the characterization of grating-based x-ray phase-contrast imaging,” PhD Thesis, TU Dresden, 2011.
- [61] C. Kottler, F. Pfeiffer, O. Bunk, C. Grünzweig, and C. David, “Grating interferometer based scanning setup for hard x-ray phase contrast imaging,” *Review of Scientific Instruments*, vol. 78, no. 4, 2007.
- [62] I. Amidror, *The Theory of the Moiré Phenomenon Volume II: Aperiodic Layers*, 2007, vol. I.
- [63] W. Yashiro, Y. Takeda, and A. Momose, “Efficiency of capturing a phase image using cone-beam x-ray Talbot interferometry.” *Journal of the Optical Society of America. A, Optics, image science, and vision*, vol. 25, no. 8, pp. 2025–2039, 2008.
- [64] T. Donath, M. Chabior, F. Pfeiffer, O. Bunk, E. Reznikova, J. Mohr, E. Hempel, S. Popescu, M. Hoheisel, M. Schuster, J. Baumann, and C. David, “Inverse geometry for grating-based x-ray phase-contrast imaging,” *Journal of Applied Physics*, vol. 106, no. 5, p. 054703, 2009.
- [65] F. Prade, A. Yaroshenko, J. Herzen, and F. Pfeiffer, “Short-range order in mesoscale systems probed by X-ray grating interferometry,” *EPL (Europhysics Letters)*, vol. 112, no. 6, p. 68002, 2015.

- [66] M. Bech, A. Tapfer, A. Velroyen, A. Yaroshenko, B. Pauwels, J. Hostens, P. Bruyndonckx, A. Sasov, and F. Pfeiffer, “In-vivo dark-field and phase-contrast x-ray imaging,” *Scientific Reports*, vol. 3, no. 1, p. 3209, 2013.
- [67] L. B. Gromann, K. Scherer, A. Yaroshenko, D. A. Bölükbas, K. Hellbach, F. G. Meinel, M. Braunagel, O. Eickelberg, M. F. Reiser, F. Pfeiffer, S. Meiners, and J. Herzen, “First experiences with in-vivo x-ray dark-field imaging of lung cancer in mice,” in *Progress in Biomedical Optics and Imaging - Proceedings of SPIE*, vol. 10132, 2017, p. 101325L.
- [68] L. B. Gromann, F. De Marco, K. Willer, P. B. Noël, K. Scherer, B. Renger, B. Gleich, K. Achterhold, A. A. Fingerle, D. Muenzel, S. Auweter, K. Hellbach, M. Reiser, A. Baehr, M. Dmochewicz, T. J. Schröter, F. J. Koch, P. Meyer, D. Kunka, J. Mohr, A. Yaroshenko, H.-I. Maack, T. Pralow, H. van der Heijden, R. Proksa, T. Koehler, N. Wieberneit, K. Rindt, E. J. Rummeny, F. Pfeiffer, and J. Herzen, “In-vivo X-ray Dark-Field Chest Radiography of a Pig,” *Scientific Reports*, vol. 7, no. 1, p. 4807, dec 2017.
- [69] R. Behling, *Modern diagnostic x-ray sources technology, manufacturing, reliability*. Boca Raton: CRC Press, 2015.
- [70] P. A. Tipler and G. Mosca, *Physik: für Wissenschaftler und Ingenieure*, 2007.
- [71] C. H. McCollough, S. Leng, L. Yu, and J. G. Fletcher, “Dual- and Multi-Energy CT: Principles, Technical Approaches, and Clinical Applications,” *Radiology*, vol. 276, no. 3, pp. 637–653, 2015.
- [72] R. L. Heath, *The Application of High-Resolution Solid State Detectors to X-Ray Spectrometry — A Review*. Boston, MA: Springer US, 1972, pp. 1–35.
- [73] IAEA, *Radiation Oncology Physics: A Handbook for Teachers and Students*, E. B. Podgorsak, Ed., Vienna, 2005.
- [74] Bundesrepublik Deutschland, “Verordnung über den Schutz vor Schäden durch Röntgenstrahlen (Röntgenverordnung - RöV),” 2010.
- [75] H. Smith, D. Beninson, H. Jammet, R. Clarke, A. Guskova, W. Jacobi, D. Li, J. Liniecki, and B. Meinhold, C, “ICRP publication 60,” *Annals of the ICRP*, vol. 21, no. 1-3, 1990.

- [76] ICRP, “ICRP 103: The 2007 Recommendations of the International Commission on Radiological Protection,” *Annals of the ICRP*, vol. 37, p. 330, 2007. [Online]. Available: <http://ani.sagepub.com/lookup/doi/10.1016/j.icrp.2007.10.001>
- [77] H. C. Munich, “Grundlagenkurs (Technik) nach Röntgenverordnung (Modul RM),” Tech. Rep., 2017.
- [78] RSNA, “Effective radiation dose in adults.” [Online]. Available: <https://www.radiologyinfo.org/en/info.cfm?pg=safety-xray>
- [79] P. Bartl, J. Durst, W. Haas, T. Michel, A. Ritter, T. Weber, and G. Anton, “Simulation of X-ray phase-contrast imaging using grating-interferometry,” in *IEEE Nuclear Science Symposium Conference Record*, 2009, pp. 3577–3580.
- [80] P. Bartl, F. Bayer, J. Durst, W. Haas, T. Michel, A. Ritter, T. Weber, and G. Anton, “Grating-based high energy X-ray interferometry with the Medipix-detector in simulation and measurement,” *Journal of Instrumentation*, vol. 5, no. 10, p. P10008, 2010.
- [81] A. D. Malecki, G. Potdevin, and F. Pfeiffer, “Quantitative wave-optical numerical analysis of the dark-field signal in grating-based X-ray interferometry,” *EPL (Europhysics Letters)*, vol. 99, no. 4, p. 48001, aug 2012.
- [82] S. Cipiccia, F. A. Vittoria, M. Weikum, A. Olivo, and D. A. Jaroszynski, “Inclusion of coherence in Monte Carlo models for simulation of x-ray phase contrast imaging,” *Optics Express*, vol. 22, no. 19, p. 23480, 2014.
- [83] J. Wolf, A. Malecki, J. Sperl, M. Chabior, M. Schüttler, D. Bequé, C. Cozzini, and F. Pfeiffer, “Fast one-dimensional wave-front propagation for x-ray differential phase-contrast imaging,” *Biomedical Optics Express*, vol. 5, no. 10, p. 3739, 2014.
- [84] A. Ritter, P. Bartl, F. Bayer, K. C. Gödel, W. Haas, T. Michel, G. Pelzer, J. Rieger, T. Weber, A. Zang, and G. Anton, “Simulation framework for coherent and incoherent X-ray imaging and its application in Talbot-Lau dark-field imaging,” *Optics Express*, vol. 22, no. 19, p. 23276, 2014.
- [85] Y. Sung, W. P. Segars, A. Pan, M. Ando, C. J. R. Sheppard, and R. Gupta, “Realistic wave-optics simulation of X-ray phase-contrast

- imaging at a human scale,” *Scientific Reports*, vol. 5, no. 1, p. 12011, 2015.
- [86] J. D. Schmidt, *Numerical Simulation of Optical Wave Propagation with Examples in MATLAB*, 2010. [Online]. Available: <http://ebooks.spiedigitallibrary.org/book.aspx?doi=10.1117/3.866274>
- [87] J. H. Siewerdsen, A. M. Waese, D. J. Moseley, S. Richard, and D. A. Jaffray, “Spektr: A computational tool for x-ray spectral analysis and imaging system optimization,” *Medical Physics*, vol. 31, no. 11, pp. 3057–3067, 2004.
- [88] J. M. Boone and J. A. Seibert, “An accurate method for computer-generating tungsten anode x-ray spectra from 30 to 140 kV,” *Medical Physics*, vol. 24, no. 11, pp. 1661–1670, 1997.
- [89] D. Sarrut, M. Bardiès, N. Bousson, N. Freud, S. Jan, J.-M. Létang, G. Loudos, L. Maigne, S. Marcatili, T. Mauxion, P. Papadimitroulas, Y. Perrot, U. Pietrzyk, C. Robert, D. R. Schaart, D. Visvikis, and I. Buvat, “A review of the use and potential of the GATE Monte Carlo simulation code for radiation therapy and dosimetry applications,” *Medical Physics*, vol. 41, no. 6, p. 064301, 2014.
- [90] S. Agostinelli, J. Allison, K. Amako, J. Apostolakis, H. Araujo, P. Arce, M. Asai, D. Axen, S. Banerjee, G. Barrand, F. Behner, L. Bellagamba, J. Boudreau, L. Broglia, A. Brunengo, H. Burkhardt, S. Chauvie, J. Chuma, R. Chytraccek, G. Cooperman, G. Cosmo, P. Degtyarenko, A. Dell’Acqua, G. Depaola, D. Dietrich, R. Enami, A. Feliciello, C. Ferguson, H. Fesefeldt, G. Folger, F. Foppiano, A. Forti, S. Garelli, S. Giani, R. Giannitrapani, D. Gibin, J. J. Gomez Cadenas, I. Gonzalez, G. Gracia Abril, G. Greeniaus, W. Greiner, V. Grichine, A. Grossheim, S. Guatelli, P. Gumplinger, R. Hamatsu, K. Hashimoto, H. Hasui, A. Heikkinen, A. Howard, V. Ivanchenko, A. Johnson, F. W. Jones, J. Kallenbach, N. Kanaya, M. Kawabata, Y. Kawabata, M. Kawaguti, S. Kelner, P. Kent, A. Kimura, T. Kodama, R. Kokoulin, M. Kossov, H. Kurashige, E. Lamanna, T. Lampen, V. Lara, V. Lefebure, F. Lei, M. Liendl, W. Lockman, F. Longo, S. Magni, M. Maire, E. Medernach, K. Minamimoto, P. Mora de Freitas, Y. Morita, K. Murakami, M. Nagamatu, R. Nartallo, P. Nieminen, T. Nishimura, K. Ohtsubo, M. Okamura, S. O’Neale, Y. Oohata, K. Paech, J. Perl, A. Pfeiffer, M. G. Pia, F. Ranjard, A. Rybin, S. Sadilov, E. di Salvo, G. Santin, T. Sasaki, N. Savvas, Y. Sawada, S. Scherer, S. Sei, V. Sirotenko,

- D. Smith, N. Starkov, H. Stoecker, J. Sulkimo, M. Takahata, S. Tanaka, E. Tcherniaev, E. Safai Tehrani, M. Tropeano, P. Truscott, H. Uno, L. Urban, P. Urban, M. Verderi, A. Walkden, W. Wander, H. Weber, J. P. Wellisch, T. Wenaus, D. C. Williams, D. Wright, T. Yamada, H. Yoshida, and D. Zschiesche, "GEANT4 - A simulation toolkit," *Nuclear Instruments and Methods in Physics Research, Section A: Accelerators, Spectrometers, Detectors and Associated Equipment*, vol. 506, no. 3, pp. 250–303, 2003.
- [91] M. Willner, M. Bech, J. Herzen, I. Zanette, D. Hahn, J. Kenntner, J. Mohr, A. Rack, T. Weitkamp, and F. Pfeiffer, "Quantitative X-ray phase-contrast computed tomography at 82 keV," *Optics Express*, vol. 21, no. 4, pp. 4155–4166, 2013.
- [92] A. Sarapata, M. Willner, M. Walter, T. Duttenhofer, K. Kaiser, P. Meyer, C. Braun, A. Fingerle, P. B. Noël, F. Pfeiffer, and J. Herzen, "Quantitative imaging using high-energy X-ray phase-contrast CT with a 70 kVp polychromatic X-ray spectrum." *Optics Express*, vol. 23, no. 1, pp. 523–535, 2015.
- [93] M. Ruiz-Yaniz, F. Koch, I. Zanette, A. Rack, P. Meyer, D. Kunka, A. Hipp, J. Mohr, and F. Pfeiffer, "X-ray grating interferometry at photon energies over 180 keV," *Applied Physics Letters*, vol. 106, no. 15, 2015.
- [94] A. Yaroshenko, "X-Ray Dark-Field Imaging For Diagnosis of Pulmonary Disorders," Dissertation, Technical University Munich, 2015.
- [95] T. Thuring and M. Stampanoni, "Performance and optimization of X-ray grating interferometry," *Phil. Trans. R. Soc. A*, vol. 372, no. January, pp. 20 130 027–20 130 027, 2014.
- [96] A. Yaroshenko, M. Bech, G. Potdevin, A. Malecki, T. Biernath, J. Wolf, A. Tapfer, M. Schüttler, J. Meiser, D. Kunka, M. Amberger, J. Mohr, and F. Pfeiffer, "Non-binary phase gratings for x-ray imaging with a compact Talbot interferometer." *Optics express*, vol. 22, no. 1, pp. 547–56, jan 2014.
- [97] L. B. Gromann, D. Bequé, K. Scherer, K. Willer, L. Birnbacher, M. Willner, J. Herzen, S. Grandl, K. Hellerhoff, J. I. Sperl, F. Pfeiffer, and C. Cozzini, "Low-dose, phase-contrast mammography with high signal-to-noise ratio," *Biomedical Optics Express*, vol. 7, no. 2, pp. 381–391, 2016.

- [98] K. Scherer, K. Willer, L. B. Gromann, L. Birnbacher, E. Braig, S. Grandl, A. Sztrkay-Gaul, J. Herzen, D. Mayr, K. Hellerhoff, and F. Pfeiffer, "Toward Clinically Compatible Phase-Contrast Mammography," *PLoS ONE*, vol. 10, no. 6, p. e0130776, 2015.
- [99] F. Horn, K. Gelse, S. Jabari, C. Hauke, S. Kaeppler, V. Ludwig, P. Meyer, T. Michel, J. Mohr, G. Pelzer, J. Rieger, C. Riess, M. Seifert, and G. Anton, "High-energy x-ray Talbot-Lau radiography of a human knee," *Physics in Medicine & Biology*, vol. 62, no. 16, pp. 6729–6745, aug 2017.
- [100] T. Koehler, H. Daerr, G. Martens, N. Kuhn, S. Löscher, U. van Stevendaal, and E. Roessl, "Slit-scanning differential x-ray phase-contrast mammography: Proof-of-concept experimental studies," *Medical Physics*, vol. 42, no. 4, pp. 1959–1965, 2015.
- [101] J. Meiser, M. Willner, T. J. Schröter, A. Hofmann, J. Rieger, F. J. Koch, L. J. B. Birnbacher, M. Schüttler, D. Kunka, P. Meyer, A. Faisal, M. Amberger, T. Duttchenhofer, T. Weber, A. Hipp, S. Ehn, M. Walter, J. Herzen, J. Schulz, F. Pfeiffer, and J. Mohr, "Increasing the field of view in grating based X-ray phase contrast imaging using stitched gratings," *Journal of X-Ray Science and Technology*, vol. 24, no. 3, pp. 379–388, jun 2016.
- [102] CSEM SA, "CSEM Scientific And Technical Report 2016," Tech. Rep., 2016. [Online]. Available: www.csem.ch
- [103] T. J. Schröter, F. J. Koch, D. Kunka, P. Meyer, S. Tietze, S. Engelhardt, M. Zuber, T. Baumbach, K. Willer, L. Birnbacher, F. Prade, F. Pfeiffer, K.-M. Reichert, A. Hofmann, and J. Mohr, "Large-area full field x-ray differential phase-contrast imaging using 2D tiled gratings," *Journal of Physics D: Applied Physics*, vol. 50, no. 22, p. 225401, 2017.
- [104] T. J. Schröter, F. J. Koch, P. Meyer, D. Kunka, J. Meiser, K. Willer, L. B. Gromann, F. De Marco, J. Herzen, P. Noel, A. Yaroshenko, A. Hofmann, F. Pfeiffer, and J. Mohr, "Large field-of-view tiled grating structures for X-ray phase-contrast imaging," *Review of Scientific Instruments*, vol. 88, no. 1, p. 15104, 2017.
- [105] D. Noda, M. Tanaka, K. Shimada, and T. Hattori, "Fabrication of Diffraction Grating with High Aspect Ratio Using X-ray Lithography Technique for X-ray Phase Imaging," *Japanese Journal of Applied Physics*, vol. 46, no. 2, pp. 849–851, 2007.

- [106] S. Bachche, M. Nonoguchi, K. Kato, M. Kageyama, T. Koike, M. Kuribayashi, and A. Momose, “Laboratory-based X-ray phase-imaging scanner using Talbot-Lau interferometer for non-destructive testing,” *Scientific Reports*, vol. 7, no. 1, p. 6711, 2017.
- [107] V. Revol, C. Kottler, R. Kaufmann, U. Straumann, and C. Urban, “Noise analysis of grating-based x-ray differential phase contrast imaging.” *The Review of scientific instruments*, vol. 81, no. 7, p. 73709, jul 2010.
- [108] M. Chabior, T. Donath, C. David, M. Schuster, C. Schroer, and F. Pfeiffer, “Signal-to-noise ratio in x ray dark-field imaging using a grating interferometer,” *Journal of Applied Physics*, vol. 110, no. 5, p. 053105, 2011.
- [109] R. H. Redus, J. A. Pantazis, T. J. Pantazis, A. C. Huber, and B. J. Cross, “Characterization of CdTe detectors for quantitative X-ray spectroscopy,” in *IEEE Transactions on Nuclear Science*, vol. 56, no. 4, 2009, pp. 2524–2532.
- [110] K. M. Martensen, *Radiographic Image Analysis - E-Book*, 3rd ed. Elsevier Health Sciences, 2013. [Online]. Available: <https://books.google.de/books?id=nVIPAQAAQBAJ>
- [111] H. G. Chotas, C. E. Floyd Jr., J. T. Dobbins 3rd, and C. E. Ravin, “Digital chest radiography with photostimulable storage phosphors: signal-to-noise ratio as a function of kilovoltage with matched exposure risk,” *Radiology*, 1993.
- [112] I. D. Honey, A. MacKenzie, and D. S. Evans, “Investigation of optimum energies for chest imaging using film-screen and computed radiography,” *British Journal of Radiology*, 2005.
- [113] M. Uffmann, U. Neitzel, M. Prokop, N. Kabalan, M. Weber, C. J. Herold, and C. Schaefer-Prokop, “Flat-panel-detector chest radiography: effect of tube voltage on image quality.” *Radiology*, 2005.
- [114] G. Ullman, M. Sandborg, D. R. Dance, R. A. Hunt, and G. A. Carlsson, “Towards optimization in digital chest radiography using Monte Carlo modelling,” *Physics in Medicine and Biology*, 2006.
- [115] S. Metz, P. Damoser, R. Hollweck, R. Roggel, C. Engelke, K. Woertler, B. Renger, E. J. Rummeny, and T. M. Link, “Chest Radiography with

- a Digital Flat-Panel Detector: Experimental Receiver Operating Characteristic Analysis,” *Radiology*, 2005.
- [116] ICRP, “Adult Reference Computational Phantoms ICRP,” *Annals of the ICRP*, 2009.
- [117] W. P. Segars, G. Sturgeon, S. Mendonca, J. Grimes, and B. M. W. Tsui, “4D XCAT phantom for multimodality imaging research,” *Medical Physics*, vol. 37, no. 9, p. 4902, 2010.
- [118] R. A. Brooks, “A quantitative theory of the Hounsfield unit and its application to dual energy scanning.” *Journal of computer assisted tomography*, vol. 1, no. 4, pp. 487–93, 1977.
- [119] D. Mentrup, U. Neitzel, S. Jockel, H.-I. Maack, and B. Menser, “Grid-like contrast enhancement for bedside chest radiographs acquired without anti-scatter grid,” Philips Healthcare, Tech. Rep., 2014. [Online]. Available: <http://incenter.medical.philips.com/doclib/enc/fetch/2000/4504/577242/577256/588723/588747/452299104241{ }SkyFlow{ }White{ }Paper{ }20140825.pdf>
- [120] D. Mentrup, S. Jockel, U. Neitzel, and B. Menser, “Grid-like contrast restoration for non-grid chest radiographs by software-based scatter correction,” in *European Congress of Radiology*, no. March, 2014, pp. 1–15.
- [121] D. Mentrup, S. Jockel, B. Menser, and U. Neitzel, “Iterative scatter correction for grid-less bedside chest radiography : Performance for a chest phantom CHEST RADIOGRAPHY : PERFORMANCE FOR A CHEST,” *Radiation protection dosimetry*, vol. 169, no. 1-4, pp. 308–312, 2016.
- [122] B. Renger, C. Brieskorn, V. Toth, D. Mentrup, S. Jockel, F. Lohöfer, M. Schwarz, E. J. Rummeny, and P. B. Noel, “EVALUATION OF DOSE REDUCTION POTENTIALS OF A NOVEL SCATTER CORRECTION SOFTWARE FOR BEDSIDE CHEST X-RAY IMAGING,” *Radiation Protection Dosimetry*, vol. 169, no. 1-4, pp. 60–67, 2016.
- [123] M. Chabior, T. Donath, C. David, O. Bunk, M. Schuster, C. Schroer, and F. Pfeiffer, “Beam hardening effects in grating-based x-ray phase-contrast imaging,” *Medical Physics*, vol. 38, no. 3, 2011.

- [124] W. Yashiro, P. Vagovic, and A. Momose, "Effect of beam hardening on a visibility-contrast image obtained by X-ray grating interferometry," *Opt. Express*, vol. 23, no. 18, pp. 23 462–23 471, sep 2015.
- [125] G. Pelzer, G. Anton, F. Horn, J. Rieger, A. Ritter, J. Wandner, T. Weber, and T. Michel, "A beam hardening and dispersion correction for x-ray dark-field radiography," *Medical Physics*, vol. 43, no. 6, pp. 2774–2779, jun 2016.
- [126] W. R. Brody, G. Butt, a. Hall, and a. Macovski, "A method for selective tissue and bone visualization using dual energy scanned projection radiography." *Medical physics*, vol. 8, no. 3, pp. 353–357, 1981.
- [127] R. E. Alvarez and A. Macovski, "Energy-selective reconstructions in X-ray computerised tomography," *Physics in Medicine and Biology*, vol. 21, no. 5, pp. 733–744, sep 1976.
- [128] L. A. Lehmann, "Generalized image combinations in dual KVP digital radiography," *Medical Physics*, vol. 8, no. 5, p. 659, sep 1981.
- [129] H. N. Cardinal, "An accurate method for direct dual-energy calibration and decomposition," *Medical Physics*, vol. 17, no. 3, pp. 327–341, 1990.
- [130] J. E. Kuhlman, J. Collins, G. N. Brooks, D. R. Yandow, and L. S. Broderick, "Dual-energy subtraction chest radiography: what to look for beyond calcified nodules," *Radiographics*, vol. 26, no. 1, pp. 79–92, 2006.
- [131] E. Roessl and R. Proksa, "K-edge imaging in x-ray computed tomography using multi-bin photon counting detectors." *Physics in medicine and biology*, vol. 52, no. 15, pp. 4679–4696, 2007.
- [132] J. von Berg, S. Young, H. Carolus, R. Wolz, A. Saalbach, A. Hidalgo, A. Giménez, and T. Franquet, "A novel bone suppression method that improves lung nodule detection," *International Journal of Computer Assisted Radiology and Surgery*, vol. 11, no. 4, pp. 641–655, 2016.
- [133] G. Drexler, L. Wiedenmann, and W. Panzer, *Die Bestimmung der Organdosen in der Röntgendiagnostik*. Hoffmann, 1993.
- [134] "Richtlinie für die technische Prüfung von Röntgeneinrichtungen und genehmigungsbedürftigen Störstrahlern," BMUB, Tech. Rep., 2009. [Online]. Available: http://www.bmub.bund.de/fileadmin/Daten{__}BMU/Download{__}PDF/Strahlenschutz/sv{__}richtlinie.pdf

- [135] O. Yadid-Pecht, “Geometrical modulation transfer function for different pixel active area shapes,” *Optical Engineering*, vol. 39, no. 4, p. 859, 2000.
- [136] G. D. Boreman and G. D. Boremann, *Modulation Transfer Function in Optical and Electro-Optical Systems*, 2001.
- [137] H. Einarsdóttir, A. Yaroshenko, A. Velroyen, M. Bech, K. Hellbach, S. Auweter, Ö. Yildirim, F. G. Meinel, O. Eickelberg, M. F. Reiser, R. Larsen, B. K. Ersbøll, and F. Pfeiffer, “Computer-aided diagnosis of pulmonary diseases using x-ray darkfield radiography,” *Physics in Medicine and Biology*, vol. 60, no. 24, p. 9253, 2015.
- [138] F. a. J. Mettler, W. Huda, T. T. Yoshizumi, and M. Mahesh, “Effective Doses in Radiology and Diagnostic Nuclear Medicine,” *Radiology*, vol. 248, no. 1, pp. 254–263, 2008.
- [139] German Commission on Radiological Protection, “Orientierungshilfe fuer radiologische und nuklearmedizinische Untersuchungen,” Strahlenschutzkommission (SSK) des Bundesministeriums fuer Umwelt, Naturschutz und Reaktorsicherheit, Berlin, Tech. Rep. 51, 2006. [Online]. Available: <http://www.ssk.de>
- [140] A. Yaroshenko, K. Hellbach, M. Bech, S. Grandl, M. F. Reiser, F. Pfeiffer, and F. G. Meinel, “Grating-based X-ray dark-field imaging: a new paradigm in radiography,” *Current Radiology Reports*, vol. 2, no. 7, p. 57, may 2014.
- [141] BKA, “Rauschgiftkriminalität Bundeslagebericht 2015,” Bundeskriminalamt, Tech. Rep., 2015. [Online]. Available: <https://www.bka.de/SharedDocs/Downloads/DE/Publikationen/JahresberichteUndLagebilder/Rauschgiftkriminalitaet/2015RauschgiftBundeslagebildZ.html?nn=27972>
- [142] I. Evrard, S. Legleye, and A. Cadet-Taïrou, “Composition, purity and perceived quality of street cocaine in France,” *International Journal of Drug Policy*, vol. 21, no. 5, pp. 399–406, sep 2010.
- [143] N. P. Bernardo, M. E. P. B. Siqueira, M. J. N. de Paiva, and P. P. Maia, “Caffeine and other adulterants in seizures of street cocaine in Brazil,” *International Journal of Drug Policy*, vol. 14, no. 4, pp. 331–334, mar 2017.

- [144] W. Haas, M. Polyanskaya, F. Bayer, K. Gödel, H. Hofmann, J. Rieger, A. Ritter, T. Weber, L. Wucherer, J. Durst, T. Michel, G. Anton, and J. Hornegger, “Image fusion in x-ray differential phase-contrast imaging,” in *Proc. SPIE 8314, Medical Imaging: Image Processing*, vol. 8314, 2012, pp. 83 143U–83 143U–6.
- [145] E. Roessl, T. Koehler, U. van Stevendaal, G. Martens, N. Hauser, Z. Wang, and M. Stampanoni, “Image fusion algorithm for differential phase contrast imaging,” in *Proc. SPIE 8313, Medical Imaging: Physics of Medical Imaging*, vol. 8313, 2012, pp. 831 354–831 356.
- [146] Z. Wang, C. a. Clavijo, E. Roessl, U. V. Stevendaal, T. Koehler, N. Hauser, and M. Stampanoni, “Image fusion scheme for differential phase contrast mammography,” *Journal of Instrumentation*, vol. 8, no. 07, pp. C07 011–C07 011, jul 2013.
- [147] E. Coello, J. I. Sperl, D. Bequé, T. Benz, K. Scherer, J. Herzen, A. Sztrókay-Gaul, K. Hellerhoff, F. Pfeiffer, C. Cozzini, and S. Grandl, “Fourier domain image fusion for differential X-ray phase-contrast breast imaging,” *European Journal of Radiology*, vol. 89, pp. 27–32.
- [148] E. A. Miller, T. A. White, B. S. McDonald, and A. Seifert, “Phase Contrast X-Ray Imaging Signatures for Security Applications,” *IEEE Transactions on Nuclear Science*, vol. 60, no. 1, pp. 416–422, 2013.
- [149] F. Schaff, A. Malecki, G. Potdevin, E. Eggl, P. B. Noël, T. Baum, E. G. Garcia, J. S. Bauer, and F. Pfeiffer, “Correlation of X-Ray Vector Radiography to Bone Micro-Architecture,” *Scientific Reports*, vol. 4, no. 05, pp. 1528–1533, jan 2014.
- [150] E. Eggl, A. Malecki, F. Schaff, G. Potdevin, P. B. Noël, J. S. Bauer, O. Gordijenko, E. Grande García, R. Burgkart, E. J. Rummeny, T. Baum, and F. Pfeiffer, “Prediction of Vertebral Failure Load by Using X-Ray Vector Radiographic Imaging,” *Radiology*, vol. 275, no. 2, pp. 553–561, 2015.
- [151] J. Rieger, P. Meyer, G. Pelzer, T. Weber, T. Michel, J. Mohr, and G. Anton, “Designing the phase grating for Talbot- Lau phase-contrast imaging systems : a simulation and experiment study,” *Optics Express*, vol. 24, no. 12, pp. 13 357–13 365, 2016.

Acknowledgements

I would like to thank...

... my academic supervisor Prof. Dr. Franz Pfeiffer for giving me the possibility to work on this great project in such an inspiring environment. Thank you for your guidance, mentoring and sharing your knowledge with me. With your chair, you created something unique and I am really glad that I could be part of it for the last three/four years.

... Konstantin Willer and Fabio De Marco for their companionship during the whole project. Without you, nothing would have worked out that well and fast. The days (and nights) together with you in the lab and office were a real pleasure for me.

... Dr. Julia Herzen and Dr. Peter Noel for their organization and guidance of the constantly growing DAX project, their mentoring, proof-reading and valuable feedback for my work.

... Dr. Thomas Köhler for his mentoring during the last years and his constant encouragement to document all intermediate results; this made writing the final thesis much easier in the end.

... the other people from Philips, especially Dr. Andre Yaroshenko, Ingo Maack and Thomas Pralow for your constant input during our regular telcos and physical meetings. I appreciated it a lot. But also the rest of the Philips people for their enormous support either on providing excellent hardware, software or great ideas. Here I want to thank especially Hendrik van der Heijden, Karsten Rind, Nataly Wieberneit and Roland Proksa.

... Dr. Katharina Hellbach, Dr. Sigrid Auweter, Dr. Andrea Baehr and Michaela Dmochewitz for your support with the in-vivo imaging. It was quite a new experience for me and without you, this would not have been possible.

... Dr. Klaus Achterhold and Dr. Bernhard Gleich for your continuous help with all kind of regulatory, electronic and radiation safety issues and especially Klaus for his role as my official mentor. I learned a lot from you.

... Dr. Tobias Schröter, Dr. Frieder Koch, Dr. Pascal Meyer, Dr. Danays Kunka, Prof. Dr. Juergen Mohr and Dr. Joachim Schultz together with his company microworks for providing the excellent X-ray gratings. Without these, there were no XDF images at all. You did a great job there. But I

will also always remember the nice off-work events we had together either in Munich, Karlsruhe, Garmisch or Zurich.

... all the clinical doctors from both University Hospitals in Munich (Rechts der Isar & Großhadern), especially Dr. Katharina Hellbach, Dr. Alexander Fingerle, Dr. Daniela Münzel and Prof. Dr. Ernst Rummeny for their professional evaluation of the acquired images and your great scientific ideas. You improved the outcome of this thesis quite a lot.

... Bernhard Renger from the Klinikum rechts der Isar for sharing his knowledge about dose calculations and his help with the actual measurements.

... Dr. Dieter Renker, for his help on the development on all kind of handmade X-ray detectors and sensors. I really enjoyed the work with you and I hope I will keep up such a passion for physics like you do. Additionally, I am really thankful for your hospitality during the cooking sessions at your home or at our meetings in the beer-garden.

... all the people from the E17 chair. I enjoyed your company and friendship very much, both at work and during free time. I learned a lot from you and I really appreciated the countless scientific discussions with you. But I will also always remember the great trip to Florida with you, the numerous parties and events we had together: the singstar evenings in Sudelfeld, the legendary residence “Bei Gabi” in Garmisch and the nice evenings at Dieters place. It has been some great years together with you! A special thanks goes to all the people from the chair, who enabled smooth working of all the others with their passion like Nelly de Leiris and the IT-guys. Furthermore I would like to thank the other member of the growing *Dax Crew* Wolfgang Noichl, Jana Andrejewski, Manuela Frank, Alexander and Nico Gustschin, Kai Scherer, Eva Braig, Manuel Viermetz and Maximilian von Teuffenbach.

... my family for your continuous support over the last 28 years and especially Daniela for always being at my side.

... and all the other people who helped me finishing this work.

Thank you all!

